

University of Warwick institutional repository: <http://go.warwick.ac.uk/wrap>

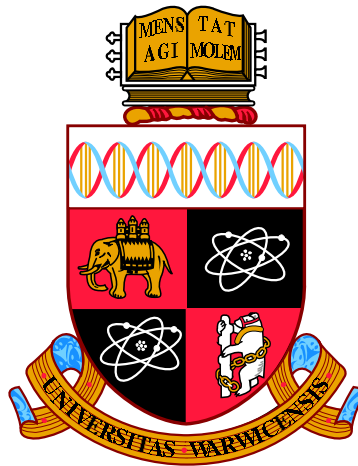
A Thesis Submitted for the Degree of PhD at the University of Warwick

<http://go.warwick.ac.uk/wrap/57512>

This thesis is made available online and is protected by original copyright.

Please scroll down to view the document itself.

Please refer to the repository record for this item for information to help you to cite it. Our policy information is available from the repository home page.



Phonons in Disordered Harmonic Lattices

by

Sebastian Pinski

Thesis

Submitted to the University of Warwick

for the degree of

Doctor of Philosophy

Physics Department

May 2013

THE UNIVERSITY OF
WARWICK

Contents

Acronyms	iv
List of Tables	vi
List of Figures	vii
Acknowledgments	xii
Declarations	xiii
Abstract	xiv
Chapter 1 Introduction	1
Chapter 2 Theory	4
2.1 Heat Transport and the Effects of Disorder	4
2.2 Anderson Localisation	6
2.2.1 Theoretical Background of Anderson Localisation	6
2.2.2 Universality Classes, Renormalisation Group Theory and Scal- ing Theory	8
2.2.3 Experimental Observations	10
2.3 Crystal Dynamics and the Canonical Equation	11
Chapter 3 Numerical Diagonalisation	14
3.1 Dense Matrix Diagonalisation	14
3.2 Sparse Matrix Diagonalisation	15
3.2.1 Sparse Matrix Structure	16
3.2.2 Power Method and Krylov Subspace	17
3.2.3 Shift and Invert Methods	18
3.2.4 Linear System of Equations	18

3.2.5	Code Packages	19
Chapter 4	One Dimensional Systems	20
4.1	Lattice Dynamics	20
4.1.1	Participation Ratios and Vibrational Density of States	21
4.2	Binary Disorder	22
4.3	Fibonacci Series	24
4.4	Uniform Disorder	26
Chapter 5	Three Dimensional Normal Modes and Vibrational Den-	
	sity of States	34
5.1	Scalar Model of Lattice Dynamics	34
5.1.1	Maximum and Minimum Frequencies	36
5.2	Normal Modes	37
5.3	Numerical Vibrational Density of States	40
5.4	The Coherent Potential Approximation	41
5.4.1	Mass Disorder	41
5.4.2	Spring Constant Disorder	46
5.5	The Boson Peak	48
Chapter 6	Three Dimensional Localisation-Delocalisation Transition	55
6.1	Electronic Anderson Phase Boundary Conversion	55
6.2	Transfer Matrix Method	61
6.2.1	Numerical Method	61
6.3	Localisation Lengths	63
6.3.1	Finite Size Scaling	66
6.3.2	Critical Parameters	75
6.4	Phase Diagrams	78
6.4.1	Truncated Spring Distribution Phase Diagram	82
Chapter 7	Three Dimensional Vibrational Eigenstate Statistics	85
7.1	Random Matrix Theory	85
7.1.1	The Porter-Thomas Distribution	86
7.1.2	Maximally Localised Distribution	87
7.1.3	Deviations and the Boson Peak	90
Chapter 8	Three Dimensional Participation Ratios and Multifractal	
	Analysis	93
8.1	Participation Ratios	93

8.1.1	Typical Participation Ratio Data	95
8.1.2	Average Participation Ratio for Constant System Size	96
8.1.3	Localisation-Delocalisation Transition from Participation Ratios	96
8.2	Multifractal Analysis	99
8.2.1	Fractal Structures and Dimensions	99
8.2.2	Mass Exponents and Generalised Dimensions	102
8.2.3	The Singularity Spectrum	103
8.2.4	Numerical Implementation	107
Chapter 9 Conclusions		118
Appendices		119
A	Tables of Critical Parameters	120
B	Weighted Averaging	120

Acronyms

1D one-dimension. vi, 3, 8, 9, 11, 20, 22, 26, 27, 30–32, 34, 61, 64, 76, 81, 107, 118

2D two-dimensions. 8, 9, 81, 107

3D three-dimensions. vi, 3, 9, 11, 16, 20, 30, 31, 34, 35, 37, 46, 55, 106, 118

AM Anderson model. 7, 55–57, 78, 87, 106, 107, 117, 119

BP ‘boson-peak’. vii, 3, 48–51, 53, 54, 80, 85–87, 90–92, 96, 97, 119

CPA coherent potential approximation. 34, 41–43, 45–48, 50, 52, 80, 119

DOS density of states. vi, 7, 8, 14, 31, 33, 43–48, 58, 99, 106, 119

FSS finite size scaling. vi, 58, 64, 68, 70, 71, 74–79, 109, 120–124

gIPR generalised inverse participation ratio. vi, 93, 99, 102, 104, 107

GOE Gaussian orthogonal ensemble. 50, 85, 86, 88, 89, 92, 119

IPR inverse participation ratio. 102

LDT localisation-delocalisation transition. vi, 3, 8, 11, 33, 41, 48, 51, 55, 56, 58–60, 66, 72, 78, 79, 84–87, 93, 94, 96, 99, 102, 105, 106, 109, 116–119

MFA multi-fractal analysis. 93, 99, 117, 119

MIT metal-insulator transition. 8–10, 80, 102, 112, 116, 119

NL σ M non-linear sigma model. 8, 106

PDF probability density function. 104, 105

PR participation ratio. 14, 21–29, 78, 93–99

PTD Porter-Thomas distribution. vii, 85–90, 92, 96

RMT random matrix theory. 85, 86

TMM transfer-matrix method. vi, 27, 30, 32, 58, 61, 66, 67, 78, 81, 82, 96, 99, 119

VDOS vibrational density of states. 21–25, 27–29, 33, 34, 40–43, 45, 47–50, 52, 58, 79, 81, 116, 117, 119

List of Tables

6.1	For orders of expansion $n_{r_0}, n_{r_1}, n_i, m_r$ and m_i from finite size scaling, critical parameters ω_c or ω_c^2 and ν , with the minimised χ^2 value, the degrees of freedom μ and the resulting goodness-of-fit parameter Γ_q for pure mass and pure spring constant disorders.	78
A.1	Critical parameters for lowest stable fits and higher order stability testing fits, from finite size scaling (in the ω^2 domain) of reduced localisation lengths of mass disordered crystals with disorder distribution widths $\Delta m = 1, 2, 4$ and 9	121
A.2	Critical parameters for lowest stable fits and higher order stability testing fits, from finite size scaling (in the ω domain) of reduced localisation lengths of mass disordered crystals with disorder distribution widths $\Delta m = 1, 2, 4$ and 9	122
A.3	Critical parameters for lowest stable fits and higher order stability testing fits, from finite size scaling (in the ω^2 domain) of reduced localisation lengths of spring constant disordered crystals with disorder distribution widths $\Delta k = 1, 7$ and 10	123
A.4	Critical parameters for lowest stable fits and higher order stability testing fits, from finite size scaling (in the ω domain) of reduced localisation lengths of spring constant disordered crystals with disorder distribution widths $\Delta k = 1, 7$ and 10	124

List of Figures

1.1	Image of a partially fried egg placed on an iPad to satirise the iPad heat controversy.	2
2.1	Thermal conductivity of Germanium as a function of percentage random substitution of Silicon.	5
2.2	Schematic electronic density of states and phase diagram as functions of potential disorder.	7
2.3	Schematic example showing the behaviour of scaling function β for dimensions $d = 1, 2$ and 3	9
3.1	Diagram illustrating the difference in sparsity of dynamical matrices for a periodic three-dimensional cubic systems of width $L = 5$ and 15	16
4.1	Participation ratios and vibrational density of states for a one-dimensional binary disordered chain of length $L = 1000$	23
4.2	Vibrational density of states, participation ratios, effective dispersion and normal modes of one-dimensional Fibonacci chains of length $L = 1000$ and Fibonacci numbers F_n of $n = 8-12$	25
4.3	Vibrational density of states, participation ratios and effective dispersion for one-dimensional chain of length $L = 1000$ with box distributed mass disorder	28
4.4	Vibrational density of states, participation ratios and effective dispersion for one-dimensional chain of length $L = 1000$ with box distributed spring constant disorder	29
4.5	Localisation lengths of a one-dimensional chain with box distributed mass disorder plotted as functions of frequency and disorder	30
4.6	Localisation lengths of a one-dimensional chain with box distributed spring constant disorder plotted as functions of frequency and disorder	31

4.7	Localisation lengths as a function of frequency for phonons in a one dimensional chain for a range of uniform box distributed pure mass and pure spring constant disorders	32
5.1	Diagram to demonstrate physical interpretation of three-dimensional periodic boundary conditions	37
5.2	Examples of normal modes in a three-dimensional box of size $L^3 = 70^3$ with mass disorder for possible extended, critical and localised states	38
5.3	Examples of normal modes in a three-dimensional box of size $L^3 = 70^3$ with spring constant disorder for possible extended, critical and localised states	39
5.4	Vibrational density of states obtained from numerical diagonalisation and coherent potential approximation studies for both mass and spring constant disorders	42
5.5	Reduced vibrational density of states as a function of frequency for both pure mass and spring constant box distributed disorders	49
5.6	Boson peak trajectories obtained from (both numerical diagonalisation and coherent potential approximation) reduced vibrational density of states	52
5.7	Vibrational eigenstates for positions around the mass disordered boson peak trajectory for system size $L^3 = 70^3$	53
5.8	Vibrational eigenstates for positions around the spring constant disordered boson peak trajectory for system size $L^3 = 70^3$	54
6.1	Examples of previously published electronic phase diagrams for box distributed potential disorders	58
6.2	Phase diagram conversion schematic from potential disordered electronic phase diagram to mass disordered phonon phase diagram	59
6.3	Reduced localisation lengths (as a function of squared frequency) and finite size scaling functions/correlation lengths with varying quasi-one-dimensional system sizes for box distributed mass disorder widths $\Delta m = 1, 4$ and 9	64
6.4	Reduced localisation lengths (as a function of squared frequency) and finite size scaling functions/correlation lengths with varying quasi-one-dimensional system sizes for box distributed spring constant disorder widths $\Delta k = 1, 7$ and 10	65

6.5	Reduced localisation lengths with analogous re-entrant behaviour in the negative squared frequency domain for box distributed mass disorder width $\Delta m = 9$	67
6.6	Distributions of critical parameters from Monte Carlo error analysis to obtain accurate unsymmetric error bars for critical parameters of the localisation-delocalisation transition for box distributed mass disorder width $\Delta m = 1.2$	72
6.7	Distributions of critical parameters from Monte Carlo error analysis to obtain accurate unsymmetric error bars for critical parameter of localisation-delocalisation transition for box distributed spring constant disorder width $\Delta k = 1$	73
6.8	Comparison of scaling for both frequency and squared frequency dependant variables with synthetic reduced localisation lengths	74
6.9	Reduced localisation lengths (as a function of frequency) and finite size scaling functions/correlation lengths with varying quasi-one-dimensional system sizes for box distributed mass disorder widths $\Delta k = 1, 4$ and 9	76
6.10	Reduced localisation lengths (as a function of frequency) and finite size scaling functions/correlation lengths with varying quasi-one-dimensional system sizes for box distributed spring constant disorder widths $\Delta k = 1, 7$ and 10	77
6.11	All twelve critical exponents from both frequency and squared frequency localisation-delocalisation transitions plotted with estimated errors and the overall weighted average	79
6.12	Phase diagram of localisation-delocalisation transitions for phonons with applied box distributed mass disorder	80
6.13	Phase diagram of localisation-delocalisation transitions for phonons with applied box distributed spring constant disorder	81
6.14	Electronic hopping disorder phase diagram for comparison to spring constant disorder phase diagram	82
6.15	Phase diagram of localisation-delocalisation transitions for phonons with applied box distributed spring constant disorder truncated so that all spring constants $ k > 10^{-4}$	83
7.1	Histograms of eigenvector displacements and difference with respect to the Porter-Thomas distribution for a range of frequencies in a three-dimensional system with the inclusion of uniform box distributed mass disorder of width $\Delta m = 1$	88

7.2	Histograms of eigenvector displacements and difference with respect to the Porter-Thomas distribution for a range of frequencies in a three-dimensional system with the inclusion of uniform box distributed spring constant disorder of width $\Delta k = 1$	89
7.3	Minima of deviations from Porter-Thomas distribution as a function of frequency for multiple disorders of both mass and spring constant type	91
8.1	Scatter plot of participation ratio versus squared frequency for all normal modes of 50 disorder realisations of mass and spring constant disorders $\Delta m = 1.5$ and $\Delta k = 1$ in a three-dimensional system of size $L^3 = 15^3$	95
8.2	Participation ratios averaged over 50 realisations of box distributed mass or spring constant disorder as a function of squared frequency for system size $L^3 = 15^3$	97
8.3	Running average over 100 frequency values on roughly 170,000 participation ratios per system size $L^3 = 5^3, 10^3$ and 15^3 in search of a localisation-delocalisation transition for mass and spring constant disorders $\Delta m = 1.5$ and $\Delta k = 1$	98
8.4	Romanesco broccoli is a natural self-affine structure whose cross-section resembles the Koch curve, a fractal with fractal dimension $D_f = 1.2619$	100
8.5	Schematic example of construction of the Mandelbrot-Given fractal .	101
8.6	Schematic example of the multifractal singularity spectrum with known features labelled appropriately	104
8.7	Example normal modes at criticality for mass disorder $\Delta m = 1.2$ in a three-dimensional cubic system of size $L^3 = 90^3$ and spring constant disorder of $\Delta k = 10$ in a system of size $L^3 = 100^3$	110
8.8	Example linear fits to obtain mass exponents $\tau_{\text{ens}}(q)$ and α_q for integer q values for mass disorder $\Delta m = 1.2$	111
8.9	Example linear fits to obtain f_q for $\Delta m = 1.2$ to construct the singularity spectrum	112
8.10	Numerical singularity spectrum $f(\alpha)$ for mass disorder $\Delta m = 1.2$. .	113
8.11	Numerical singularity spectrum $f(\alpha)$ for spring constant disorder $\Delta k = 1$	114
8.12	Numerical singularity spectrum $f(\alpha)$ for spring constant disorder $\Delta k = 10$	115

8.13 Numerical singularity spectrum $f(\alpha)$ for mass disorder $\Delta m = 1.2$
and spring constant disorder $\Delta k = 10$ in comparison with a high
precision electronic singularity spectrum obtained numerically at the
metal-insulator transition 116

Acknowledgments

First and foremost I dedicate this thesis to my life partner - Jenny Gordon. Without her continuing support I would never have gotten to this stage; not only in my research career, but life in general. I've been blessed by her presence ever since we met and hope that she can keep being my guiding light for however long I shall live.

I am forever indebted to my supervisor, Prof. Rudolf A. Römer for accepting me for a research degree, and thank him not only for his invaluable input to my work but also for the friendly and creative atmosphere he has developed within our modestly sized research group. I also thank Dr. Alberto Rodriguez-Gonzales for being a close friend during my first years at Warwick University, and an ocean of knowledge that I tapped into so often. I could not have done this without you both.

Other notable mentions go to other Disordered Quantum Systems group members throughout the years, in no particular order: Dr. Andrea Fischer, Dr. Louella Vasquez, Dr. Emilio Jimenez, Jack Heal, Andrew Goldsborough, Clara González-Santander, Carlos Paez and numerous other visitors. I thank you all for being like family to me.

I extend my gratitude to the Physics Department at the University of Warwick and the EPSRC for funding and providing me with some fantastic opportunities to present this work at numerous international conferences and warmly acknowledge the additional funds granted to me by the IOP (C R Barber Trust and the Research Student Conference Fund) and the University of Warwick American Study and Student Exchange Committee (ASSEC) used to pay for my travel.

Declarations

I hereby declare that this thesis entitled “Phonons in Disordered Harmonic Lattices” is an original work and has not been submitted for a degree, diploma or other qualification at any other University or degree granting institution. Chapters 1 to 3 provide information gathered from literature as referenced in the text, whereas chapters 4 to 8 are based on the following publications:

- “Study of the localization-delocalization transition for phonons via transfer matrix method techniques”, S. Pinski and R. A. Roemer, J. Phys. Conf. Ser. **286**, 012025 (2011);
- “Anderson universality in a model of disordered phonons”, S. Pinski, W. Schirmacher and R. A. Roemer, Europhys. Lett. **97**, 16007 (2012);
- “Localization-delocalization transition for disordered cubic harmonic lattices”, S. Pinski, W. Schirmacher, T. E. Whall, and R. A. Roemer, J. Phys.: Condens. Matter. **24**, 405401 (2012);
- “Universal multifractal behaviour for phonons and electrons at the Anderson transition”, S. Pinski, A. Rodriguez, W. Schirmacher, and R. A. Roemer, AIP Conf. Proc. **1506**, 62 (2012).

The above mentioned papers are the result of joint work with the indicated authors.

Abstract

This work explores the nature of the normal modes of vibration for harmonic lattices with the inclusion of disorder in one-dimension (1D) and three-dimensions (3D). The model systems can be visualised as a ‘ball’ and ‘spring’ model in simple cubic configuration, and the disorder is applied to the magnitudes of the masses, or the force constants of the interatomic ‘springs’ in the system.

With the analogous nature between the electronic tight binding Hamiltonian for potential disordered electronic systems and the isotropic Born model for phonons in mass disordered lattices we analyse in detail a transformation between the normal modes of vibration throughout a mass disordered harmonic lattice and the electron wave function of the tight-binding Hamiltonian. The transformation is applied to density of states (DOS) calculations and is also particularly useful for determining the phase diagrams for the phonon localisation-delocalisation transition (LDT). The LDT phase boundary for the spring constant disordered system is obtained with good resolution and the mass disordered phase boundary is verified with high precision transfer-matrix method (TMM) results. High accuracy critical parameters are obtained for three transitions for each type of disorder by finite size scaling (FSS), and consequently the critical exponent that characterises the transition is found as $\nu = 1.550^{+0.020}_{-0.017}$ which indicates that the transition is of the same orthogonal universality class as the electronic Anderson transition.

With multifractal analysis of the generalised inverse participation ratio (gIPR) for the critical transition frequency states at spring constant disorder width $\Delta k = 10$ and mass disorder width $\Delta m = 1.2$ we confirm that the singularity spectrum is the same within error as the electronic singularity spectrum at criticality and can be

considered to be universal.

We further investigate the nature of the modes throughout the spectrum of the disordered systems with vibrational eigenstate statistics. We find deviations of the vibrational displacement fluctuations away from the Porter-Thomas distribution (PTD) and show that the deviations are within the vicinity of the so called ‘boson-peak’ (BP) indicating the possible significance of the BP.

Chapter 1

Introduction

The miniaturisation of electronic devices has almost become a necessity in recent years. Manufacturers are not only expected to increase the specifications of their products, but also decrease the form factor with every iteration of the device. The challenges involved in the field of microelectronics are unprecedented and complications arise at every step of the development process. One of the more demanding aspects of this field is thermal management [1]. With reducing form factors, there is little space available for bulky fans and heat sinks, prompting the development of new and innovative materials to convert and channel heat away from core components. Sometimes this undertaking will go awry with a massive media backlash. After the release of the ‘new iPad’ on 16th March 2012, the Apple product was criticised in a consumer report for the ability to achieve a 47°C operating temperature¹ initiating a series of satirical images posted by technology bloggers, the most notable being a photograph of an egg supposedly frying on an iPad in Fig. 1.1. In most cases the newly developed materials are integrated within the electronic circuits and acquire more than just the role of thermal management. Most notable are thermoelectric materials [2] that can generate power from a temperature differential. The recent resurgence in this field has led to developments in both theory and advanced fabrication in an attempt to increase the thermoelectric figure of merit [3], the measure governs the efficiency of power conversion. It is defined as

$$ZT = \frac{\sigma S^2 T}{\kappa_e + \kappa_{ph}}, \quad (1.1)$$

where S is the Seebeck coefficient, T is the temperature, σ is the electrical conductivity, κ_e and κ_{ph} are the thermal conductivities due to electrons and phonons,

¹<http://news.consumerreports.org/electronics/2012/03/our-test-finds-new-ipad-hits-116-degrees-while-running-games.html>



Figure 1.1: Image of a partially fried egg placed on an iPad by famous technology blogger Robert Scoble who was satirising the iPad heat controversy via his Instagram account (http://statigr.am/p/151628232280579401_70).

respectively. Most methods proposed to improve the figure of merit ZT attempt to limit the phonon propagation whilst not significantly deteriorating the electronic transport in the system [4].

Currently two different research approaches are taken when producing thermoelectric materials [5]. The first approach is to develop new generations of bulk materials that contain heavy-ion species with large vibrational amplitudes that provide phonon scattering centres [6, 7]. The other is based on reducing the dimensionality of the system whilst including either nanoscale constituents to confine the phonons [8] or internal interfaces arranged such that the thermal conductivity is reduced more than electrical conductivity [9, 10]. The manufacturing techniques have advanced in recent years, yielding the ability to produce these material, but the theoretical understanding of phonon transport must now go beyond the macroscopic level. We are now entering a regime where the phonons interacting with nano-engineered structures needs to be understood at a microscopic level in order to progress in the field.

Comparatively less attention has been given to thermal transport, than to electrical conductivity research. Since the discovery of electricity, research has pushed the extremes of electrical conductivity which now spans over twenty or-

ders of magnitude. Thermal conductivity in solids at room temperature spans only four [2], yet the history of thermal transport goes back to primitive humankind, far beyond that of electrical conductivity. In this thesis I investigate the effect of disorder on vibrational modes in solids to increase understanding of the underlying heat transport processes for a large range of frequencies. In Chap. 4, 1D systems are studied and in Chaps. 5-8 3D systems are studied where features such as the BP and the LDT are the main areas of interest.

Chapter 2

Theory

2.1 Heat Transport and the Effects of Disorder

Phonons are quantised travelling elastic waves associated with the displacement of ions from their equilibrium lattice positions. Acoustic phonons are the predominant carriers of heat in any temperature regime (for electrical insulators) due to their large group velocity compared to that of optical phonons [11]. With lowering the lattice temperature of the sample, the wavelength (and mean free path) of a phonon increases but reaches a maximum limiting value of $2L$ (L being the length of the sample), as this is the lowest possible normal mode of the system.

Perfect crystalline lattices would exhibit the lowest possible mode of the system and in effect be a perfect thermal conductor of phonons. In nature impurities within the medium such as grain boundaries, impurity atoms, structural defects, vacancies and dislocations (anything that changes the bond stiffness/strength of adjacent lattice sites) cause the phonon thermal conductivity κ_{ph} to reduce. This is good evidence that impurities have the largest effect on κ_{ph} at low temperatures [11].

The first theoretical studies on a single ‘light’ impurity within a linear lattice were performed by Lifshitz et al. [12]. They found a high frequency mode that corresponded to the single light impurity moving back and fourth erratically within a cage of heavy particles, a localised phonon.

The thermal conductivity of a bulk crystalline solid according to Debye is expressed as [13, 14]

$$\kappa_{\text{ph}}(T) = \frac{k_B}{2\pi^2\nu} \left(\frac{k_B T}{\hbar} \right)^3 \int_0^{\theta_D/T} \tau(x, T) \frac{x^4 e^x}{(e^x - 1)^2} dx, \quad (2.1)$$

where k_B is the Boltzmann constant, \hbar is Planck’s constant ($/2\pi$), ν is the speed

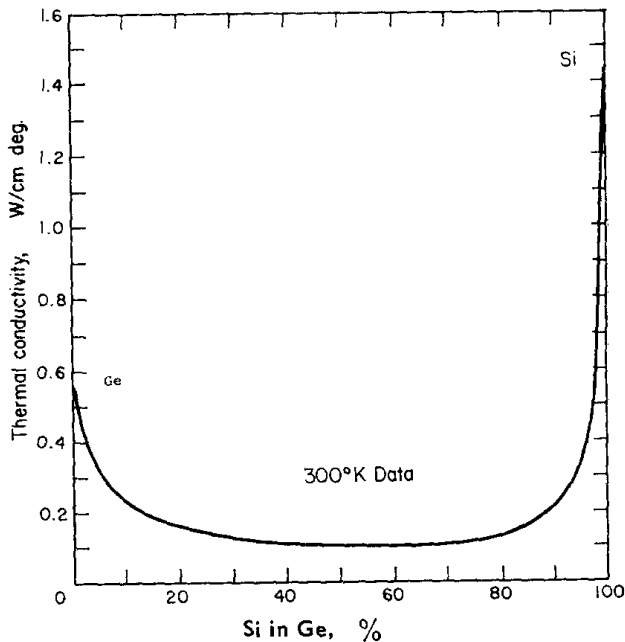


Figure 2.1: Thermal conductivity of Germanium as a function of percentage random substitution of Silicon taken from Ref. [16].

of sound in the solid, θ_D is the Debye temperature. The variable $x = \hbar\omega/k_B T$ is best described as a frequency (ω) dependant quantity, τ is the total relaxation time of the phonons. By assuming that all scattering processes are independent of each other, Mathiessen's rule [7, 13] can be used to express the relaxation time as

$$\frac{1}{\tau} = \frac{1}{\tau_U} + \frac{1}{\tau_N} + \frac{1}{\tau_b} + \frac{1}{\tau_p}. \quad (2.2)$$

Here τ_U and τ_N represent the relaxation times due to umklapp and normal processes, respectively. These scattering types are predominately due to phonon-phonon interactions and at low temperatures phonon-phonon scattering rates are close to non-existent, therefore we take these relaxation times to be infinite [15]. The remaining contributions to the overall relaxation time come from boundary and particle (τ_b and τ_p) scattering and by increasing these rates, the associated relaxation times will reduce proportionately. This effectively reduces the overall relaxation time of the phonons and the thermal conductivity in Eqn. (2.1).

From Fig. 2.1 we see experimental evidence that with random substitution of Silicon into a Germanium substrate, the thermal conductivity of the sample is dramatically reduced. The minimum thermal conductivity achieved is at the highest

random doping level of 50%. In order to achieve desired thermal properties in disordered materials, where the thermal conductivity is governed by boundary and particle scattering, we must understand the characteristics of the underlying phonon modes and all mechanisms that affect them.

2.2 Anderson Localisation

Philip Warren Anderson’s original paper [17] entitled “Absence of diffusion in certain random lattices” saw him jointly lay claim to The Nobel Prize in Physics (1977). He shared the prize with Sir Nevill Francis Mott and John Hasbrouck van Vleck “for their fundamental theoretical investigations of the electronic structure of magnetic and disordered systems”. Not only did he receive one of the greatest accolades in Physics for this work, but he unleashed a major worldwide research field that even now, 54 years later, is still very much active. Anderson theorised that with the introduction of tiny modifications to a lattice, such as the introduction of impurities or defects, an electron that would normally move freely inside the solid no longer diffuses on the defects as expected but can be completely stopped. In a recent press release, Philippe Bouyer, an experimentalist in the field of Anderson localisation of matter waves [18] described an analogy of the phenomena as:

“On a macroscopic scale, [Anderson localisation] would be like saying that a few blades of grass scattered haphazardly over a golf course could completely stop a full-speed golf ball in its tracks.”

The majority of the research on Anderson localisation has been conducted in the field of electron transport, although it is now known to extend to classical waves and many varying experimental realisations. Nonetheless, the following theory will be presented in the framework of the original electronic theory [19, 20].

2.2.1 Theoretical Background of Anderson Localisation

In Anderson’s original work [17], it was stated that “the eigenfunctions [of the electrons] are localised if the ‘strength’ of the disorder exceeds some definite value”. Only later was it found by Mott [21] (and almost simultaneously Ziman [22]) that the transition also depends on the energy (spectral variable) of the electrons. Hence they theorised that the spectrum is divided by a *mobility edge* into regions where all states are localised or extended. There is no rigorous proof of the exact positions of the mobility edges but as in the three-dimensional Ising model [23], while the existence

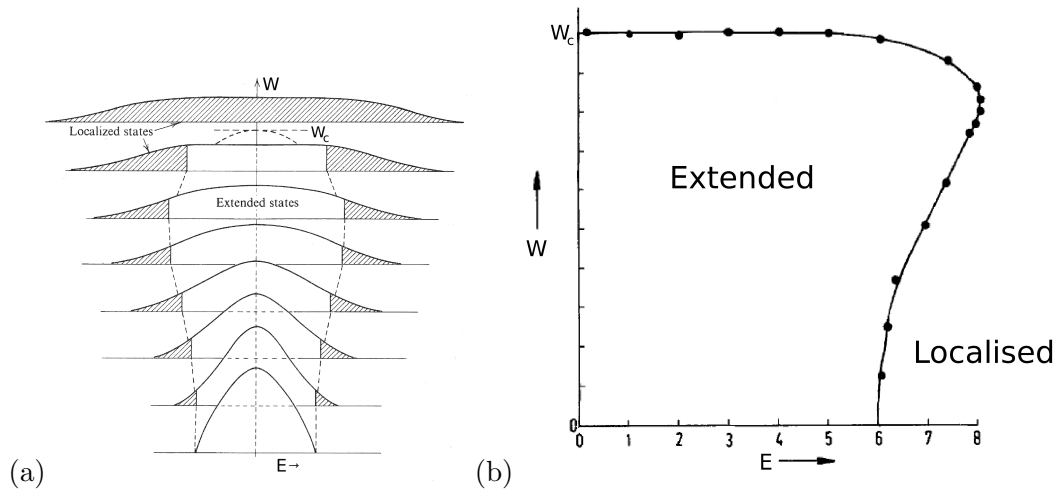


Figure 2.2: (a) Illustration of the electronic DOS as a function of electronic energy E and disorder strength W adapted from Ref. [24] and (b) phase diagram between extended and localised states adapted from Ref. [25].

of a phase transition is accepted the critical temperature for given scenarios is not analytically known and remains difficult to calculate.

The Anderson model (AM) neglects the effects of interactions such as the electron-electron and electron-phonon interactions and is only reasonable in a regime where all scattering is elastic ($\sim 10K$) and electrons are taken to be spinless particles. In most cases the AM involves solving the Schrödinger equation using a tight binding approximation with diagonal disorder. The diagonal disorder is applied to the diagonal terms within the Hamiltonian, which are linked to the potential at each lattice site. The Hamiltonian is of the form

$$\mathcal{H} = \sum_i \epsilon_i |i\rangle\langle i| + t_{ij} \sum_{i \neq j} |i\rangle\langle j| \quad (2.3)$$

where ϵ_i is the potential at lattice site i and t_{ij} is the hopping integral from site i to j . In the case of potential disorder, t_{ij} is constant and set to unity.

The disorder is introduced into the onsite potentials such that $\epsilon_i \in [-\frac{\mathcal{W}}{2}, \frac{\mathcal{W}}{2}]$, where \mathcal{W} is known as the ‘strength’ of the disorder and is usually symmetric around $\epsilon = 0$. As an illustration, we show the effect on the electronic DOS and the mobility edges for increased disorder in Fig. 2.2. We can see that when the trajectory of the mobility edges from Fig. 2.2(a) are plotted as a function of disorder strength \mathcal{W} we obtain the phase diagram in Fig. 2.2(b) which is symmetric around $E = 0$. Most research in the field of the AM is based around electrons with $E = 0$ and close to the

phase boundary as not only is there a LDT but the disorder required for a metal-insulator transition (MIT) can also be studied. It is assumed that when all electrons with $E = 0$ are localised, that the system has experienced a MIT. The exact disorder strength required for an MIT is of significant interest, where the current accepted value is $\mathcal{W}_c \approx 16.5$ without a magnetic field. It is also favourable to work in this region of the phase diagram as the DOS (as seen in Fig. 2.2(a)) is roughly constant or flat. This is advantageous when working with localisation properties as it has been shown to be more difficult to work in regions of fluctuating DOS [26].

2.2.2 Universality Classes, Renormalisation Group Theory and Scaling Theory

Renormalisation group theory is a tool to investigate the changes in a system when observed at varying length scales [27]. As the scale changes, it is as if the ‘magnifying power’ set upon the system is being altered. In these renormalisable theories [28,29], the system at one scale will generally be seen to consist of ‘self-similar’ copies of itself, when viewed at a smaller scale. The aim is to understand the behaviour of properties in the system as a function of the system size or of other scale variables [29].

Let us consider an observable of a physical system undergoing a renormalisation group transformation. The magnitude of the observable as the length scale of the system goes from small to large may be (a) always increasing, (b) always decreasing or (c) other, and these observables would be described as (a) relevant, (b) irrelevant and (c) marginal, respectively [30]. A relevant operator is needed to describe the macroscopic behaviour of the system. Irrelevant operators account for other systematic changes to the observable that occur in finite sized systems and have lesser influence when approaching the thermodynamic limit. Marginal observables may or may not need to be taken into account depending on the success of using only relevant and irrelevant variables. It is generally accepted that most observables are of the irrelevant type, and therefore the macroscopic physics is dominated by only a few relevant observables in most systems.

After Anderson’s original paper [17], the localisation problem was reformulated in terms of renormalisation group theory [31] and the non-linear sigma model (NL σ M) [32], before finally establishing that the MIT is a second order phase transition. Within a few years, in a very similar manner, John et al. [33] described the transition from extended to localised modes in an elastic medium using the NL σ M. They found that for phonons in a disordered system, all finite frequency modes in 1D and two-dimensions (2D) are localised, and in dimensions $d > 2$ there exists a mobility edge between extended and localised regimes.

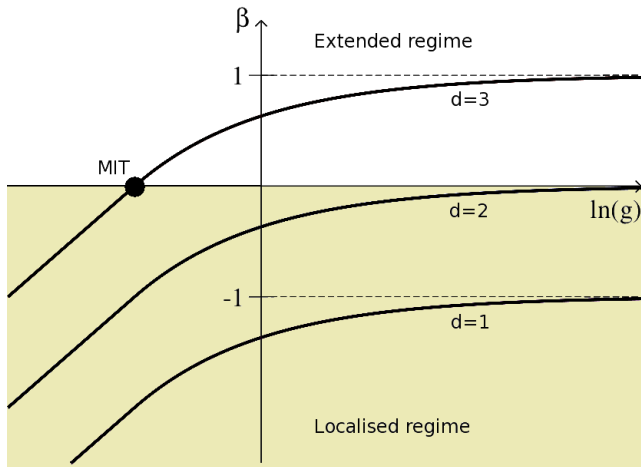


Figure 2.3: Schematic diagram of the scaling function β for dimensions $d = 1, 2$ and 3 . β describes with what exponent the average conductance g grows with system size L . We see that the transition occurs when $d = 3$ as β can be both positive and negative.

In the one-parameter electronic scaling theory [29] the conductance $g(L)$ of electrons was taken to be the only scaling variable. It was rightly pointed out that the DC conductivity vanishes in the localised regime and at absolute zero temperature it is no longer a useful quantity for the description of transport through finite sized systems [34]. The assumption was made that the quantity $\beta = \frac{d \ln(g)}{d \ln(L)}$ in a ‘hypercube’ of volume L^d depends solely on $g(L)$ and not separately on system size L , energy or disorder. The qualitative behaviour of the dependance of β upon g is given in Fig. 2.3 and was estimated by interpolating between the known forms of both large and small g [35]. At small g , where the disorder is sufficiently strong, the electronic states near the Fermi energy are localised and as such the electronic wave functions are exponentially localised. The conductance g assumes the form $g = g_0 \exp^{-L/\lambda}$ where λ is the localisation length and hence, $\beta(g) = \ln \frac{g}{g_0}$. In the large g regime we observe metallic behaviour so $g = \sigma L^{d-2}$, where σ is the conductivity and therefore $\beta(g) = d - 2$. We see in Fig. 2.3 that β is always negative for $d \leq 2$, and implies that an increase in system length L will drive 1D and 2D systems to an insulating regime. In the case of a 3D system, β is negative for small g and positive for large g , and where $\beta = 0$ (conductance is independent of system size) there is a MIT at a critical conductance g_c , so an increase in L can either drive the system to a metallic or insulating regime [36]. Therefore the main result of the one-parameter scaling law is that a MIT can only exist in 3D.

Near criticality the only relevant length scale is the localisation length λ in

the localised regime or the correlation length between wave function amplitudes in the extended regime. These length scales diverge near the MIT and since they can depend on either the disorder or the spectral variable they therefore diverge near some critical point as

$$\lambda = |w - w_c|^{-\nu}. \quad (2.4)$$

Here w represents either the applied disorder or a spectral variable (such as energy E for electrons or squared frequency ω^2 for phonons), w_c is the critical point of w , and ν is the critical exponent. To apply scaling theory, we disregard the irrelevant observables and group the macroscopic phenomena into a small set of universality classes, described by the set of relevant observables [37]. The value of ν defines the universality class of the Hamiltonian which can be either orthogonal, unitary or symplectic [37]. The properties of the relevant observables (and hence the critical exponent ν) are governed by the fundamental symmetries of the Hamiltonian with respect to time reversal and spin rotation [38] and can be altered, for example, by the application of an external magnetic field. An external magnetic field destroys time reversal invariance and changes the universality class of the system along with the critical behaviour of the MIT [19].

In Sec. 6.3.1 we will see the numerical application of renormalisation group theory and scaling to obtain the critical exponent of the transition from extended to localised states.

2.2.3 Experimental Observations

Experimental work on localisation due to disorder has been a very active field in recent years and mainly focussed on localisation phenomena in new and unique experimental assemblies. Initial attempts to observe localisation were based entirely around electronic systems of ever decreasing dimensionality (where localisation effects are strongest) such as narrow wires and semiconductor channels [39, 40]. The critical exponent of the MIT was first measured as $\nu = 0.51 \pm 0.05$ [41], yet early numerical studies predicted $\nu > \frac{2}{3}$ [19]. The experimental problems were formidable and thought to be a direct consequence of the finite temperatures of the systems. Imprecise corrections were applied to results to account for effects associated with finite temperatures (e.g. inelastic scattering), but even so extrapolation of the measured conductivity to zero temperature still only recovered a critical exponent of $\nu \approx 1$.

Scaling theory was experimentally verified for the integer quantum Hall effect [42]. Due to a theoretical link established between the quantum Hall critical

exponent and the inelastic-scattering/localisation length exponents [43], and similarly due to the universal nature of the exponents [44], scaling theory also holds for Anderson localisation.

John et al. [33] reformulated the theory of Abrahams et al. [29] for an elastic medium to find that in $d < 2$ all finite frequency excitations are localised in line with the electronic theory. A year later John predicted that a frequency regime exists in which electromagnetic waves localise [45].

Due to the relative difficulties of observation of electron localisation, analogous classical wave systems were sought. The advantage of classical waves, such as photons, is the inherent lack of interactions and controllability in a room temperature environment. In all classical wave cases the spectral variable is frequency (as opposed to the electron energy), and transmission of classical waves as a function of system size is usually straightforward to measure. The drawback of such systems include; the inability for low frequency waves to localise as their mean free paths become comparable to the system size and the lack of theoretical estimates of the location of a LDT.

In one of the first such experiments that attempted to build an analogy between the electronic and acoustic models, He and Maynard [46] demonstrated a 1D acoustic experiment in which localisation can be observed on a long wire of coupled masses and they attempted to study an analogy to the inelastic effects in the electron system by introducing strain into their wire. Later, after the theoretical framework set out by Economou and Soukoulis [47], light has been experimentally localised [48]. In 2008, Hu et al. [49] reported the localisation of ultrasound using a 3D elastic network of aluminium beads, and a Bose-Einstein condensate was shown to localise in a quasi-1D optical lattice [50]. Similarly, matter waves were spatially localised in 1D systems of ultra cold atoms [18, 50]. Gases of ultra cold atoms have the potential to be used as quantum simulators and with advances in the experimental control of such systems [51] we can experimentally mimic theoretical Hamiltonians of realistic quantum systems without the inclusion of the interaction effects that would usually mask the critical transitions.

2.3 Crystal Dynamics and the Canonical Equation

Consider a crystalline lattice composed of N lattice sites, each of which is an equilibrium position for an atom/molecule, henceforth referred to as the ‘masses’. If the lattice is rigid, the constituent masses in the bulk must be exerting forces on one-another to keep them all in/near their equilibrium positions. The forces acting

between the masses are generally due to the Coulomb interaction and may be one of many types, for example Van der Waals forces, covalent bonds and/or electrostatic attractions. The force between each pair of masses within the crystalline lattice may be characterised by a potential energy function ν that depends on the distance of separation of the atoms. The potential energy of the entire lattice is the sum of all pairwise potential energies

$$\mathcal{V} \approx \sum_{i < j} \nu(r_i - r_j)$$

where r_i is the position of the i^{th} atom.

The inclusion of *all* interactions/forces in any many-body problem dramatically increases the complexity and difficulty of a solution. To simplify the model we make the approximation that only the forces applied to each particle are exerted by others in the direct vicinity of said particle. Although the electric forces in real solids extend to infinity, we assume that the fields produced by distant particles are screened by those nearest to the particle in question [52]. Therefore the above summation is only performed over the nearest neighbours sites in the lattice.

We consider a crystal lattice as a series of atoms in unit cells that exhibit translational periodicity in all directions. Each atom is made up of an ion core and surrounding valance electrons. To begin to derive our crystal dynamics equations, we first simplify our system by applying the ‘adiabatic approximation’ [15], where the motion of the ion cores at each lattice site is determined in a potential field generated by the *average* motion of the electrons. Due to the ion cores being much heavier than the electrons, their motion can be treated separately.

We now consider the total potential energy \mathcal{V} of a crystal as a function of the instantaneous position of all atoms. We use the label p for atoms per unit cell, and let $\mathbf{u}(lb)$ represent the displacement of the b^{th} atom in the l^{th} unit cell. We expand \mathcal{V} in a Taylor series in powers of the atomic displacement $\mathbf{u}(lb)$ such that

$$\mathcal{V} = \mathcal{V}_0 + \underbrace{\sum_{lb\alpha} \frac{\partial \mathcal{V}}{\partial \mathbf{u}_\alpha(lb)} \bigg|_0}_{\mathcal{V}_1} \mathbf{u}_\alpha(lb) + \underbrace{\frac{1}{2} \sum_{lb, l'b'} \sum_{\alpha\beta} \Phi_{\alpha\beta}(lb; l'b') \mathbf{u}_\alpha(lb) \mathbf{u}_\beta(l'b')}_{\mathcal{V}_2} + \dots \quad (2.5)$$

The zeroth order term \mathcal{V}_0 is disregarded as it is the equilibrium value and shifts the minimum value of the potential which is unimportant for dynamical problems. The first order term \mathcal{V}_1 is a force that disappears in the equilibrium configuration. The first significant term is \mathcal{V}_2 and consideration of this term alone is known as the ‘harmonic approximation’ [15]. This holds for small displacements (and there-

fore, low temperatures) as higher order terms are dependant on the displacement itself. $\Phi_{\alpha\beta}(lb; l'b')$ is given as

$$\Phi_{\alpha\beta}(lb; l'b') = \left. \frac{\partial^2 \mathcal{V}}{\partial \mathbf{u}_\alpha(lb) \partial \mathbf{u}_\beta(l'b')} \right|_0. \quad (2.6)$$

With the potential term ($\mathcal{V}_2 = \mathcal{V}_{\text{harm}}$), we can now see our generalised equation of motion is given as

$$m_b \ddot{\mathbf{u}}_\alpha(lb) = - \frac{\partial \mathcal{V}_{\text{harm}}}{\partial \mathbf{u}(lb)} = - \sum_{l'b'\beta} \Phi_{\alpha\beta}(lb; l'b') \mathbf{u}_\beta(l'b'), \quad (2.7)$$

and can be used for model systems that span any number of spatial dimensions.

Chapter 3

Numerical Diagonalisation

We will see in the following chapters that the system of equations for the motion of the lattice sites is assembled into an eigenproblem where the eigenvalues of the system λ are the negative of the squared frequencies ω , and the eigenvectors \mathbf{x} are the site displacements from equilibrium \mathbf{u} . The eigenproblem matrix for a phonon system is usually referred to as the ‘dynamical matrix’ \mathcal{D} and made up of spring constant and inverse mass matrices. Given a system of lattice sites where all mass and spring constant parameters are known, the dynamical matrix is constructed and diagonalised to obtain the normal modes and their frequencies. For the general discussions of diagonalisation techniques below, we use the symbol \mathbf{A} to represent the matrix to be diagonalised.

3.1 Dense Matrix Diagonalisation

The name ‘dense matrix routine’ is given to code packages that require the *entire* matrix for diagonalisation, as a two dimensional array. Generally such a routine is used for small eigenvalue problems, where either the input matrix is heavily populated with non-zero terms or where all eigenvalues/eigenvectors are required to be computed. The latter condition is a requirement for DOS and participation ratio (PR) calculations, as seen in Chaps. 5 and 8, respectively.

We employ the standard LAPACK [53] dense matrix routine (DGEEV) which is specifically designed to diagonalise real, double precision matrices. This is the most general routine as it is capable of diagonalising both non-symmetric (mass disorder) and symmetric (spring constant disorder) matrices. Dense matrix linear algebra is computationally expensive as it involves unnecessary computations due to the inclusion of zero valued matrix entries and memory intensive as the whole

input matrix is stored in memory with additional working memory for calculations. Further memory is also allocated for storage of the returned eigenvectors and eigenvalues. As with other eigenvalue problem solvers this routine returns the computed eigenvectors normalised to have Euclidean norm equal to one and largest component real, reducing the need for further computation.

LAPACK routines have been developed over many years to be extremely efficient and their use is now common practice in scientific computing. With any diagonalisation, there may well be some form of pre-conditioning or matrix manipulation that best suits the matrix structure making it more readily diagonalisable. Therefore the algorithms are very flexible and can be adapted with numerous input parameters. We direct the interested reader to the LAPACK users guide in Ref. [53] for a breakdown of additional options, and summarise only the main algorithm structure:

1. The general matrix \mathbf{A} is converted to upper Hessenberg form \mathbf{H} where all values below the first sub diagonal are zero and the conversion can be written as $\mathbf{A} = \mathbf{Q}\mathbf{H}\mathbf{Q}^T$ where \mathbf{Q} is orthogonal as \mathbf{A} is real.
2. The upper Hessenberg matrix \mathbf{H} is reduced to Schur form \mathbf{T} , giving the Schur factorisation $\mathbf{H} = \mathbf{S}\mathbf{T}\mathbf{S}^T$ and therefore the matrix of Schur vectors \mathbf{S} of \mathbf{H} may additionally be computed. The eigenvalues are obtained from the diagonal of \mathbf{T} .
3. Given the eigenvalues, the eigenvectors may be computed in two different ways. Either performing an inverse iteration on \mathbf{H} to compute the eigenvectors of \mathbf{H} , which can then be used to multiply the eigenvectors by the matrix \mathbf{Q} in order to transform them to eigenvectors of \mathbf{A} . Alternatively the eigenvectors of \mathbf{T} are computed and transformed to those of \mathbf{H} or \mathbf{A} if the matrix \mathbf{S} or $\mathbf{Q}\mathbf{S}$ is supplied.

3.2 Sparse Matrix Diagonalisation

In cases where the full set of eigenvalues/eigenvectors is not required, sparse matrix diagonalisation techniques become favourable. Sparse matrix techniques usually only find one to a few eigenvalues (and/or eigenvectors) of a matrix close to a pre-decided eigenvalue target. The benefit of such diagonalisation packages is that their memory requirements and computational costs are far less demanding and therefore much larger input matrices (system sizes) are diagonalisable.

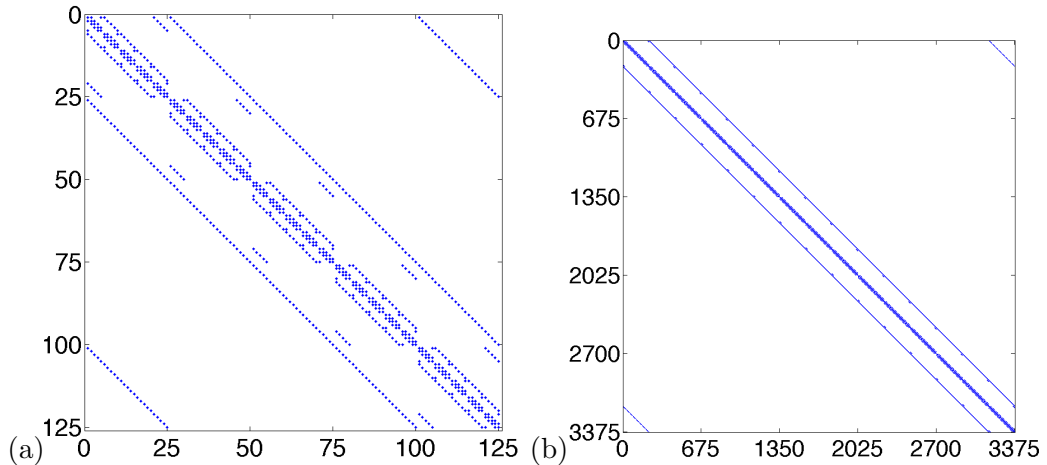


Figure 3.1: Arrangement of non-zero terms in dynamical matrices for 3D periodic systems of size (a) $L^3 = 5^3$ and (b) $L^3 = 15^3$. The axis labels are the site indices of the system and each blue dot represents a non-zero data entry.

Research in 2006 on the tight binding Anderson model of electron localisation pushed the limit of achievable system size to a cube of 350^3 sites for which an electron wave function at the MIT was calculated [54]. This world record required the use of a machine with 96GB of memory for three whole days in order to obtain a single state. In this study we aim for a more modest matrix size due to the quantity of required states, time limitations and memory restrictions.

3.2.1 Sparse Matrix Structure

We note that in a periodic 3D simple cubic structure each site is connected to exactly six others. Therefore each row in the dynamical matrix will contain seven terms; six neighbours and itself. As this figure is constant we know that the number of non-zero matrix entries increases linearly with lattice sites. The number of overall matrix entries increases quadratically with the number of lattice sites. Therefore, the level of sparsity (percentage of zero terms) in the matrix grows substantially as the matrix increases in size. To illustrate this we plot the positions of matrix entries for two dynamical matrices in Fig. 3.1 for systems of size $L^3 = 5^3$ and $L^3 = 15^3$. The blue spots illustrate the positions of non-zero terms and as the matrix size increases the percentage of non-zero matrix entries decreases rapidly. We see in this example that the level of sparsity is much higher for an unexceptionally larger system size.

One of the advantages of sparse matrix diagonalisation is the storage methods. We only store non-zero values and for a symmetric matrix, just the non-zero

values in the upper triangular part of the matrix. This is achieved with the construction of three vectors; the first vector contains all non-zero matrix entries as a list in row major order. The second vector contains pointers in the same positions as the matrix entries of the first vector, indicating the column index for the values. The third vector contains pointers to the column indices of the second vector, that signify where a new row begins. This simple storage solution dramatically reduces the required memory compared to that of the dense matrix storage arrays. This type of matrix storage is conventionally known as ‘compressed row storage’ [55].

3.2.2 Power Method and Krylov Subspace

There are many iterative methods for the calculation of the dominant eigenvalue of a matrix, each tailored to a particular matrix structure. For example, the Arnoldi iteration method [56] finds eigenvalues of general matrices, whereas the Lanczos iteration method [57] works only with Hermitian matrices. All of these methods are in essence optimised adaptations of the power method [55].

The power method will generate the largest eigenvalue of a matrix \mathbf{A} . It only interacts with the matrix \mathbf{A} using a matrix-vector product. We start with an arbitrary vector and repeatedly calculate the matrix-vector product. Once converged and normalised the resultant vector will correspond to the dominant eigenvalue of the matrix $x^{(0)}$, the eigenvalue of largest magnitude. We first assume that the arbitrary initial vector is a linear superposition of the eigenvectors x of the matrix \mathbf{A} , therefore

$$x^{(0)} = \sum_j \alpha_j x_j, \quad (3.1)$$

where α_j is a set of linear coefficients. Multiplication by matrix \mathbf{A} gives

$$\mathbf{A}x^{(0)} = \mathbf{A} \sum_j \alpha_j x_j = \sum_j \alpha_j \mathbf{A}x_j = \sum_j \lambda_j \alpha_j x_j \quad (3.2)$$

and therefore after k matrix-vector multiplications we have

$$\mathbf{A}^k x^{(0)} = \mathbf{A}^k \sum_j \alpha_j x_j = \sum_j \alpha_j \mathbf{A}^k x_j = \sum_j (\lambda_j)^k \alpha_j x_j. \quad (3.3)$$

Where the final sum will be dominated by the value of the k^{th} power of the dominant eigenvalue. In practice all resultant vectors at every iteration stage are stored in a Krylov matrix \mathcal{K} . A Krylov matrix is a linear subspace spanned by a set of vectors produced by the first k powers of \mathcal{A} applied to the arbitrary starting vector [58],

such that

$$\mathcal{K}_k(\mathbf{A}, x^{(0)}) = \text{span}\{x^{(0)}, \mathbf{A}x^{(0)}, \mathbf{A}^2x^{(0)}, \mathbf{A}^3x^{(0)} \dots \mathbf{A}^{k-1}x^{(0)}\} \quad (3.4)$$

The columns of this matrix are not orthogonal, but we can orthonormalise via the GramSchmidt method. The resulting orthonormalised basis vectors are a basis of the Krylov subspace \mathcal{K}_k , and the vectors of this basis give a good approximation of the eigenvectors corresponding to the k largest eigenvalues of the matrix \mathbf{A} , for the same reason that $\mathbf{A}^{k-1}x^{(0)}$ approximates the dominant eigenvector.

3.2.3 Shift and Invert Methods

We can now find eigenvalues of the given matrix \mathbf{A} using computationally inexpensive iteration methods with low memory usage. Although this offers little advantage if we can only obtain the dominant eigenvalue of our matrix. We use a shift and invert scheme to ‘move’ the spectrum of eigenvalues, so that the eigenvalues of particular interest (close to an appropriately chosen shift σ), can be obtained. The shift is applied as

$$\mathbf{A}' = (\mathbf{A} - \sigma\mathbf{I})^{-1} \quad (3.5)$$

to produce matrix \mathbf{A}' , where \mathbf{I} is the identity matrix. The advantage of this method is that the eigenvectors of matrix \mathbf{A}' are the same as that of \mathbf{A} , although the eigenvalues are not. The relationship to obtain the original eigenvalues from the matrix \mathbf{A}' is,

$$\mu_i = (\lambda_i - \sigma)^{-1}, \quad (3.6)$$

where the μ 's are the eigenvalues of the matrix \mathbf{A}' . We note that although we can now access a specified eigenvalue, a matrix inversion is as computationally expensive as a full diagonalisation. We therefore perform the inversion outlined in Eqn. (3.5) by instead solving a system as a set of linear equations.

3.2.4 Linear System of Equations

The computational expense of matrix inversions is of the same order as diagonalisation. Computationally implementing the matrix inversion of Eqn. (3.5) would offer no speedup over the dense matrix diagonalisation outlined in Sec. 3.1.

We now denote n as some arbitrary vector encountered at some point during the iteration process outlined in Sec. 3.2.3. Say we apply a matrix-vector multiplication, yielding a vector m , both n and m will make up part of the Krylov subspace.

When implementing a shift and invert, we essentially perform the operation

$$m = (\mathbf{A} - \sigma \mathbf{I})^{-1} n. \quad (3.7)$$

To eliminate the requirement of the matrix inversion, we rewrite the operation as

$$n = m(\mathbf{A} - \sigma \mathbf{I}) \quad (3.8)$$

which is a linear system of equations that can be efficiently solved using iterative processes [54], where the only unknown is the vector m .

3.2.5 Code Packages

There are a multitude of packages available for sparse matrix diagonalisation which implement many different techniques and employ further optimisation strategies to improve computational efficiency. For both symmetric and unsymmetric dynamical matrices we use the ARPACK [55] and PARDISO [59] packages. ARPACK is based upon a modified Arnoldi process called the ‘implicitly restarted Arnoldi method’. PARDISO is an iterative linear system of equation solver and more information on the method used in this package is available in Ref. [54].

For the symmetric case alone, we attempted to use the all in one eigenproblem solver JADAMILU [60]. JADAMILU implements the Jacobi-Davidson method which has proved fruitful for the Anderson model [54], yet has proved to be memory intensive when attempting to diagonalise a dynamical matrix severely restricting the maximum system size achievable.

Chapter 4

One Dimensional Systems

The properties of 1D systems are studied as a starting point for any phonon investigation due to the minimal computational cost. Modelling a single site along a chain as rigid infinite planes of identical masses (planar force constant model [15]) thermal properties of higher dimensional systems can be crudely estimated. More recently, due to advances in semiconductor nano-structuring, 1D nano wires have become a topic of intense investigation [61] because of their enhanced thermoelectric figure of merit [62]. Treating 1D lattices with the classical model from Sec. 2.3 we visualise the admissible vibrational modes of the systems [63]. We verify computational techniques ready for application to 3D systems and observe the effect of disorder and low dimensionality on the normal modes of vibration.

4.1 Lattice Dynamics

We re-write Eqn. (2.7) for a 1D system with only nearest neighbour interactions that can be visualised as springs connecting masses in a chain. We now use a notation based on extension from equilibrium for the displacements of the sites. We make the analogy of the harmonic potential restoring the site to equilibrium as a spring with spring constant k . Therefore the equation of motion for a mass m at lattice site n (of a possible total N) is given as

$$m_n \frac{\partial^2 u_n}{\partial t^2} = k_{n+1}(u_{n+1} - u_n) + k_{n-1}(u_{n-1} - u_n), \quad (4.1)$$

where we have shortened the notation of the lattice site subscripts on the spring constants k to only include the site that n is connected to. u is the displacement and we seek solutions that satisfy Bloch's theorem to solve this equation. The form of this wavefunction is a consequence of the translational symmetry of the lattice.

It will therefore only have solutions at the sites of the masses [64], such that

$$u_n(t) = \bar{u}e^{i(qx - \omega t)}, \quad (4.2)$$

where ω is the angular frequency, t is time and \bar{u} is a universal amplitude, normally taken to be $N^{-\frac{1}{2}}$ for normalisation purposes [65]. q is the wave vector and x is equal to na where a is the lattice spacing and therefore the one-dimensional Bravais lattice vector is just $\mathbf{R} = na$. After solving Eqn. (4.1) and re-substituting (4.2) the following form is found:

$$-\omega^2 m_n u_n = k_{n+1}(u_{n+1} - u_n) + k_{n-1}(u_{n-1} - u_n). \quad (4.3)$$

To solve (4.3) for all N sites we arrange the system of equations into the general matrix equation $\mathbf{M}\ddot{\mathbf{U}} + \mathbf{C}\dot{\mathbf{U}} + \mathbf{K}\mathbf{U} = \mathbf{F}$ [66] with zero driving force \mathbf{F} and zero damping term \mathbf{C} , i.e. $\mathbf{M}\ddot{\mathbf{U}} + \mathbf{K}\mathbf{U} = \mathbf{0}$. We therefore arrive at the eigensystem

$$-\omega^2 \mathbf{U} = \mathbf{M}^{-1} \mathbf{K} \mathbf{U}, \quad (4.4)$$

with eigenvalues ω^2 , and eigenvectors \mathbf{U} . $\mathbf{M}^{-1} \mathbf{K}$ is called the dynamical matrix [15] and individually \mathbf{M} and \mathbf{K} are made up of all masses m and all spring constants k in the system, respectively. \mathbf{U} is a matrix containing all vibrational eigenvectors where each vector is used to plot displacements from equilibrium of all sites in the system for a particular normal mode. In a clean system, all masses are equal to a constant \bar{m} and all spring constants are \bar{k} .

4.1.1 Participation Ratios and Vibrational Density of States

When the eigenmodes are obtained, the vibrational density of states (VDOS) and PR are plotted to gain further insight into the properties of the system. The VDOS is essentially the number of normal modes per linear frequency interval. The PR [67] is plotted as a measure of localisation and is an estimate of the number of lattice sites contributing to a particular mode and therefore an indicator of the extension of the mode. The general form of the PR is given as

$$P_L(n) = \frac{1}{L \sum_{j=1}^L u_j^4(n)}, \quad (4.5)$$

where u_j is the displacement at site j , n is the mode number. L is the length of the system (as $d = 1$) and included as a normalisation condition, such that the PR is between zero (no participation) and one (full participation). As a direct consequence

of numerical diagonalisation the eigenstates are normalised such that the sum of the displacements squared is already unity. In situations where the states are yet to be normalised and in d dimensions the PR takes the more commonly seen form

$$P_L(n) = \frac{[\sum_{j=1}^{L^d} u_j^2(n)]^2}{L^d \sum_{j=1}^{L^d} u_j^4(n)}. \quad (4.6)$$

Throughout the rest of the 1D study, we use only P as opposed to P_L for the PR as in all cases we study chains of constant length $L = 1000$.

4.2 Binary Disorder

We attempt to introduce random disorder of the ‘binary’ type, whereby a particular percentage of the host mass \bar{m} in a chain is randomly exchanged for another mass \bar{M} . In the chain of masses we select the mass on each site randomly such that we are left with a particular percentage $\mathcal{P}\%$ of \bar{m} masses and $(100 - \mathcal{P})\%$ of \bar{M} , where \mathcal{P} is the ‘doping’ percentage. Since the system is of a random nature, we are required to repeat and average the calculations for a multitude of disorder realisations to obtain statistics for the normal modes as each realisation of the same doping percentage may yield very different results.

We work with the integer mass ratio $\frac{\bar{m}}{\bar{M}} = 3 \approx \frac{\text{Ge}}{\text{Si}} = 2.6$ as this is the closest integer ratio to the most commonly used ratio in experimental semiconductor physics. Experimental physicists favour Ge and Si due to the high-quality growth of multilayer structures by silicon molecular-beam epitaxy [68]. The VDOS in Fig. 4.1 at $\mathcal{P} = 0$ and 100% is the usual expected horseshoe shape for the monatomic chains containing only masses \bar{m} and \bar{M} , respectively [69]. For the intermediate doping percentages we have peaks in the high frequency regions where optical phonons reside and the upper part of the acoustic branch being smeared out. As the frequencies of the normal modes vary between disorder realisations, we must average the PR within the frequency domain. We choose to use the same bin widths as used in the VDOS calculations and take the mean of the PRs in each bin, this is plotted as Fig. 4.1(b). As expected none of the optical modes have a high PR. We observe a dramatic drop in PR for high frequency acoustic modes for all doping percentages. This is consistent with the scaling theory of localisation, where for 1D systems at the thermodynamic limit all finite frequency modes are localised regardless of the magnitude of disorder, yet the zero frequency mode is unaffected by the disorder.

To reduce the thermal conductivity of crystalline lattices at low temperatures the low frequency PRs must also be reduced. Within this small example we have

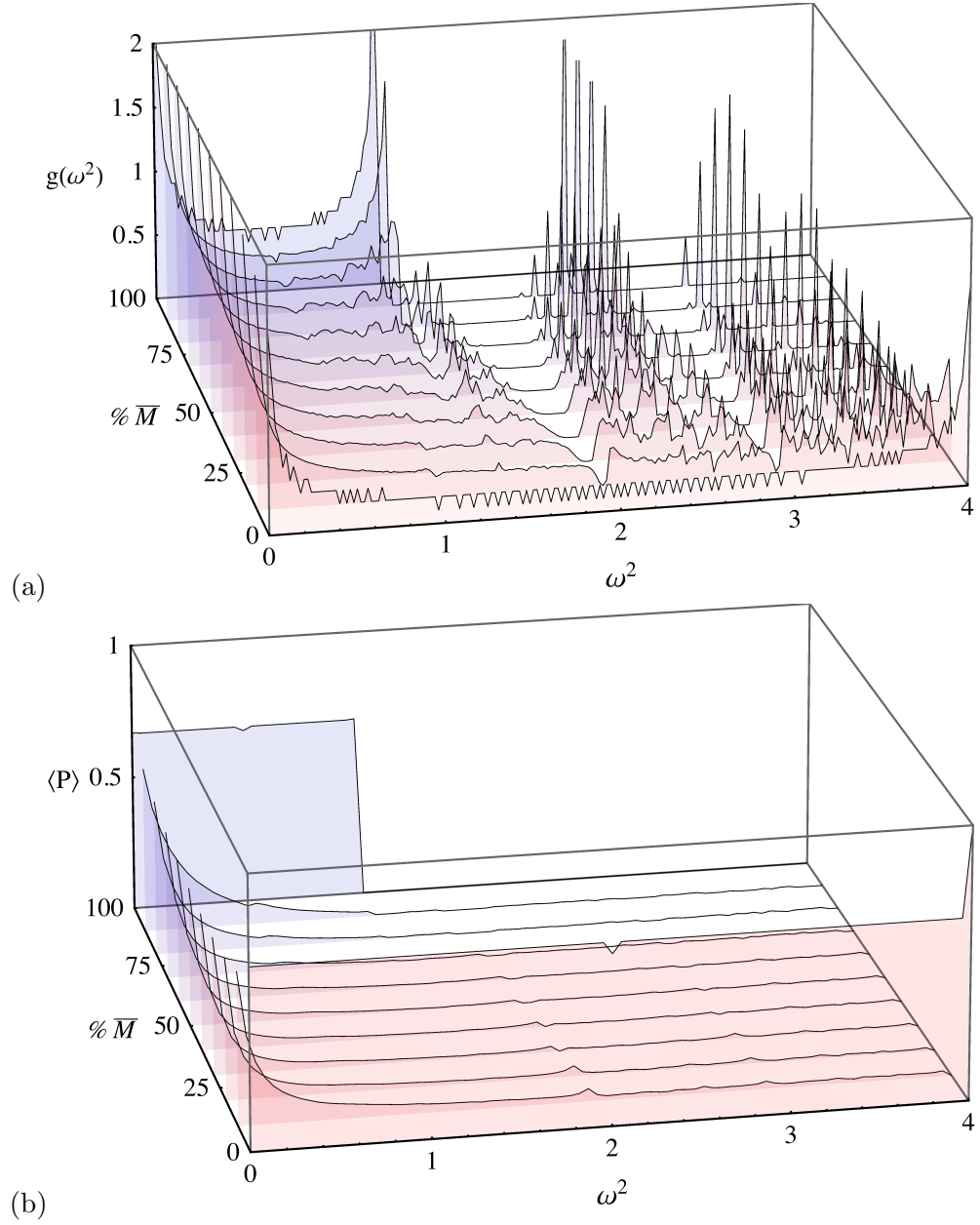


Figure 4.1: (a) VDOS and (b) PR as functions of ω^2 and doping levels of \bar{M} for a chain of length $L = 1000$. Results are averaged over 100 disorder realisations.

already applied the maximum possible binary disorder with a doping level of 50% and therefore cannot further affect the modes. We have seen similar reduction of PRs for all magnitudes of applied disorder and for these reasons it appears that with binary disorder there is no possibility of engineering any further reductions.

4.3 Fibonacci Series

It has recently been reported [70,71] that a Fibonacci superlattice can filter/localise phonons and cause a dramatic reduction in thermal conductivity of a crystalline solid by inducing band gaps in the VDOS. The superlattice consists of layers of a particular thickness of identical atoms stacked in a Fibonacci sequence. The sequence of layers is constructed with an initial condition (start with layer ‘A’) and for every increase in Fibonacci number F_n , two rules are applied,

$$A \rightarrow B \quad \text{and} \quad B \rightarrow BA. \quad (4.7)$$

To illustrate, after eight iterations we have a random sequence of 21 digits made up of only two characters, it is as follows: *BABBABABBABBABABBABAB*. Now say that we produce a material made of 21 deposited layers of identical thickness that followed this pattern, where a *B* would be a layer of Silicon and *A* would be Germanium, we would have a Fibonacci superlattice.

Typically, perfect Fibonacci superlattices are modelled. Therefore, each layer in the superlattice would contain an exact number of lattice sites, each occupied with the identical masses, either \bar{m} or \bar{M} (for layers *A* and *B*, respectively). We conversely propose modelling Fibonacci superlattices of constant length, say 1000 sites. In real life applications, we are generally limited to systems of a defined thickness, as opposed to number of layers in the superlattice. We divide the length of the system by the number of layers required for each Fibonacci chain, this results in a non-integer layer thickness. The number of sites in each layer is determined by cumulative rounding of the remainder of the non-integer layer thicknesses and results in a Fibonacci superlattice where the layer thickness randomly varies by a maximum of a single lattice site throughout the system. We use this method as it is more representative of a real life semiconductor deposition, as each layer cannot be guaranteed to contain an identical number of lattice sites but is of the same general thickness [10].

We simulate the Fibonacci chain for Fibonacci numbers F_n for $n = 8, 9, 10, 11$ and 12 that correspond to 21, 34, 55, 89 and 144 layers, respectively. We plot the VDOS and PR for these chains in Figs. 4.2(a) and (b) and find that for increasing

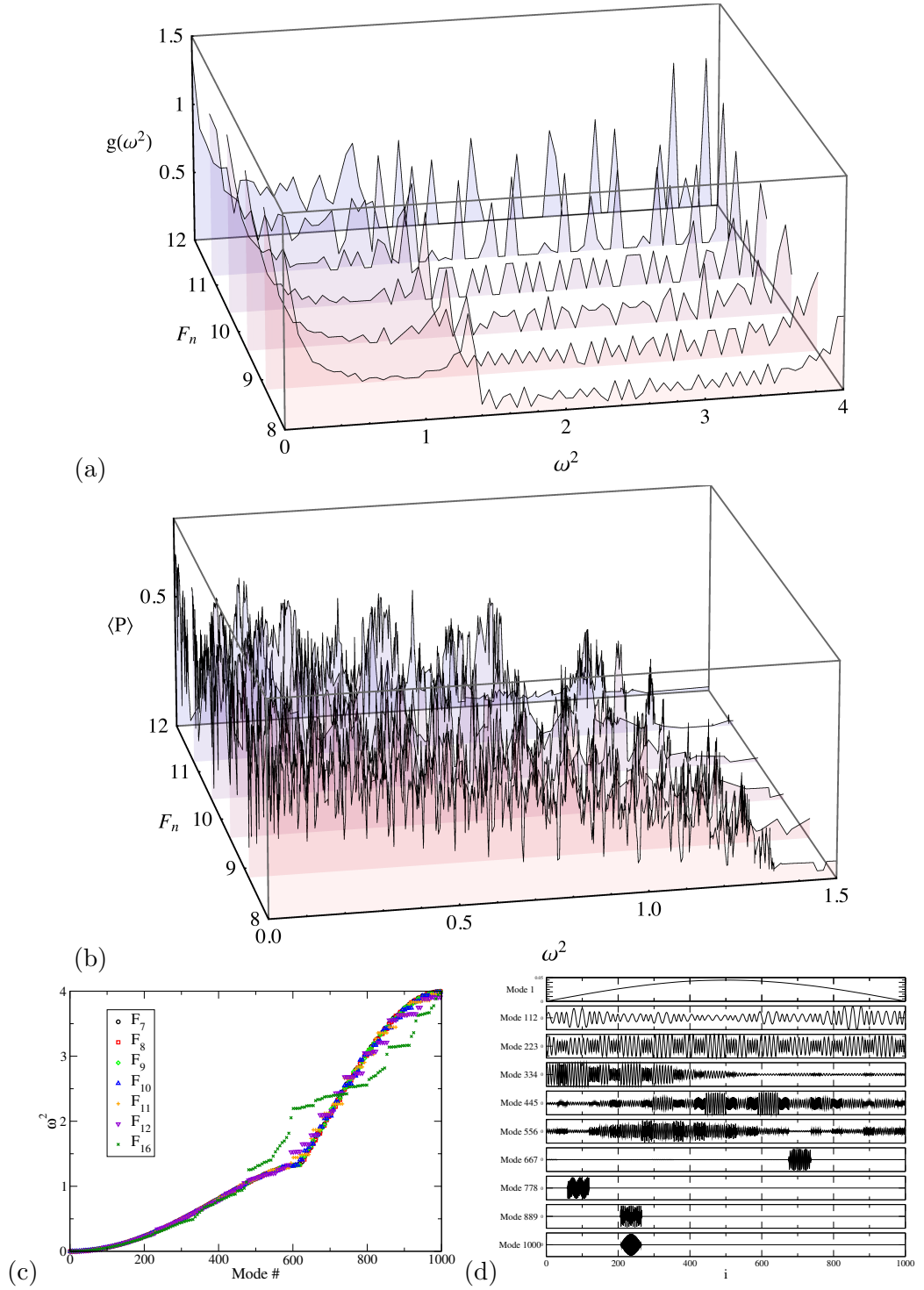


Figure 4.2: The (a) VDOS, (b) PR, (c) effective dispersion relation and (d) ten evenly distributed normal modes for Fibonacci chains of length $L = 1000$ with alternating layers of masses \bar{m} and \bar{M} according to the Fibonacci sequences for Fibonacci numbers F_n where $n = 8 - 12$ (and additionally 16 in (c)). Normal modes in (d) are for $n = 9$.

Fibonacci number we see spreading of the acoustic modes to higher frequencies, with the introduction of band gaps. As the Fibonacci number is increased we begin to have more well defined peaks in the optical part of the spectrum. The grouping of modes with similar frequencies in the high frequency regime can be seen in the step like structures of the dispersion relations in Fig. 4.2(c). The steps are flat and therefore the group velocity of the phonons here is approaching zero. The main feature of the PR plot is that for any number of Fibonacci layers there is enhanced reduction for the PR in intermediate frequencies of the acoustic spectrum. Although advantageous in some sense for filtering a particular part of the spectrum, it is clear that there is no Fibonacci sequence where *all* modes see a reduction. Connecting a series of Fibonacci superlattices as a series of band stop filters is not possible. The bond between adjacent Fibonacci lattices will redefine the structure as a collective lattice for which the preceding results are obsolete.

In the Fibonacci lattices dispersion relations, we observe a kink, below which the acoustic modes seem unaffected by the disorder. Beyond the kink the dispersion relations have band gaps where modes of similar frequencies have collected in regions of lighter mass, leading to phonon confinement. This is observed in the plots of the ten evenly spaced normal modes in Fig. 4.2(d) for the Fibonacci lattice of number $F_n = 9$ with 34 A and B layers.

Additionally in the dispersion relation in Fig. 4.2(c) we plot the results for a Fibonacci sequence F_{16} . This sequence contains 987 layers and can be considered to be an extreme case whereby mimicking, at some level, binary disorder. We see in the comparison of effective dispersion relations, that the binary disorder has the largest effect on the smoothness of the dispersion and therefore more detrimental to the overall mode extension.

4.4 Uniform Disorder

We have confirmed in the preceding sections that disorder does produce localisation effects in 1D harmonic systems for different disorder types. We have seen that although quasi-periodic disorder produces interesting features in all aspects of analysis, purely random disorder is more likely to have a greater effect on all modes within the system, rather than just modes within a select frequency band. Binary disorder does show promising localisation capabilities, although the degree of disorder that can be applied is limited. We have shown that the inclusion of interfaces or scattering centres can confine the phonon modes and the greater the mismatch of successive lattice sites the higher likelihood of localisation. In a binary lattice, the

transfer from one site to the next is restricted to only one of four options ($\bar{m} \rightarrow \bar{m}$, $\bar{m} \rightarrow \bar{M}$, $\bar{M} \rightarrow \bar{M}$, $\bar{M} \rightarrow \bar{m}$). The possible number of transfer types can be significantly increased by introducing uniform disorder, by which every mass (or now every spring constant) in the system is distributed within a uniform box distribution of width Δm (or Δk).

We allow the masses to vary such that $m_n \in [\bar{m} - \Delta m/2, \bar{m} + \Delta m/2]$ or the spring constants $k_n \in [\bar{k} - \Delta k/2, \bar{k} + \Delta k/2]$. For simplicity, we will use the *uniform* mass and spring constant distributions with mean $\bar{m} = \bar{k} = 1$ and restrict our investigation to the cases of either pure mass or pure spring constant disorder. Already these two cases permit interesting scenarios, e.g. in the strong disorder limits of $|2\Delta m| > \bar{m}$, with negative masses, or $|2\Delta k| > \bar{k}$ with negative spring constants. In addition, we have $(\mathbf{M}^{-1}\mathbf{K})^T = \mathbf{K}\mathbf{M}^{-1}$ and hence the dynamical matrix $\mathbf{M}^{-1}\mathbf{K}$ is not necessarily symmetric for mass disorder although the ω^2 values will remain real. Normally, these scenarios are only considered permissible, so long as the system remains ‘stable’ [72,73], such that no negative eigenvalues are present. Recently, some interesting new avenues of research have opened for which stability is no longer a necessity. Due to the seminal work on electromagnetic metamaterials [74] companion acoustic systems have recently been realised e.g. in the form of an array of sub wavelengths Helmholtz resonators [75]. Research in 1D disordered acoustic metamaterials is in its infancy but the hope is that loss of translational invariance via disorder will lead to highly localised modes [76]. We present typical results for (a) VDOS, (b) PR and (c) effective dispersion relations in Figs. 4.3 and 4.4, for mass and spring constant disorder, respectively. We see from the VDOS that spreading occurs and more higher frequency modes are available in both cases. The available frequencies differ between mass and spring constant disorder distributions as the maximum frequency limit is proportional to the positive portion of the spring constant distribution and inversely proportional to the negative portion of the mass disorder distribution and calculated as $\omega_{\max}^2 = 4\bar{k}/\bar{m}$ [77]. As disorder increases, the mass disordered frequency limit increases at a much greater rate and the limit completely disappears at $\Delta m > 2$. This is evident in the effective dispersion relations in Figs. 4.3(c) and 4.4(c). We now see the best evidence in the PR spectra (Figs. 4.3(b) and 4.4(b)) that all finite frequency modes are localised for any level of disorder in 1D systems, so long as the system is large enough, in line with the scaling theory of localisation. Additionally, the zero frequency mode has a PR of 1 for all disorder magnitudes.

To gain further insight into the localisation properties of phonons in 1D systems, we use the TMM. We rearrange the canonical equation for the 1D system

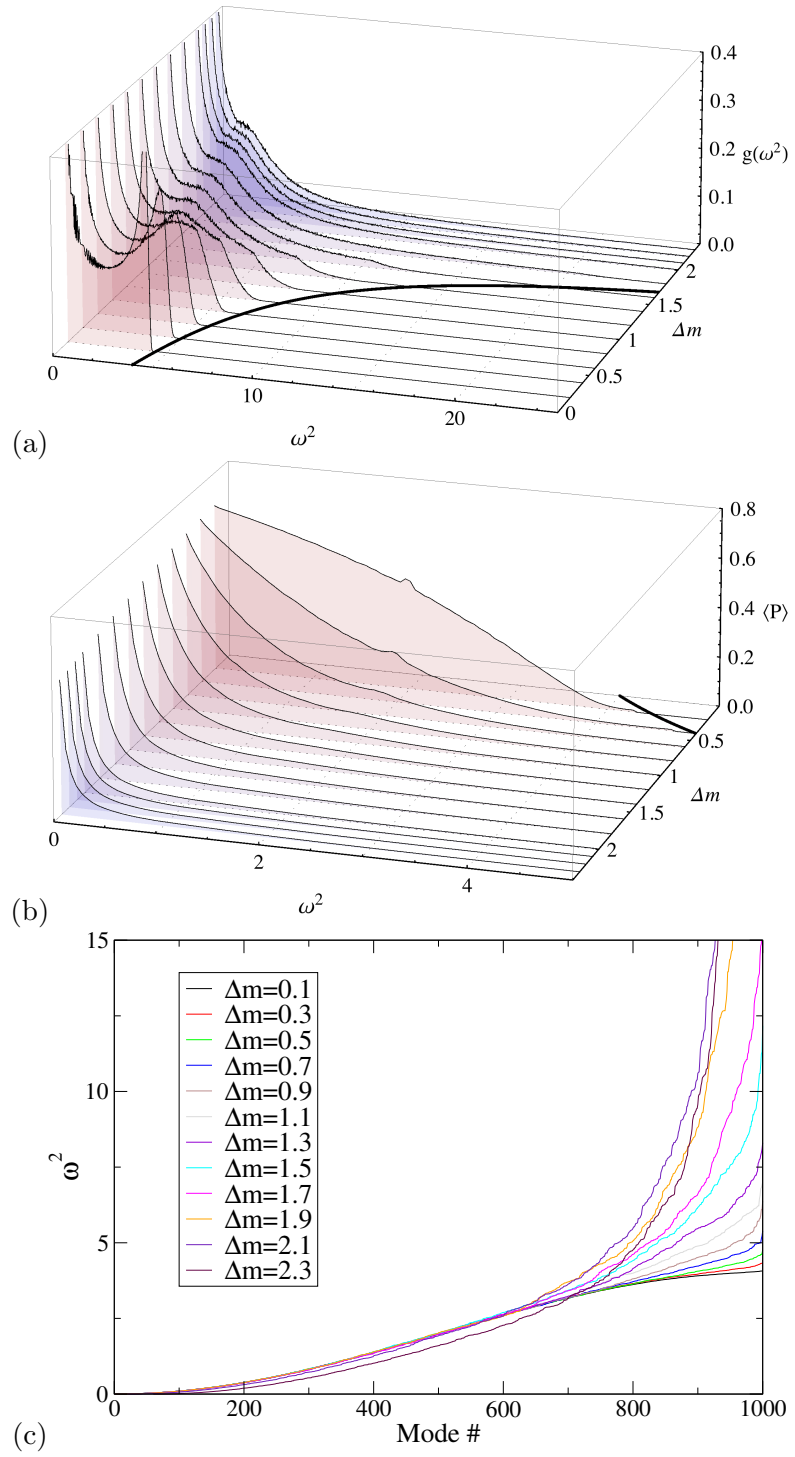


Figure 4.3: The (a) VDOS, (b) PR and (c) effective dispersion relation for chains of length $L = 1000$ with varying masses according to a box distribution of width Δm .

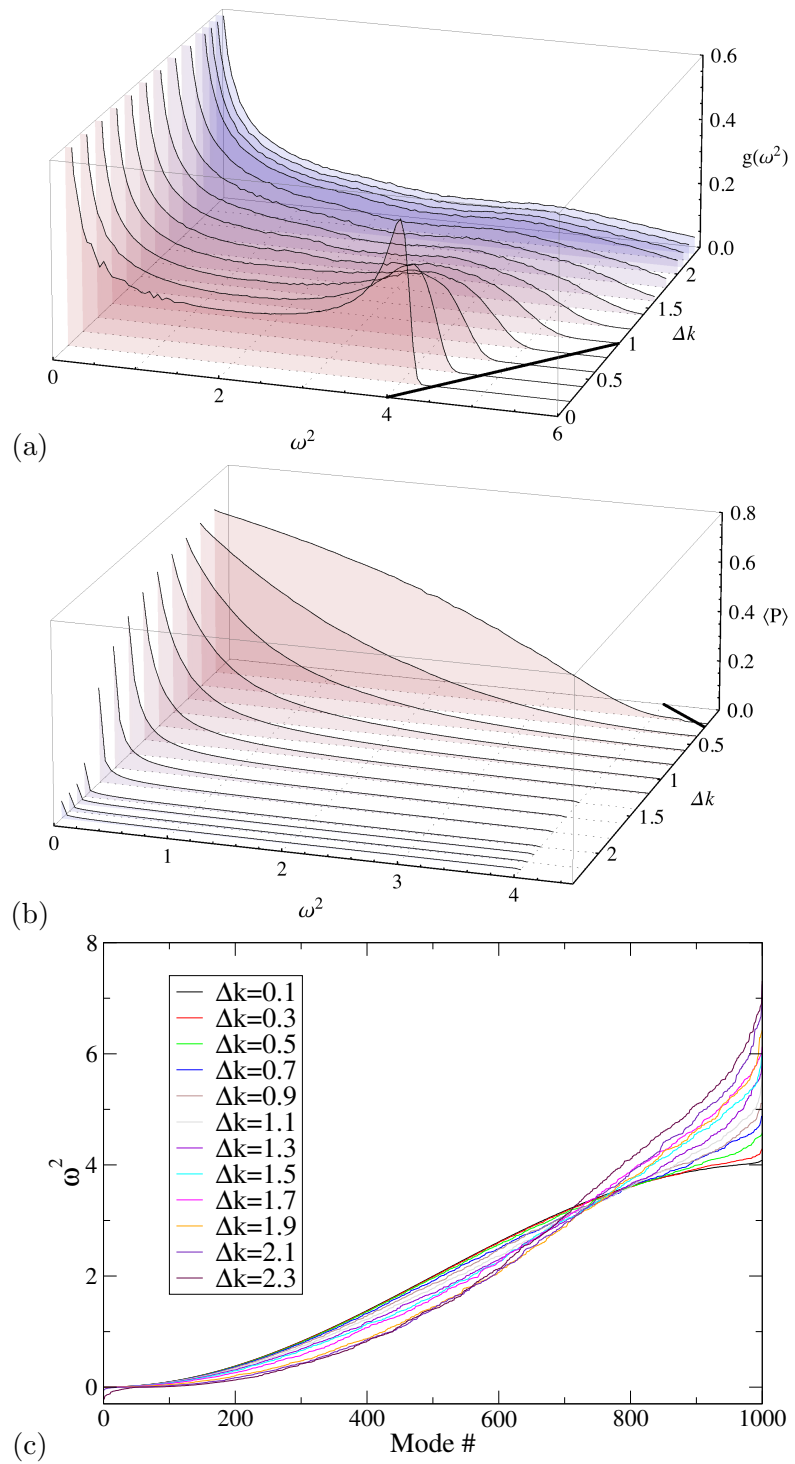


Figure 4.4: The (a) VDOS, (b) PR and (c) effective dispersion relation for chains of length $L = 1000$ with varying spring constants according to a box distribution of width Δk .

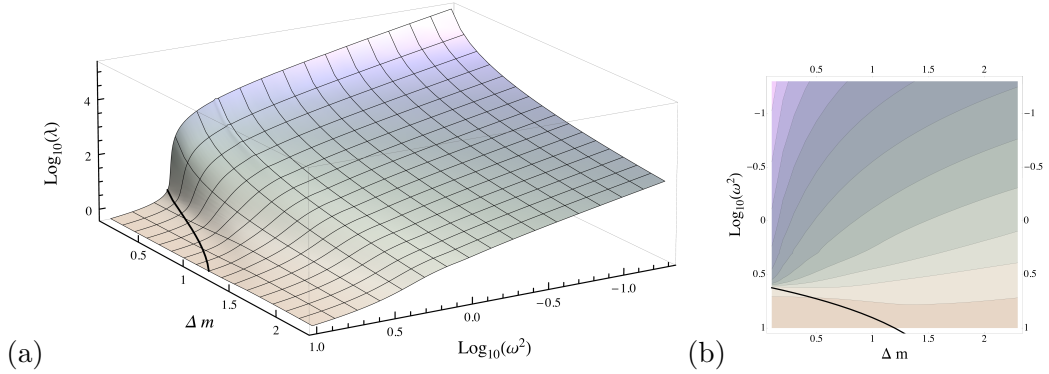


Figure 4.5: Localisation lengths of phonons in a 1D chain with the inclusion of uniform box distributed mass disorder plotted as a (a) function of frequency ω^2 and disorder Δm in a 3D plane and (b) contour plot. Each contour has the localisation length value of $\log_{10} i$ where i runs from 0.5 to 5 in half integer intervals. The thick black line represents the band edge.

in Eqn. (4.3) such that the amplitude of vibration of the oncoming site is calculated from the previous and current site. We find the rearranged form as

$$u_{n+1} = \frac{1}{k_{n+1}} [(-\omega^2 m_n + k_{n+1} + k_{n-1})u_n - k_{n-1}u_{n-1}]. \quad (4.8)$$

This translates directly to a matrix form, such that

$$\begin{bmatrix} u_{n+1} \\ u_n \end{bmatrix} = \underbrace{\begin{bmatrix} \frac{-\omega^2 m_n + k_{n+1} + k_{n-1}}{k_{n+1}} & -\frac{k_{n-1}}{k_{n+1}} \\ 1 & 0 \end{bmatrix}}_{\mathbf{T}_n} \begin{bmatrix} u_n \\ u_{n-1} \end{bmatrix}. \quad (4.9)$$

Formally, the transfer matrix \mathbf{T}_n is used to ‘transfer’ vibrational amplitude u from one slice to the next and repeated multiplication of \mathbf{T}_n gives the global transfer matrix $\tau_L = \prod_{n=1}^L \mathbf{T}_n$. The limiting matrix $\Gamma \equiv \lim_{L \rightarrow \infty} (\tau_L \tau_L^\dagger)^{\frac{1}{2L}}$ exists [78] and has eigenvalues $e^{\pm\gamma}$. The inverse of the positive Lyapunov exponent γ gives an estimates of the localisation length of the system λ .

We will see in Chap. 6 how the TMM is a memory efficient method for calculation of localisation lengths in a 3D system. Here the TMM is a convenient method where the length of the system is not required to be pre-defined and we can continue transfer matrix multiplications until convergence of the Lyapunov exponents to a desired accuracy is achieved. The estimated localisation lengths are plotted for mass (Fig. 4.5) and spring constant (Fig. 4.6) disorder as functions of ω^2 . We

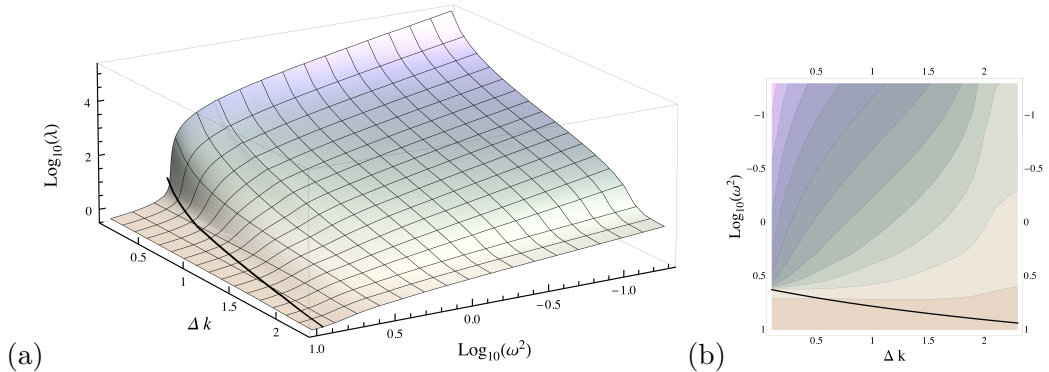


Figure 4.6: Localisation lengths of phonons in a 1D chain with the inclusion of uniform box distributed spring constant disorder plotted as a (a) function of frequency ω^2 and disorder Δk in a 3D plane and (b) contour plot. Each contour has the localisation length value of $\log_{10} i$ where i runs from 0.5 to 5 in half integer intervals. The thick black line represents the band edge.

note that for $\omega^2 = 0$ there is no convergence of the Lyapunov exponents for any of the studied disorder magnitudes. This indicates that all zero-frequency modes are extended for all disorder magnitudes, in line with previous studies [33, 79–82]. This is a well known attribute of the zero-frequency mode, also known as the Goldstone mode. We also see that for low frequency ($\omega^2 \rightarrow 0$) and low disorder modes, the localisation lengths diverge and are in the order of tens of thousands of lattice spacings, far larger than the chain of 1000 sites used in the diagonalisation study.

We see in the extremes of weak disorder and low frequency ω^2 , the localisation lengths λ for both types of disorder (Δm and Δk) are indistinguishable. Still for low frequency, upon increasing disorder, the localisation lengths in the mass disordered system remain within the same order of magnitude. In the spring constant disordered system, we see a more rapid decrease in the localisation lengths until the disorder $\Delta k > 2$, where a sudden drop is observed. Most likely due to the inclusion of negative spring constants. This is evidence that spring constant disorder has a greater effect on the phonon localisation lengths in 1D systems.

Plotting localisation lengths λ as a function of ω^2 for disorders Δm and Δk (in Fig. 4.7), we see the power-law behaviour that is observed in electronic 1D systems [83]. The decrease in localisation length for constant ω^2 goes as $\lambda \sim 1/w^2$, where w represents the disorder strength Δm or Δk [83]. In the vicinity of low (no) DOS near (beyond) the band edge, it is well known [84, 85] that the Lyapunov exponents can grow anomalously. This manifests itself as a smooth decay of the localisation lengths λ that continues beyond the band edge. In the mass disorder

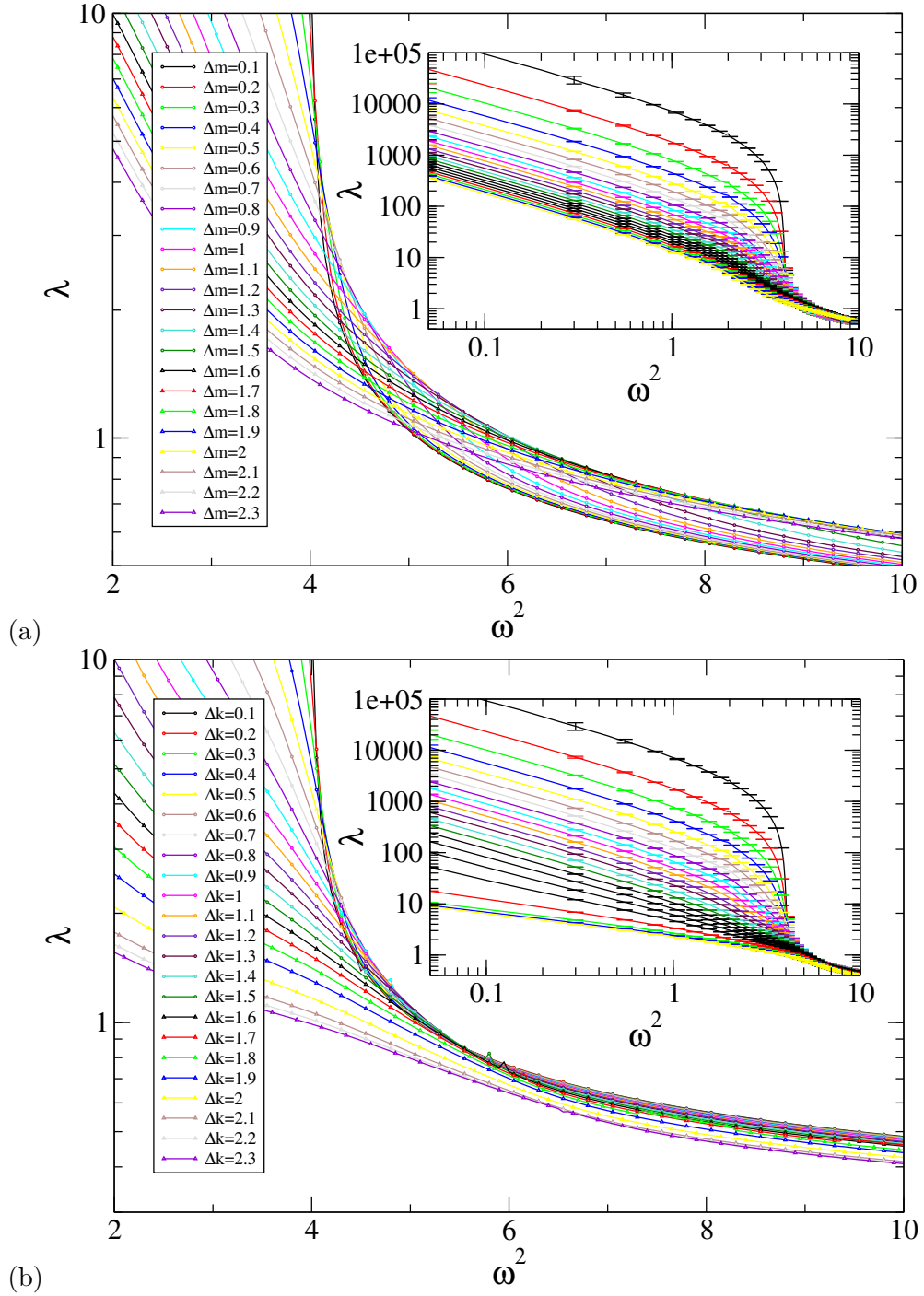


Figure 4.7: Estimations of localisation lengths from the inverse Lyapunov exponents obtained with the TMM plotted as a function of squared frequency ω^2 for a 1D system for a range of (a) uniform box distributed mass disorders and (b) uniform box distributed spring constant disorders. Inset shows full range of ω^2 and main figure is a closeup near the band edges. In both, every fifth symbol is shown.

case, we see that the localisation length dependence on the disorder appears to change from a regime where the localisation length increases for decreasing disorder to a regime where the localisation length decreases for decreasing disorder (see Fig. 4.7(a)). This could be mistaken for a LDT and would not be the first time that this behaviour has been observed in systems of dimensionality $d < 3$ [86, 87]. The authors in these publications attribute the observed behaviour to accuracy of data attainable at time of publication. The behaviour can be explained by comparison to the behaviour of spring constant disordered system in Fig. 4.7(b) and the relative magnitude of the VDOS near the band edge seen in Figs. 4.3(a) and 4.4(a) for mass and spring constant disorder, respectively. In the spring constant disordered case, the position of the band edge increases linearly with disorder strength and the magnitude of the DOS relative to the band edge remains similar for all disorders. The reduction of the localisation lengths near the band edge for all disorder magnitudes is therefore unaffected by DOS and no apparent transition is seen. In comparison, the band edge of the mass disordered system grows as $\omega_{\max}^2 = 4/(1 - \Delta m/2)$ and therefore $\omega_{\max}^2 \rightarrow \infty$ as $\Delta m \rightarrow 2$. The magnitude of the DOS relative to the band edge therefore experiences a continual reduction for increasing Δm with a Lifshitz tail present for disorders $\Delta m \approx 2$. This gives rise to a non-zero DOS for high disorders in a frequency region that was previously forbidden for low disorder. For low disorder near the band edge we have a relatively large DOS with a sudden drop to zero DOS beyond the band edge causing a rapid growth in Lyapunov exponent, and therefore a rapid decrease of localisation length. For increasing disorder the band edge grows rapidly and extends to infinity leaving a persistent Lifshitz tail in the DOS. The finite DOS now present in a frequency range beyond the low disorder band edge causes the localisation length to decrease less rapidly for increasing disorder leading to crossover of localisation lengths for increasing disorder.

Chapter 5

Three Dimensional Normal Modes and Vibrational Density of States

In the present chapter we introduce the canonical equation that governs the displacements from equilibrium of masses in a 3D simple cubic lattice connected with harmonic interatomic interactions (“springs”). We define a simplification that reduces the computational complexity of the 3D system and describe the procedure used to obtain the phonon frequencies and normal modes of vibration. Disorder is introduced into the system by varying either the masses or the spring constants according to uniform box distribution of width Δm or Δk , respectively. We investigate the effect of disorder on the VDOS using both numerical diagonalisation and the coherent potential approximation (CPA).

5.1 Scalar Model of Lattice Dynamics

Similarly to the case for 1D systems (Sec. 4.1) we take the crystal dynamics equation of motion Eqn. (2.7) and apply appropriate constraints to model a simple cubic lattice, i.e. one atom per unit cell and lattice spacing of unit length. Additionally, all displacements of neighbouring sites are given in terms of the current site displacement. This results in a summation over the six nearest neighbours of the current

lattice site, such that

$$\begin{aligned}
-\omega^2 m_{\text{imn}} \begin{bmatrix} u_{1,m,n}^x \\ u_{1,m,n}^y \\ u_{1,m,n}^z \end{bmatrix} &= \begin{bmatrix} k_{l+1,m,n}^{\text{cen}} & 0 & 0 \\ 0 & k_{l+1,m,n}^{\text{non}} & 0 \\ 0 & 0 & k_{l+1,m,n}^{\text{non}} \end{bmatrix} \begin{bmatrix} u_{l+1,m,n}^x - u_{1,m,n}^x \\ u_{l+1,m,n}^y - u_{1,m,n}^y \\ u_{l+1,m,n}^z - u_{1,m,n}^z \end{bmatrix} + \begin{bmatrix} k_{l-1,m,n}^{\text{cen}} & 0 & 0 \\ 0 & k_{l-1,m,n}^{\text{non}} & 0 \\ 0 & 0 & k_{l-1,m,n}^{\text{non}} \end{bmatrix} \begin{bmatrix} u_{l-1,m,n}^x - u_{1,m,n}^x \\ u_{l-1,m,n}^y - u_{1,m,n}^y \\ u_{l-1,m,n}^z - u_{1,m,n}^z \end{bmatrix} \\
&+ \begin{bmatrix} k_{l,m+1,n}^{\text{non}} & 0 & 0 \\ 0 & k_{l,m+1,n}^{\text{cen}} & 0 \\ 0 & 0 & k_{l,m+1,n}^{\text{non}} \end{bmatrix} \begin{bmatrix} u_{l,m+1,n}^x - u_{1,m,n}^x \\ u_{l,m+1,n}^y - u_{1,m,n}^y \\ u_{l,m+1,n}^z - u_{1,m,n}^z \end{bmatrix} + \begin{bmatrix} k_{l,m-1,n}^{\text{non}} & 0 & 0 \\ 0 & k_{l,m-1,n}^{\text{cen}} & 0 \\ 0 & 0 & k_{l,m-1,n}^{\text{non}} \end{bmatrix} \begin{bmatrix} u_{l,m-1,n}^x - u_{1,m,n}^x \\ u_{l,m-1,n}^y - u_{1,m,n}^y \\ u_{l,m-1,n}^z - u_{1,m,n}^z \end{bmatrix} \\
&+ \begin{bmatrix} k_{l,m,n+1}^{\text{non}} & 0 & 0 \\ 0 & k_{l,m,n+1}^{\text{non}} & 0 \\ 0 & 0 & k_{l,m,n+1}^{\text{cen}} \end{bmatrix} \begin{bmatrix} u_{l,m,n+1}^x - u_{1,m,n}^x \\ u_{l,m,n+1}^y - u_{1,m,n}^y \\ u_{l,m,n+1}^z - u_{1,m,n}^z \end{bmatrix} + \begin{bmatrix} k_{l,m,n-1}^{\text{non}} & 0 & 0 \\ 0 & k_{l,m,n-1}^{\text{non}} & 0 \\ 0 & 0 & k_{l,m,n-1}^{\text{cen}} \end{bmatrix} \begin{bmatrix} u_{l,m,n-1}^x - u_{1,m,n}^x \\ u_{l,m,n-1}^y - u_{1,m,n}^y \\ u_{l,m,n-1}^z - u_{1,m,n}^z \end{bmatrix}.
\end{aligned} \tag{5.1}$$

Here ‘l’, ‘m’ and ‘n’ are the site indices in a 3D cartesian co-ordinate system, ω is the frequency, m is the mass and u is the displacement from equilibrium. The subscript of the spring constants k has been shortened so that only the indices of the nearest neighbour site are given as it is known that all springs are connected to the current lattice site (l,m,n). The subscripts ‘l’, ‘m’ and ‘n’ for cartesian directions are roman to distinguish from the mass m . The notation of ‘cen’ and ‘non’ represent the ‘central’ and ‘non-central’ terms of the spring constant tensor matrix, essentially representing the shear and normal spring constant coefficients. In Eqn. (5.1) you can see that the central terms always act along the cartesian direction of the current neighbouring spring, and the non-central terms otherwise.

We simplify this problem by making the assumption that the central and non-central terms are equivalent. This therefore reduces the 3×3 spring constant matrix to that of a scalar quantity and effectively de-couples the system. In this instance only the displacements of the nearest neighbours in a particular cartesian direction contribute to the corresponding component of displacement of the current site. This leaves us with a scalar model of phonons which is also known as the ‘isotropic Born model’ [88–90], given as

$$\begin{aligned}
\left(-\omega^2 m_{l,m,n} + \sum_{\text{NN}} k_{l,m,n} \right) u_{l,m,n} &= k_{l+1,m,n} u_{l+1,m,n} + k_{l-1,m,n} u_{l-1,m,n} \\
&+ k_{l,m+1,n} u_{l,m+1,n} + k_{l,m-1,n} u_{l,m-1,n} + k_{l,m,n+1} u_{l,m,n+1} + k_{l,m,n-1} u_{l,m,n-1},
\end{aligned} \tag{5.2}$$

where the summation is over all spring constants that directly connect the current site to the nearest neighbours (NN). Now the three cartesian co-ordinates are de-coupled and the spring constant is a scalar value. Solving the system for a single spatial dimension using Eqn. (5.2) essentially solves the total displacement of all sites in 3D as the problem is replicated in all dimensions. This means that all the rich information obtained for vector vibrations with a (nine times) larger dynamical

matrix is preserved.

The system of lattice sites where each obeys Eqn. (5.2) is arranged into an appropriate dynamical matrix and diagonalised to obtain the normal mode frequencies and corresponding vibrational displacements. The obtained displacements for a single spatial dimension are exactly equal to the total amplitudes in the vector case. The obtained vibrational displacement is replicated in all other dimensions and are combined using Pythagoras theorem. There is therefore a pre-multiplicative factor of $\sqrt{3}$ for the amplitude vector, that is normalised to unity such that the sum of the squares of the amplitudes is unity.

5.1.1 Maximum and Minimum Frequencies

Starting as above with Eqn. (2.7) we this time substitute the plane wave Eqn. (4.2) so that all amplitude terms are eliminated from the dynamical equation. We arrive at the form

$$-\omega^2 m = k(e^{iq_n a} + e^{-iq_n a} + e^{iq_m a} + e^{-iq_m a} + e^{iq_1 a} + e^{-iq_1 a} - 6), \quad (5.3)$$

where the scalar wavevectors q_1 , q_m and q_n make up the wavevector \mathbf{q} . Furthermore, the ‘-6’ term is known as the coordination number and is a direct consequence of the simple cubic lattice structure and every lattice site having 6 neighbours. Let us assume that all masses and spring constants are identical throughout the system. We use a series of trigonometric identities to arrive at

$$-\omega^2 M = 2k [\cos(q_n a) + \cos(q_m a) + \cos(q_1 a) - 3] \quad (5.4)$$

$$\omega^2 M = 4k \left[\sin^2 \left(\frac{q_n a}{2} \right) + \sin^2 \left(\frac{q_m a}{2} \right) + \sin^2 \left(\frac{q_1 a}{2} \right) \right] \quad (5.5)$$

Taking the limits of the trigonometric functions where the wave vector minima are zero and maxima are $q_n = q_m = q_1 = \frac{\pi}{a}$ leaves the relationships

$$\omega_{\max}^2 = \frac{12k}{m}, \quad \omega_{\min}^2 = 0. \quad (5.6)$$

Here the subscripts ‘max’ and ‘min’ relate to the limits used to obtain the relationships and not to the frequencies they represent. Both equations represent band edges that can be either upper or lower, this becomes clearer with the inclusion of disorder. Given this, we introduce the disorder, such that $m \Rightarrow \langle m \rangle \pm \frac{\Delta m}{2}$ and $k \Rightarrow \langle k \rangle \pm \frac{\Delta k}{2}$. When Δk or $\Delta m > 2$, ω_{\max}^2 can be used to obtain negative band edges and therefore the lower band edge can extend below zero, into the negative

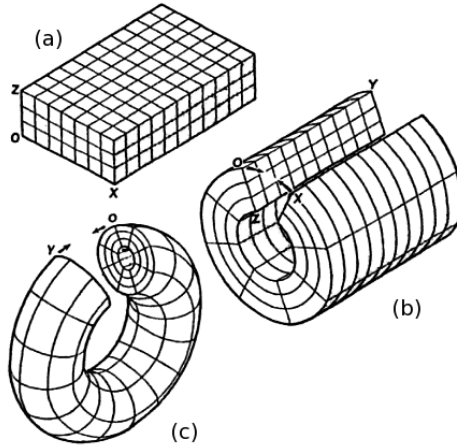


Figure 5.1: Diagram to demonstrate the inability to physically apply theoretical Born and Von Kármán periodic boundary conditions in a 3D cubic lattice. We see the transition from (a) to (b) by joining a single dimension to produce a hollow cylinder. The transition from (b) to (c) to join a second spatial dimension produces a torus, from which the third spatial dimension cannot be joined. Taken from Ref. [92].

ω^2 regime.

5.2 Normal Modes

Now that a canonical equation is defined we decide on using periodic boundary conditions that were first proposed by Born and Von Kármán [91]. Unlike the situation in one-dimension where the periodic chain can be visualised as a ring, a 3D visualisation of a periodic cube cannot exist in nature as displayed pictorially in Fig. 5.1. The initial stage shows the cubic lattice being bent into a cylinder and then joined at either end into a torus, after which further deformations cannot satisfy the final dimension's boundary conditions. Although the conditions cannot be realised physically we still use periodic boundary conditions in an attempt to simulate an infinite lattice, this way fixed boundary effects are non-existent and as the system size increases the amplitudes become less dependent on the periodic nature of the box.

We start our investigation of the system by visualising some typical eigenstates. We use sparse matrix diagonalisation of the dynamical matrix outlined in Chap. 3 to obtain eigenstates of a reasonably large size $L^3 = 70^3$. In Figs. 5.2 and 5.3, we show eigenstates for the pure mass and pure spring constant disordered

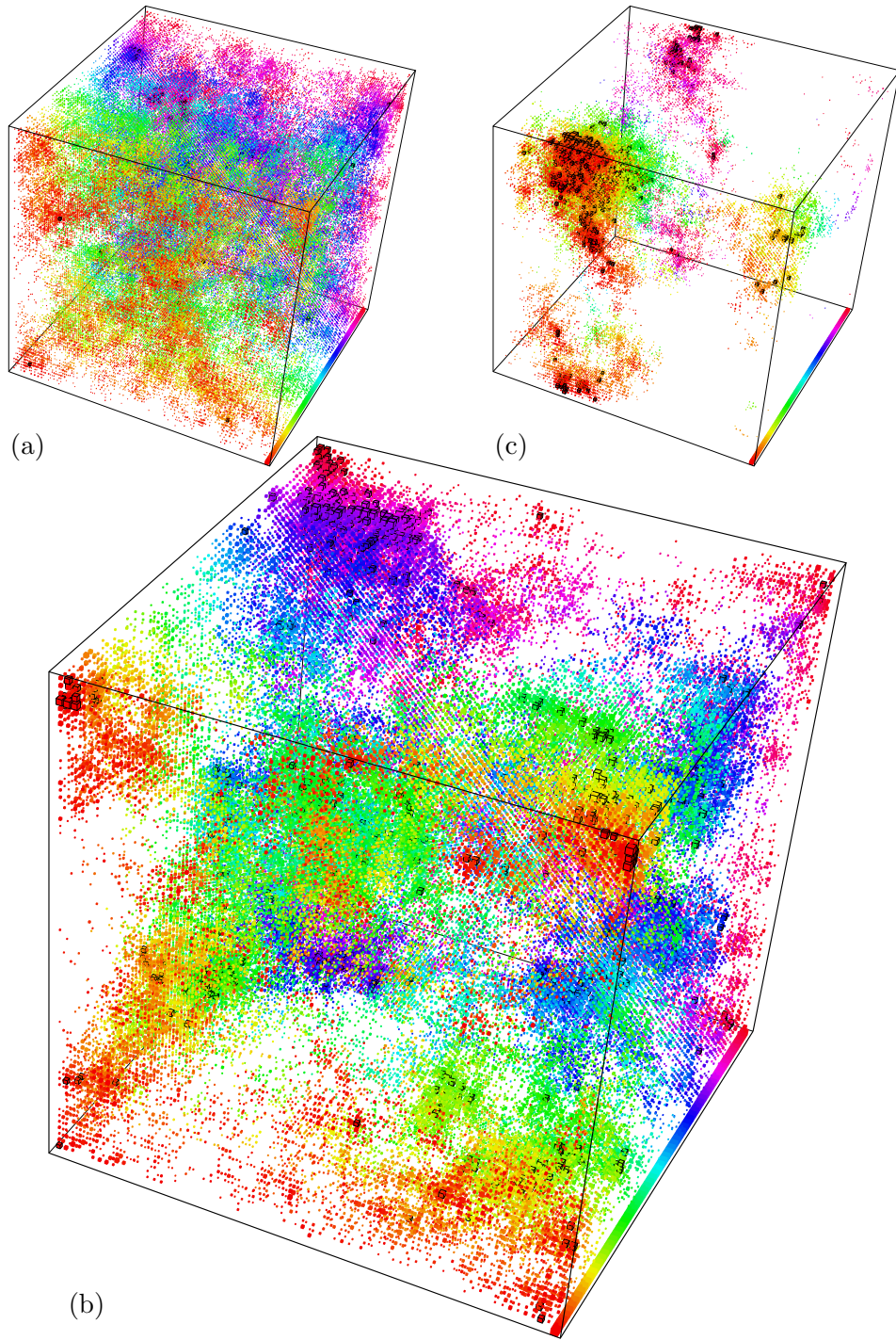


Figure 5.2: Normal modes in a box of size $L^3 = 70^3$ lattice sites with periodic boundary conditions and uniform box distributed disorder applied to the masses with width $\Delta m = 1.5$ and squared frequency (a) $\omega^2 = 9$, (b) $\omega^2 = 11$ and (c) $\omega^2 = 12.5$. The colours vary according to the depth within the box as shown on the scale in the base of the boxes. All sites with $u(\vec{r}_j)/L^3 \sum_j u(\vec{r}_j) > 1$ are shown as small cubes and those with black edges have $u(\vec{r}_j)/L^3 \sum_j u(\vec{r}_j) > \sqrt{1000}$ and $|u_j| < \langle |u_j| \rangle$ are not displayed.

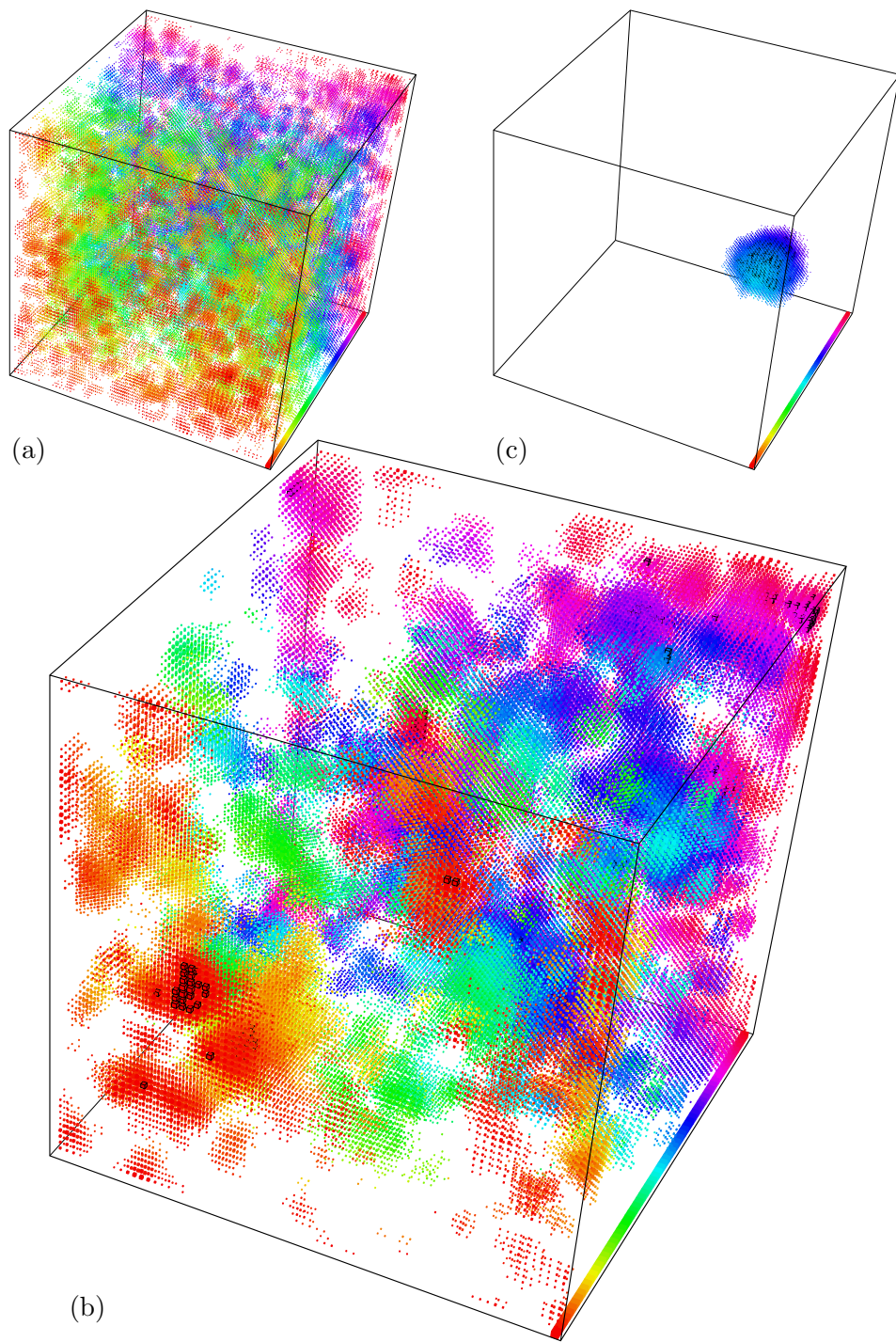


Figure 5.3: Eigenstates for uniform box distributed disorder applied to the spring constants with width $\Delta k = 1$ and squared frequency (a) $\omega^2 = 12$, (b) $\omega^2 = 12.5$ and (c) $\omega^2 = 13.03$. All other parameters are as in Fig. 5.2.

cases, respectively, corresponding to three eigenfrequencies which lie in regions that appear to be extended, close to the mobility edge and localised. For Figs. 5.2 and 5.3(a), the local amplitude of vibrations at each site is roughly of similar magnitude throughout the system, whereas for Figs. 5.2 and 5.3(c), the vibrations are confined to a small region in the cube. Figs. 5.2 and 5.3(b) display the characteristic properties of a *critical* phonon state at the Anderson mobility edge [93]. As we will show in Chap. 6, these classification indeed agree with the computed phase diagrams for the pure mass and pure spring constant disordered cases. However, we also see that the character of the spring constant states seem subtly different from the pure mass disorder ones. The vibrations seem to be more around certain vibration centres and radiate outward roughly symmetrically from these centres [94]. We emphasise that this should make the multifractal analysis of such states very informative, in particular its comparison with the recently proposed symmetry of the multifractal spectrum [79, 93, 95] as we will see in Chap. 8.

5.3 Numerical Vibrational Density of States

In order to numerically obtain the VDOS, the computation of *all* states is required. We therefore use the dense matrix diagonalisation methods outlined in Chap. 3. This is computationally more expensive and reduces the maximum system size achievable. We calculate the VDOS $g(\omega^2)$ for disorders Δm , $\Delta k = 0.5, 1, 1.2, 1.5, 2, 2.5, 3, 4, \dots, 9$ and 10 for cubes with width $L = 5, 10$ and 15 with 1360, 170 and 50 disorder configurations, respectively. This results in 170,000, 170,000 and 168,750 normal modes, respectively, for each disorder/system size combination. The plots of $g(\omega^2)$ as a function of ω^2 are shown in Fig. 5.4 for all above mass and spring constant disorder magnitudes. A typical feature of the VDOS are the Van Hove singularities [96]. As the disorder is increased they broaden and smear out, and the lowest Van Hove singularity smoothly shifts toward $\omega^2 = 0$.

In the pure mass disorder case there is the development of sharp, well-defined peaks in *both* the positive and complex frequency spectrum, with the peak in the positive part always being larger. Both peaks have rather long tails due to the removal of upper and lower frequency limits beyond $\Delta m = 2$ as discussed in Sec. 5.1.1. For pure spring disorder we observe a peak for $\Delta k < 2$ whereas when $\Delta k > 2$ (unstable regime) the inclusion of negative spring constants causes a piling up of states around $\omega = 0$ that is further amplified in the reduced VDOS $g(\omega)/\omega^2$ shown in Fig. 5.5(b). For both mass and spring constant disorder in the low disorder regime there is the usual low frequency fluctuations due to the global translational

invariance.

5.4 The Coherent Potential Approximation

We use the CPA to verify the VDOS results obtained via numerical diagonalisation for disorders that have, to the authors knowledge, not been previously studied. The CPA is one of the most established Green's function methods. It is useful when considering waves in a random medium. Due to the loss of translational symmetry (a consequence of disorder), accurate solutions to the wave equation are generally not possible. Therefore, in some cases, even if the exact Green's function is known, it is not always possible to extract the desired information [97]. In CPA we perform a configurational average of the Green's function for many realisations of the applied disorder. This produces a much simpler function that is easier to calculate and extract information from.

We recall the operator notation [98] for the Green's function as $\mathbf{G} = \mathbf{G}_{\text{eff}} + \mathbf{G}_{\text{eff}}\mathbf{V}\mathbf{G}$, where \mathbf{V} is the impurity potential operator. Another way to express this is by iterating on \mathbf{G} to give

$$\begin{aligned}\mathbf{G} &= \mathbf{G}_{\text{eff}} + \mathbf{G}_{\text{eff}}\mathbf{V}[\mathbf{G}_{\text{eff}} + \mathbf{G}_{\text{eff}}\mathbf{V}(\mathbf{G}_{\text{eff}} + \mathbf{G}_{\text{eff}}\mathbf{V}\dots \\ &= \mathbf{G}_{\text{eff}} + \mathbf{G}_{\text{eff}}\mathbf{V}\mathbf{G}_{\text{eff}} + \mathbf{G}_{\text{eff}}\mathbf{V}\mathbf{G}_{\text{eff}}\mathbf{V}\mathbf{G}_{\text{eff}} + \dots\end{aligned}$$

or alternatively

$$\mathbf{G} = \mathbf{G}_{\text{eff}} + \mathbf{G}_{\text{eff}}\mathbf{T}\mathbf{G}_{\text{eff}} \quad (5.7)$$

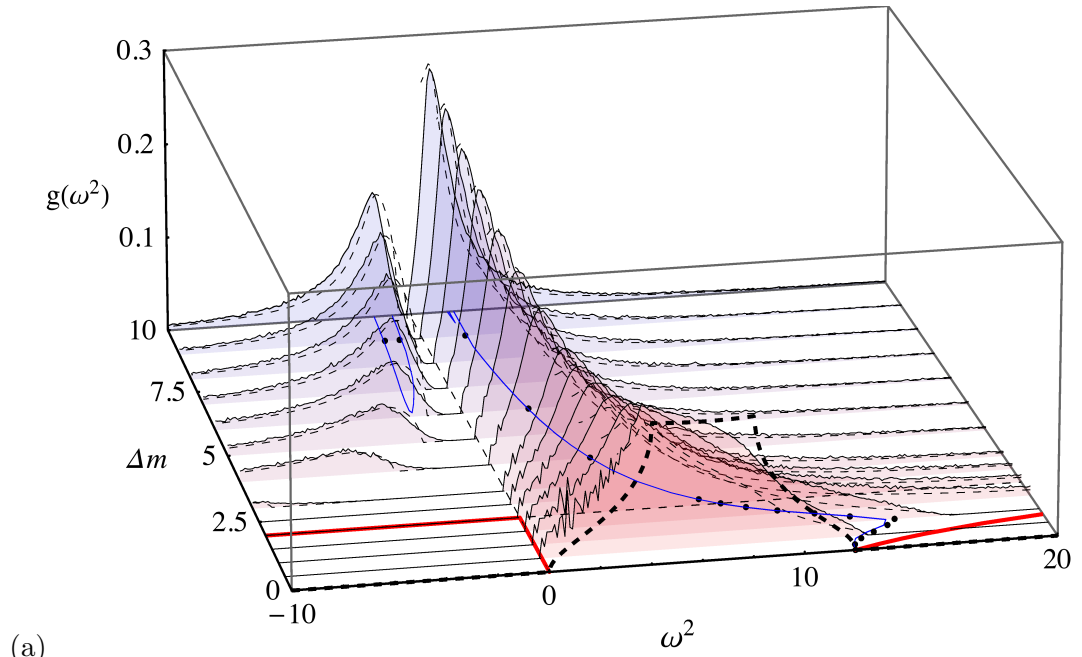
where

$$\begin{aligned}\mathbf{T} &= \mathbf{V} + \mathbf{V}\mathbf{G}_{\text{eff}}\mathbf{V} + \mathbf{V}\mathbf{G}_{\text{eff}}\mathbf{V}\mathbf{G}_{\text{eff}}\mathbf{V} + \dots \\ &= \mathbf{V}(\mathbf{1} + \mathbf{G}_{\text{eff}}\mathbf{V})^{-1} = (\mathbf{1} + \mathbf{V}\mathbf{G}_{\text{eff}})^{-1}\mathbf{V}\end{aligned} \quad (5.8)$$

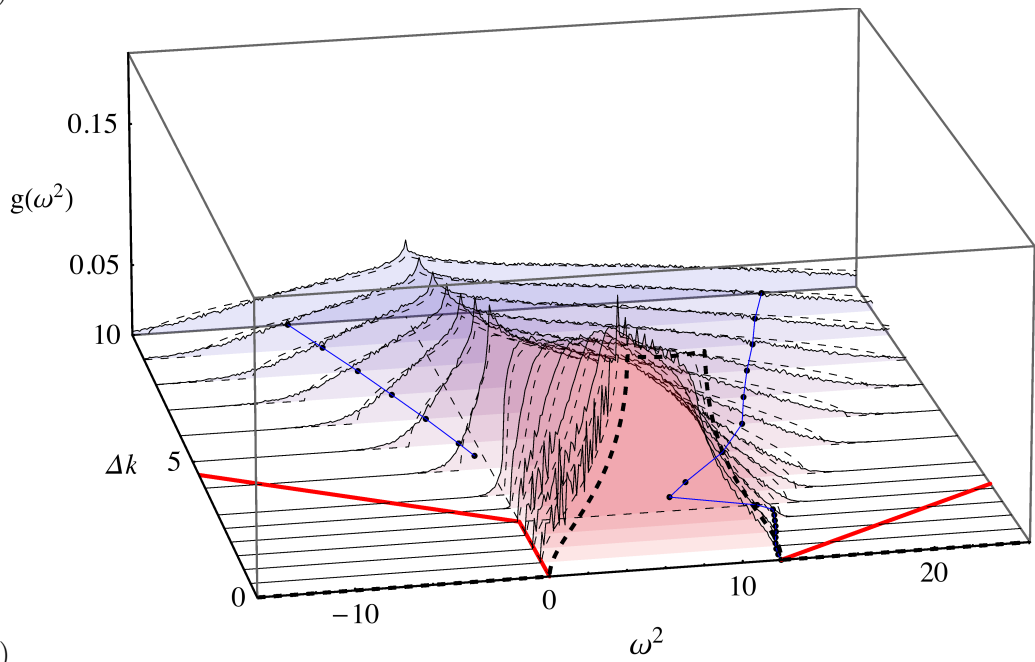
and \mathbf{T} is known as the scattering or \mathbf{T} -matrix. It is recognised that if the impurity potential represents a single scattering (perturbation to the effective medium), the scattering matrix includes the multiple scatterings.

5.4.1 Mass Disorder

It is well known [99–102] that the mass disordered scalar vibrational model is analogous to the potential disordered electronic problem. A pair of transformation equations are derived later in this work (Sec. 6.1). Due to the loss of symmetry in



(a)



(b)

Figure 5.4: VDOS $g(\omega^2)$ as a function of squared frequency ω^2 and disorders Δm and Δk . The coloured planes are the numerical diagonalisation results and the thin dashed lines are obtained from CPA. The blue and red lines in the base denote the trajectories of the LDT and the band edges respectively as in Fig. 6.12. The thick dashed line is the CPA VDOS free from disorder with Van Hove singularities as expected at $\omega^2 = 4$ and 8 .

the dynamical matrix with the inclusion of mass disorder in the system, the single site CPA is difficult to implement. We therefore study the potential disordered electronic problem and apply the known single site CPA equations to find the average VDOS. Then we transform the obtained electronic DOS to that of the mass disordered phonon system. The electronic tight binding Hamiltonian for this problem is

$$\hat{H} = \sum_i |i\rangle \epsilon_i \langle i| + t \sum_j |j\rangle \langle i|, \quad (5.9)$$

where the ϵ_i 's are uncorrelated random potentials that follow a box distribution such that $\epsilon_i \in [-\frac{\mathcal{W}}{2}, \frac{\mathcal{W}}{2}]$. This distribution directly translates to a mass disordered distribution in the phonon case such that $m_i \in [\langle m \rangle - \frac{\Delta m}{2}, \langle m \rangle + \frac{\Delta m}{2}]$ using the conversion equations $\mathcal{W} = \omega^2 \Delta m$ and $\epsilon_i = \omega^2 (m_i - \langle m \rangle)$ taken from Sec. 6.1. Here \mathcal{W} and Δm are the distribution widths for the electronic potential disordered and the phonon mass disordered problems, respectively. The hopping integral t is taken to be one.

The first stage of the CPA is to replace the disorder parameter ϵ_i by an unknown common value Σ . Σ is known as the self energy and can be energy dependant and complex. We denote the energy dependance as $\Sigma(z)$ where z is the complex energy with a negligible imaginary part ($z = \epsilon_i + i0^+$). The replacement changes the Hamiltonian (5.9) to that of a periodic effective Hamiltonian

$$\hat{H}_{\text{eff}}(z) = \sum_i |i\rangle \Sigma(z) \langle i| + t \sum_j |j\rangle \langle i|. \quad (5.10)$$

We now replace a single effective site energy, say at i_0 , by some fluctuating energy ϵ_i . This applies a perturbation to \hat{H}_{eff} and defines a perturbed Hamiltonian as

$$\hat{H}_{\text{per}} = \hat{H}_{\text{eff}} + \underbrace{|i_0\rangle (\epsilon_{i_0} - \Sigma) \langle i_0|}_{\mathcal{V}_{i_0}}. \quad (5.11)$$

Now following Eqns. (5.7) and (5.8), the configurationally averaged Green's function and single site \mathbf{T} -matrix are given as

$$\langle \mathbf{G} \rangle = \mathbf{G}_{\text{eff}} + \mathbf{G}_{\text{eff}} \langle \mathbf{T} \rangle \mathbf{G}_{\text{eff}}, \quad (5.12)$$

$$\langle \mathbf{T} \rangle = \langle \mathbf{V} (\mathbf{1} - \mathbf{G}_{\text{eff}} \mathbf{V})^{-1} \rangle, \quad (5.13)$$

respectively. For the configurationally averaged Green's function to be equal to that of the effective, we restrict our calculation so that the \mathbf{T} -matrix in Eqn. (5.13) is on average equal to zero. We also note that the \mathbf{T} -matrix is diagonal ($\langle i_0 | \mathbf{T} | i_0 \rangle \equiv t_{i_0}$),

and to satisfy this condition, the average of the individual single site scatterers must also be zero ($\langle t_{i_0} \rangle = 0$).

We re-write our configurationally averaged T -matrix Eqn. (5.13) in terms of single sites, where we include the perturbation from Eqn. (5.11) as the single site impurity potential to give

$$\langle t_{i_0} \rangle = \left\langle \frac{\mathcal{V}_{i_0}}{1 - \mathcal{V}_{i_0} \underbrace{\langle i_0 | \mathbf{G}_{\text{eff}} | i_0 \rangle}_{G_{\text{eff}}(z) = G_0[z - \Sigma(z)]}} \right\rangle = \left\langle \frac{\epsilon_{i_0} - \Sigma(z)}{1 - [\epsilon_{i_0} - \Sigma(z)] G_0[z - \Sigma(z)]} \right\rangle = 0. \quad (5.14)$$

The configurational average can be evaluated by an integral over the disorder distribution as

$$\langle t_i \rangle = \int d\epsilon_i p(\epsilon_i) t_i = 0. \quad (5.15)$$

The average DOS is then calculated from the Green's function as

$$\langle \rho(\epsilon) \rangle = -\frac{1}{\pi} \Im \{ G_0[z - \Sigma(z)] \}. \quad (5.16)$$

Evaluating The Lattice Green's Function

When evaluating the averaged single site scattering term, Eqn. (5.14), there are two unknowns; the self energy $\Sigma(z)$ which must be determined self consistently and the lattice Green's function G_0 . We have a simple cubic lattice and the corresponding simple cubic Green's function is of the form

$$G_{\text{sc}}(z; l, m, n) = \frac{1}{\pi^3} \int_0^\pi dx \int_0^\pi dy \int_0^\pi dz \frac{\cos lx \cos my \cos nz}{z - \cos x - \cos y - \cos z}. \quad (5.17)$$

Here the imaginary part of $G_{\text{sc}}(z; 0, 0, 0) \equiv G_0(z)$ gives the negative of the DOS [103]. Numerically integrating over the Brillouin zone can be difficult. We therefore follow the work of Joyce [104], who showed that the Green's function can be expressed as the square of a Heun function [104]¹. Joyce later derived an exact representation for the Green's function as the product of two complete elliptic integrals of the first kind. It follows that

$$G(z) = z^{-1} P(t)_{sc}, \quad (t = \frac{3}{z}), \quad (5.18)$$

$$P(t)_{sc} = (1 - \frac{3}{4}x_1)^{\frac{1}{2}} (1 - x_1)^{-1} (\frac{2}{\pi})^2 \mathbf{K}(k_+) \mathbf{K}(k_-), \quad (5.19)$$

$$k_\pm^2 = \frac{1}{2} \pm \frac{1}{4}x_2(4 - x_2)^{\frac{1}{2}} - \frac{1}{4}(2 - x_2)(1 - x_2)^{\frac{1}{2}}, \quad (5.20)$$

¹See Ref. [105] for the original German paper on Heun functions.

$$x_1 = \frac{1}{2} + \frac{1}{6}t^2 - \frac{1}{2}(1-t^2)^{\frac{1}{2}}(1-\frac{1}{9}t^2)^{\frac{1}{2}}, \quad (5.21)$$

$$x_2 = \frac{x_1}{(x_1-1)}, \quad (5.22)$$

where \mathbf{K} represents a complete elliptic integral of the first kind, which has a standard numerical solution [106].

Self Consistency

As mentioned above we determine the self energy self consistently. To do this we use the following iteration method that is equivalent to the CPA condition [107]

$$\Sigma(z)^{(n+1)} = \Sigma(z)^{(n)} + \frac{\langle t \rangle^{(n)}}{1 + \langle t \rangle^{(n)} G_0(z - \Sigma(z)^{(n)})}, \quad (5.23)$$

$$\langle t \rangle^{(n)} = \left\langle \frac{\epsilon_{i_0} - \Sigma(z)^{(n)}}{1 - (\epsilon_{i_0} - \Sigma(z)^{(n)}) G_0(z - \Sigma(z)^{(n)})} \right\rangle. \quad (5.24)$$

The computation requires an adequate starting value for $\Sigma(z)^{(0)}$. This is approximated using its lowest-order expansion [108]

$$\Sigma(z)^{(0)} \approx \frac{\mathcal{W}}{12} G_0(z). \quad (5.25)$$

Density of States Conversion

We cannot assume that the DOS from the electronic case is the same as the DOS in the phonon case. So far only a transformation of independent variable ($E \rightarrow \omega^2$) has been implemented. We know that the DOS ($g_e(\mathcal{W}, E)$) in the electronic case is dependent on both the disorder width \mathcal{W} and energy E and similarly the phonon VDOS $g_p(\Delta m, \omega^2)$ is dependant on Δm and ω^2 . As in both cases the DOS is dependant on two variables, a conversion between co-ordinate systems requires a Jacobian. The equations that relate the variables of the electronic and phonon systems are necessary to compute the Jacobian and were previously derived in Sec. 6.1. They are given as $E = 6 - \omega^2$ and $\mathcal{W} = \Delta m |\omega^2|$. The Jacobian is therefore

$$\mathcal{J} = \begin{vmatrix} \frac{\partial \omega^2}{\partial E} & \frac{\partial \omega^2}{\partial \mathcal{W}} \\ \frac{\partial(\Delta m)}{\partial E} & \frac{\partial(\Delta m)}{\partial \mathcal{W}} \end{vmatrix} = \begin{vmatrix} -1 & 0 \\ 0 & \frac{1}{\omega^2} \end{vmatrix} \quad (5.26)$$

and the determinant of the Jacobian is $-\frac{1}{\omega^2}$. This gives us the relation

$$\int_{\mathcal{W}} \int_E \frac{1}{\omega^2} g_e(\mathcal{W}, E) dE d\mathcal{W} = \int_{\Delta m} \int_{\omega^2} g_p(\Delta m, \omega^2) d\omega^2 d\Delta m. \quad (5.27)$$

Here the \mathcal{W} and Δm disorder distributions for the electronic and phonon case, respectively, are already normalised. We therefore expect the DOS for a given disorder magnitude to be transformed using the equation

$$\int_E \frac{1}{\omega^2} g_e(E) dE = \int_{\omega^2} g_p(\omega^2) d\omega^2 = 1. \quad (5.28)$$

5.4.2 Spring Constant Disorder

In the spring constant disorder case we are fortunate that the system follows a Laplacian form and that the two-site CPA approximation can be used [72, 109]. We consider a system where each site is occupied by a mass of fixed value \bar{m} . It is convenient here to use a notation that signifies the connection between adjacent sites and therefore use 3D site indices (e.g. i, j and l) that each consist of three cartesian site indices, previously referred to as ‘l’, ‘m’ and ‘n’. Each site is connected to six nearest neighbours by a spring of force constant k_{ij} that fluctuates according to a box distribution of width Δk , such that $k_{ij} \in [\langle k \rangle - \frac{\Delta k}{2}, \langle k \rangle + \frac{\Delta k}{2}]$. The time-dependent equation of motion for this system is

$$\frac{d^2}{dt^2} u_i(t) = - \sum_j k_{ij} (u_i(t) - u_j(t)) \quad (5.29)$$

and therefore the corresponding Green’s function of this equation follows

$$\frac{d^2}{dt^2} \mathcal{G}_{ij}(t, t') + \sum_l k_{il} (\mathcal{G}_{ij} - \mathcal{G}_{lj}) = \delta_{ij} \delta(t - t'). \quad (5.30)$$

Now, we define the dynamical matrix as

$$\mathcal{H}_{ij} = \begin{cases} -\sum_l k_{il} & i = j \\ k_{ij} & i \neq j \end{cases}, \quad (5.31)$$

and by Fourier transforming we obtain the Green’s matrix $\langle i | \mathcal{G}(\omega^2) | j \rangle = \mathcal{G}_{ij}(\omega^2)$ via

$$(z - \mathcal{H}) \mathcal{G} = (-\omega^2 + i\epsilon - \mathcal{H}) \mathcal{G} = 1, \quad (5.32)$$

where, as before, z is the complex frequency with minimal complex part.

We create the ‘effective medium’ by replacing the disordered spring constants with some effective frequency dependent spring constants ($\Gamma(z)$). Therefore, the dynamical matrix becomes

$$\mathcal{H}_{ij} = \begin{cases} -\sum_l k_{il}^{\text{eff}} = 6\Gamma(z) & i = j \\ k_{ij}^{\text{eff}} = \Gamma(z) & i \neq j \end{cases}, \quad (5.33)$$

where the sum over nearest neighbours in a simple cubic lattice is a summation of six effective spring constants, hence the term $6\Gamma(z)$. This in turn redefines the Green’s function of the effective medium as

$$z\mathcal{G}_{ij} - \delta_{ij} = 6\Gamma(z)(\mathcal{G}_{lj} - \mathcal{G}_{ij}). \quad (5.34)$$

Where the subscript l is the site index for some arbitrary neighbouring site. Similar to the electronic case where we replace a single site i_0 with an actual random potential, here we also include an actual random spring constant. We are considering the two-site CPA and therefore replace the effective spring constant between a single pair of sites with an actual random spring constant $k_{i_0j_0}$. This acts as our perturbation $v_{i_0j_0}(z) = k_{i_0j_0} - \Gamma(z)$ and the perturbation matrix is populated as

$$V = \begin{pmatrix} -v_{i_0j_0}(z) & v_{i_0j_0}(z) \\ v_{i_0j_0}(z) & -v_{i_0j_0}(z) \end{pmatrix}. \quad (5.35)$$

Again the key factor to this theory is that the inclusion of the perturbation should have no effect on averaged \mathbf{T} -matrix (Eqn. (5.13)) being zero. Taking the inverse of the perturbation matrix and using $i = j$ in Eqn. (5.34) we arrive at the \mathbf{T} -matrix

$$\langle T \rangle = \left\langle \frac{k - \Gamma(z)}{1 + [k - \Gamma(z)] \frac{2}{6\Gamma(z)} [1 - zG(z)]} \right\rangle = 0. \quad (5.36)$$

The T-matrix can be reformulated in terms of Γ in order to solve for $\langle \mathbf{T} \rangle$ self consistently. The local Green’s function G is given as a function of the simple cubic lattice Green’s function G_0 .

$$\Gamma(z) = \left\langle \frac{k}{1 + [k - \Gamma(z)] \frac{2}{6\Gamma(z)} [1 - zG(z)]} \right\rangle, \quad (5.37)$$

$$G = \frac{1}{\Gamma(z)} G_0 \left(\frac{z}{\Gamma(z)} \right), \quad (5.38)$$

where the lattice Green’s function and DOS are found as in the mass disorder case

using Eqn. (5.16).

We plot in Fig. 5.4 the VDOS results obtained from CPA calculations with the numerical diagonalisation VDOS and find a very good agreement between both approaches. Low frequency mass disorder CPA results are not plotted due to the dependance of the Jacobian on the reciprocal of the variable ω^2 . This causes the CPA DOS to diverge to infinity for $\omega^2 \rightarrow 0$.

5.5 The Boson Peak

The excess contribution to the VDOS at low temperatures was named the “Boson Peak” (BP) by Josef Jäckle [110] after low-frequency Raman scattering experiments on glasses in 1981 revealed an anomalous peak. As early as 1959, Flubacher et al. [111] inferred the existence of extra vibrational modes in vitreous silica to explain the excess heat capacity at low temperatures (3 - 15K) over the Debye modes. Since these discoveries it has also been noted that the BP is present in crystalline systems with the inclusion of disorder. In perfect crystalline systems, the VDOS exhibits Van Hove singularities [96], the positions of which are dictated by the underlying lattice. With enough disorder the singularities broaden and smear eventually being recognised as a BP. There is a smooth transition from the lowest Van Hove singularity to what is considered a BP leading to intense debate regarding the origins and significance of the peak. It is unclear at what level of disorder the underlying lattice no longer contributes to the shape of the VDOS [112, 113]. On one hand (even in amorphous systems) the BP is simply considered a renormalised analogue to the crystalline Van Hove singularities [114, 115] and has no further significance. On the other hand the BP is conjectured to mark the cross-over of vibrational states between Debye-like waves and random-matrix type eigenstates [72]. It has been shown that a BP is present in field theoretical theories that neglect the presence of an underlying lattice [116, 117], supporting the latter.

It is often stated that the origins of the peak are unknown, implying that nothing is known about the modes within the peak [73, 118]. The form of the peak is found to be largely independent of the material type. This suggests that the underlying origin may be quite fundamental to the physics of scattering in disordered systems [113] and could mark the onset of some transition or crossover of transport regimes. Past studies claimed that the frequency of the BP is the onset of the LDT [119]. Later investigations of the localisation properties of disordered vibrational modes agree that the modes with frequencies greater than the BP frequency

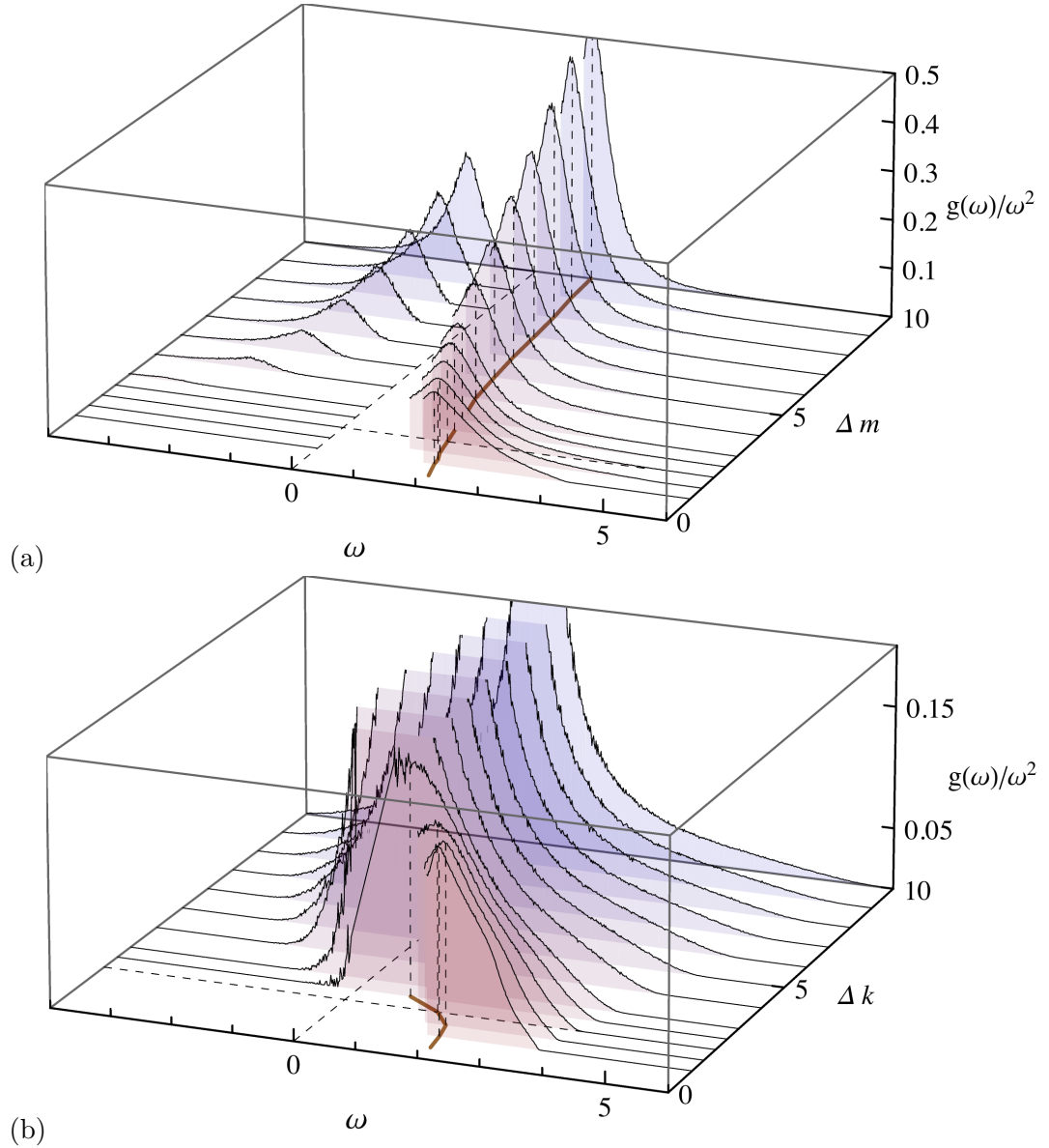


Figure 5.5: Reduced VDOS $g(\omega)/\omega^2$ as a function of frequency ω and a range of (a) mass Δm and (b) spring constant Δk disorders. The green line in the base denotes the trajectory of the BP. The negative ω axis represents the complex ω range. Noisy data as $\omega \rightarrow 0$ due to the division by ω^2 has been arbitrarily truncated below the BP for clarity.

are extended² [72, 120, 121]. Since then, there have been attempts to analytically relate the ω_c and ω_{BP} [122], though it is now argued that no such relationship exists [123–125]. Another transition considered to occur near the BP frequency is the phonon-fracton crossover [126], although numerical calculations [126] and experimental Raman studies [127] have shown that this is also not correct. Later it was conjectured that the BP is in fact the point that separates a nearly plane wave regime from a regime where disorder is dominant (random-matrix regime) [72]. Recently it has been shown that the Ioffe-Regel criterion between weak and strong scattering regimes occurs, at a qualitative level, at the BP frequency [113, 128]. We see in the low frequency regime of the VDOS some fluctuations that indicate the existence of plane waves below the BP frequency. It has been argued via eigenvalue statistics that the states with $\omega_{\text{BP}} < \omega < \omega_c$ are governed by random-matrix statistics of the Gaussian orthogonal ensemble (GOE) [72, 129], supporting this conjecture. In this work we locate the trajectory of the BP and study the normal modes from frequency domains both below and above the BP frequency ω_{BP}^2 , for two disorders in each disorder type. By doing so we attempt to find some effects of the BP on the normal modes.

If we assume that the VDOS $g(\omega)$ follows the Debye $g(\omega) \propto \omega^2$ law [72, 122], and divide by ω^2 , the reduced VDOS $g(\omega)/\omega^2$ should be flat. We plot the reduced VDOS $g(\omega)/\omega^2$ obtained from numerical diagonalisation in Fig. 5.5 and find that for most disorder magnitudes there is a well defined peak in the low frequency regime. For the sake of consistency we consider all peaks in the reduced VDOS as a true BP and they occur at frequency ω_{BP} . The peak locations ω_{BP}^2 from the numerical diagonalisation and the CPA calculations are plotted as a function of disorder width in Fig. 5.6. For the peak obtained by numerical diagonalisation the error is estimated from the width of the peak at 95% of the original height. The BP frequencies ω_{BP}^2 obtained from the CPA are within error of the peak obtained from numerical diagonalisation. In the mass disordered case the peak is persistent for all disorder magnitudes. In the spring constant disorder case the peak reaches $\omega^2 = 0$ at a disorder of $\Delta k \simeq 3$ and remains there contributing to the other well known feature of the spring constant disordered VDOS, the zero frequency singularity [130]. The different trajectories of the BPs for mass and spring constant disorders gives the possibility of studying normal modes for constant frequencies and disorder magnitudes whilst the positions of said modes fall on differing sides of the BP trajectories. In Fig. 5.6(a), for mass disorder, labels ①-④ corresponds to the eigenstates plotted

²We'll see in this study (Chap. 6) that for all magnitudes of disorder $\omega_{\text{BP}} \ll \omega_c$, where ω_c is the boundary between extended and localised states.

in Fig. 5.7(a)-(d), where (a) and (c) are at constant frequency $\omega^2 = 1 < \omega_{\text{BP}}^2$. In Fig. 5.6(b), for spring constant disorder, labels (a)-(d) corresponds to the eigenstates plotted in Fig. 5.8(a)-(d), where (a) and (c) are at constant frequency $\omega^2 = 1$. For disorder $\Delta k = 1$, $\omega^2 < \omega_{\text{BP}}^2$ and for $\Delta k = 4$, $\omega^2 > \omega_{\text{BP}}^2$.

Careful study of the states in Figs. 5.7(a)-(d) and 5.8(a)-(d) indicates that the BP frequency qualitatively separates two different phonon transport regimes. In the mass disorder scenario (Fig. 5.7) we find that both states (a) and (c) at frequency $\omega^2 = 1$ barely differ in their makeup regardless of the difference in disorder applied and both are at a frequency $\omega^2 < \omega_{\text{BP}}^2$. Both (a) and (c) appear as a periodic arrangement of “cotton balls”, which indicates plane waves. States (b) and (d) cannot be compared as (b) is near or beyond the LDT whilst (d) is in the extended regime with a higher excitation frequency than (c). Now comparing states (a) and (c) in Fig. 5.8 for spring constant disorder, we instantly see a different scenario. Although we have the “cotton ball” effect at low frequency and low disorder in (c), beyond the BP boundary for increased disorder at $\omega^2 = 1$ in (a), we find that the eigenstate differs drastically. The disorder has altered the makeup of the vibrational state. Continuing in the extended regime for both disorder $\Delta k = 1$ and 4 in states (d) and (b), respectively, we find that both are most likely in the extended regime and differ very little.

We note that the above result, without the presence of a transition near the BP, would be counter intuitive. If we study the LDT phase diagrams in Sec. 6.4, for mass disorder, we have an increasingly smaller proportion of extended states as disorder increases. Whereas we see the opposite behaviour for spring constant disorder, where the phase boundary continues to extend towards higher frequencies as disorder increases. Therefore the spring constant disorder states stay extended for a much larger range of frequencies. The unprecedented disruption to the low frequency states in the spring constant disordered system beyond the BP suggests that the BP frequency must be of some significance. We therefore investigate the nature of the states further in Chap. 7.

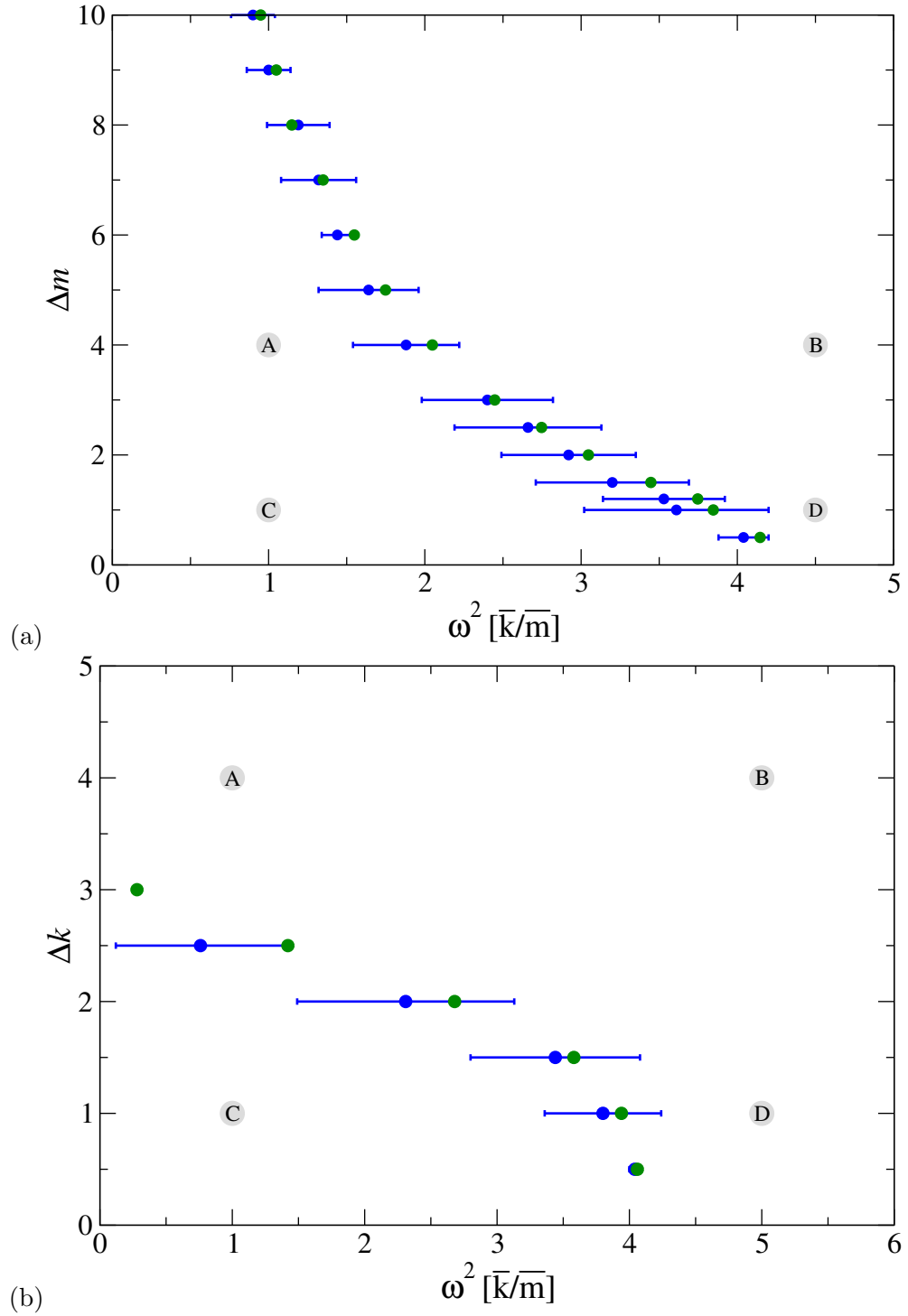


Figure 5.6: Frequencies of peaks in the reduced VDOS $g(\omega)/\omega^2$ as a function of squared frequency ω^2 and disorder (a) Δm and (b) Δk for both numerical diagonalisation (blue) and CPA (green) studies. In both cases the positions with large grey circles labelled (a)-(d) denote the positions of the states found in Figs. 5.7 and 5.8 for mass and spring constant disorder, respectively.

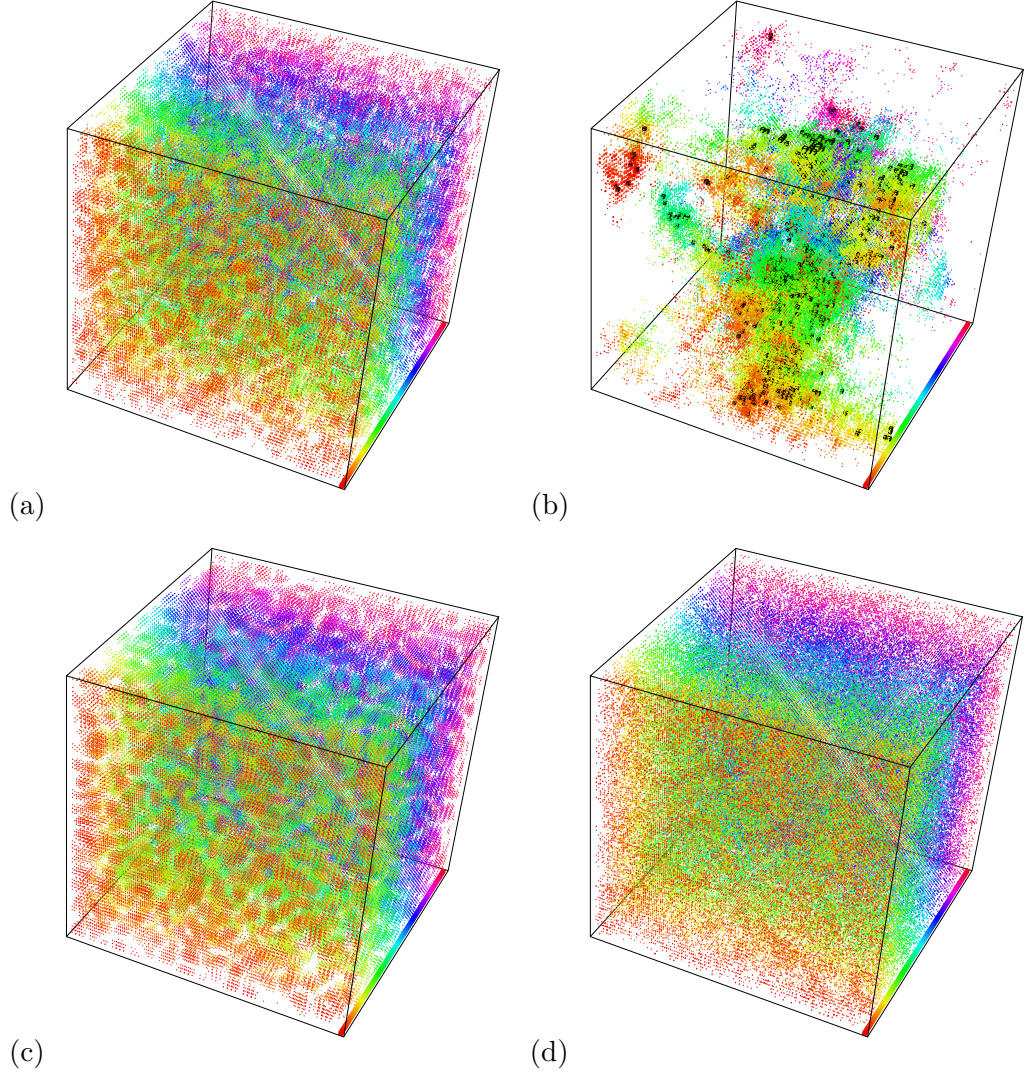


Figure 5.7: Representation of displacement distributions $|u_j|$ obtained from exact diagonalisation for system of length $L^3 = 70^3$. All sites with $u(\vec{r}_j)/L^3 \sum_j u(\vec{r}_j) > 1$ are shown as small cubes and those with black edges have $u(\vec{r}_j)/L^3 \sum_j u(\vec{r}_j) > \sqrt{1000}$ and $|u_j| < \langle |u_j| \rangle$ are not displayed. The colour scale distinguishes between different slices of the system along the axis into the page. (a)-(d) relate to the position within the BP trajectories in Fig. 5.6(a) that are marked as grey shaded circles labelled (a)-(d). The frequency and disorder for the states is (a) $\Delta m = 4$ and $\omega^2 = 1$, (b) $\Delta m = 4$ and $\omega^2 = 4.5$, (c) $\Delta m = 1$ and $\omega^2 = 1$ and (d) $\Delta m = 1$ and $\omega^2 = 4.5$.

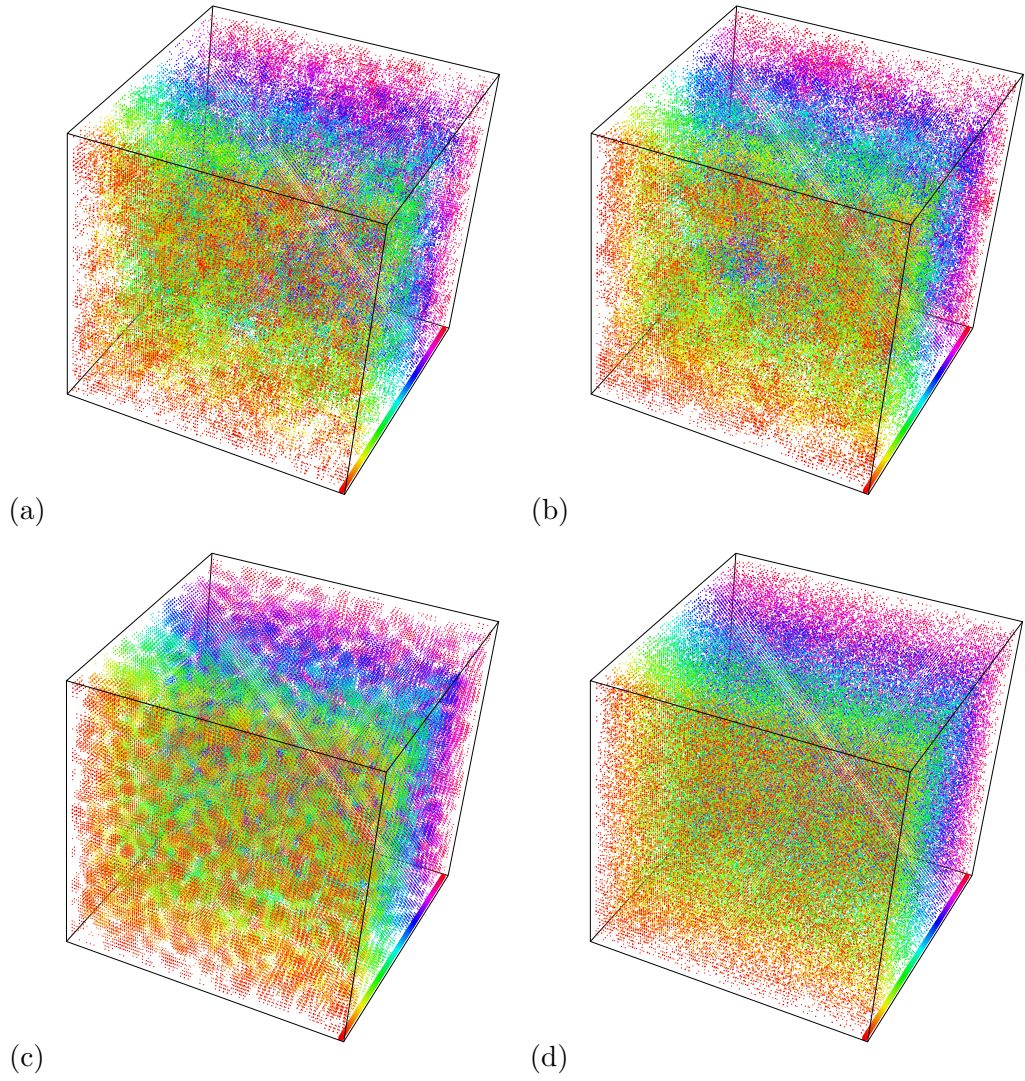


Figure 5.8: Representation of displacement distributions $|u_j|$ with properties as in Fig. 5.7. (a)-(d) relate to the position within the BP trajectories in Fig. 5.6(b) that are marked as grey shaded circles labelled ①-④. The frequency and disorder for the states is (a) $\Delta k = 4$ and $\omega^2 = 1$, (b) $\Delta k = 4$ and $\omega^2 = 5$, (c) $\Delta k = 1$ and $\omega^2 = 1$ and (d) $\Delta k = 1$ and $\omega^2 = 5$.

Chapter 6

Three Dimensional Localisation-Delocalisation Transition

So far we have only studied the normal modes, from which we have some evidence of a LDT for phonons with either mass or spring constant disorder. Until now a phonon LDT has been assumed in the literature to be in the high frequency regime near the band edge [33, 81, 102, 122]. This is based on analysis of the normal modes and mainly for systems containing spring constant disorder as the disorder is easier to study due to the symmetry of the dynamical matrix. In this chapter we look towards other methods available to find the LDT.

6.1 Electronic Anderson Phase Boundary Conversion

The classical problem presented in Eqn. (5.2) is very similar to the tight-binding Schrödinger equation for the 3D AM of localisation, with Hamiltonian

$$\mathbf{H} = \sum_i \epsilon_i |i\rangle \langle i| - \sum_{i \neq j} t_j |i\rangle \langle j|, \quad (6.1)$$

where the summation is over all nearest-neighbours. The corresponding Schrödinger equation is

$$\begin{aligned} (E - \epsilon_{x,y,z})\psi_{x,y,z} &= -t_{x,y,z+1}\psi_{x,y,z+1} - t_{x,y,z-1}\psi_{x,y,z-1} - \\ &t_{x,y+1,z}\psi_{x,y+1,z} - t_{x,y-1,z}\psi_{x,y-1,z} - \\ &t_{x+1,y,z}\psi_{x+1,y,z} - t_{x-1,y,z}\psi_{x-1,y,z} \end{aligned} \quad (6.2)$$

where E is the energy, $\epsilon_{x,y,z}$ is the disorder potential at the given lattice site and t is the hopping term. Here $\psi_{x,y,z}$ is the electron wave-function amplitude that has a role equivalent to the displacements $u_{x,y,z}$ in the phonon system. The site indices i and j from Eqn. (6.1) have been converted to a cartesian form, where each index i and j is made up of an x , y and z site index. We have omitted the cartesian co-ordinates for site i from all hopping integrals for clarity. Comparing Eqns. (6.2) and (5.2), we find that

$$-\omega^2 m_{x,y,z} + k_{x,y,z+1} + k_{x,y,z-1} + k_{x,y+1,z} + k_{x,y-1,z} + k_{x+1,y,z} + k_{x-1,y,z} \equiv E - \epsilon_{x,y,z} \quad (6.3)$$

and $k_{x,y,z} \equiv t_{x,y,z}$. The present model of vibrations can hence also be thought of as an AM in which the potential disorder can be modelled by random masses and the on-site disorder by a combination of spring and mass disorder. For the case of pure mass disorder with $k_{x,y,z} = \bar{k}$ for all x, y, z , we then find

$$E = -\omega^2 \bar{m} + 6\bar{k}, \quad (6.4a)$$

$$\epsilon_{x,y,z} = \omega^2 (m_{x,y,z} - \bar{m}), \quad (6.4b)$$

$$t_{x,y,z} = \bar{k}, \quad (6.4c)$$

while for pure spring disorder with $m_{x,y,z} = \bar{m}$, we have

$$E = -\omega^2 \bar{m} + 6\bar{k}, \quad (6.5a)$$

$$\epsilon_{x,y,z} = (k_{x,y,z+1} \dots k_{x-1,y,z} - 6\bar{k}), \quad (6.5b)$$

$$t_{x,y,z} = k_{x,y,z}. \quad (6.5c)$$

From Eqns. (6.4) and (6.5), we immediately see that the spectrum for the *clean* case is non-negative, i.e. $0 \leq \omega^2 \leq 12\bar{k}/\bar{m}$. With the relations (6.4) and (6.5) we can also reuse many of the results for the AM [25, 131] for the phonon case. In particular, the analogy first of all establishes the existence of an LDT for the phonon model, starting from $\omega^2 = 12\bar{k}/\bar{m}$ for small disorder. The behaviour of the mobility edges for stronger disorder is not immediately clear. For pure mass disorder, Eqns. (6.4) imply a novel energy/frequency-dependent on-site disorder and for pure spring disorder, (6.5b) corresponds to a disorder distribution consisting of the sum of six independently chosen random numbers. Even when each $k_{x,y,z}$ is chosen according to the uniform distribution as above, the resulting distribution of $\epsilon_{x,y,z}$ is not similarly simple and has not previously been studied for the AM. Therefore, there are no readily available quantitative phase diagrams to compare with.

By setting $\bar{k} = \bar{m} = 1$ we now obtain the relations $E = -\omega^2 + 6$ and $\epsilon_{x,y,z} = \omega^2 (m_{x,y,z} - 1)$ from Eqns. (6.4a) and (6.4b) respectively. We introduce the parameter \mathcal{W} for the width of the electronic disorder distribution and compare the second moments of both sides of the latter reduced equation to obtain the final conversion relation.

$$\mathcal{P}(\epsilon) = \begin{cases} \frac{1}{\mathcal{W}}, & \text{if } -\frac{\mathcal{W}}{2} \leq \epsilon \leq \frac{\mathcal{W}}{2} \\ 0, & \text{otherwise} \end{cases},$$

$$\langle \epsilon^2 \rangle = 2 \int_0^{\frac{\mathcal{W}}{2}} \frac{1}{\mathcal{W}} \epsilon^2 d\epsilon = \frac{2}{\mathcal{W}} \left. \frac{\epsilon^3}{3} \right|_0^{\frac{\mathcal{W}}{2}} = \frac{\mathcal{W}^2}{12}, \quad (6.6)$$

$$\mathcal{P}(\gamma) = \begin{cases} \frac{1}{\Delta}, & \text{if } -\frac{\Delta}{2} \leq \gamma \leq \frac{\Delta}{2} \\ 0, & \text{otherwise} \end{cases},$$

$$\langle \beta^2 \rangle = \frac{\omega^4}{\Delta} \int_{-\frac{\Delta}{2}}^{\frac{\Delta}{2}} \gamma^2 d\gamma = \frac{\omega^4}{\Delta} \left[\frac{\gamma^3}{3} \right]_{-\frac{\Delta}{2}}^{\frac{\Delta}{2}} = \frac{\omega^4 \Delta^2}{12}. \quad (6.7)$$

Here $\gamma = m - 1$ and $\beta = \omega^2 \gamma$. Now equating $\langle \beta^2 \rangle \equiv \langle \epsilon^2 \rangle$ we find

$$\Delta m = \frac{\mathcal{W}}{|\omega^2|} \quad (6.8)$$

and with Eqns. (6.4a) and (6.8) we have the ability to transform the phase boundary obtained from the AM with continuous distribution disorder applied to the onsite potentials. The required phase boundaries are available in the literature and two such examples from Refs. [25, 131] are given in Fig. 6.1.

As Bulka et al. [25] have included a continuous phase boundary we digitise this and apply the transformation from Eqns. (6.4a) and (6.8) to obtain an estimate of the mobility edge for the mass disordered phase diagram. The schematic of the transformation is available in Fig. 6.2.

The phase diagram is intriguing in many respects. We first note that the region for $\omega^2 \geq 6$ corresponds to the $E \leq 0$ region in the AM and similarly $\omega^2 \leq 6$ is associated with $E \geq 0$. The much studied centre of the band at $E = 0$ for the AM becomes the much less distinct $\omega^2 = 6$. For $\omega^2 \leq 6$, we see that much of the extended phase belongs to the region of possible negative masses with $\Delta m > 2$. Furthermore, the $E \geq 0$, $\omega^2 \leq 6$ region also extends into negative values of ω^2 and hence *imaginary* frequencies. Here we see that the region of extended states for $E \geq 0$ gets transformed into a much reshaped form for $\omega^2 < 0$. The particular form of this puddle of extended states, towards the $\omega^2 = 0$ axis, is driven by the so-called re-entrant behaviour for the AM [25, 131]. Similarly, the re-entrant behaviour at

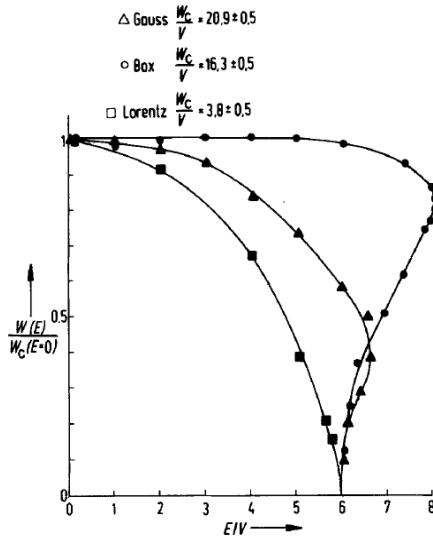


Fig. 1. Mobility edge trajectories $W_c(E)$ for the box (● $W_c(0)/V = 16.3 \pm 0.5$), Gaussian (▲ $W_c(0)/V = 20.9 \pm 0.5$), and the Lorentzian (■ $W_c(0)/V = 3.8 \pm 0.5$) distribution (a)

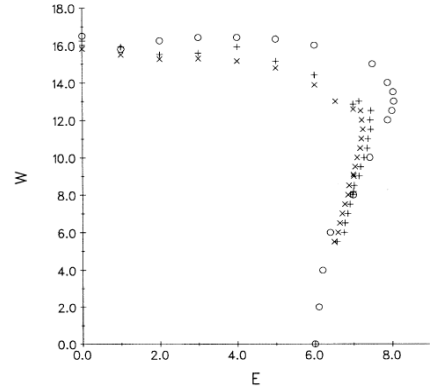


FIG. 3. The mobility edge trajectory in 3D as calculated by the TMM (○) (from Ref. 11) and the multifractal analysis via $\alpha(0)$ (×) and $\alpha(1)$ (+) for the box distribution. (b)

Figure 6.1: Phase diagram for the LDT of electrons plotted as a function of electronic energy E versus potential box distribution width W taken from (a) Ref. [25] and (b) Ref. [131].

$\omega^2 > 12$ can be traced to the corresponding re-entrant shape of the mobility edge at $E \lesssim -6$. As we will show in the rest of this chapter, these extraordinary mobility edges and hence the phase diagram for the mass disorder case are indeed confirmed by direct high-precision numerics.

The proceeding sections numerically confirm the mass disorder phase boundary that has been obtained with the above transformation. Additionally the LDT phase boundary of the spring constant disordered system up to and including disorder $\Delta k = 10$ is studied with high precision TMM simulations. The properties of LDTs are expected to be universal throughout the phase diagram with a universal critical exponent [44] characterising the transition. We expect to find via FSS that the critical parameters of the LDTs in the new, previously unexplored regions of the phase diagrams, are consistent with those at disorders $\Delta m < 2$ and $\Delta k < 2$. Furthermore, it is well known [132, 133] that values of critical parameters at the LDT can be affected in regions of low DOS. With the VDOS results obtained in Chap. 5 we can see for the mass disorder case above that the LDT for disorders $\Delta m < 2$ is near the band edge. For disorders $\Delta m > 2$ the band edge does not exist and the LDT moves closer to $\omega^2 = 0$. Bearing this in mind, the critical parameters for disorders $\Delta m > 2$ and $\Delta k > 2$ may be better estimated. The full phase boundary may

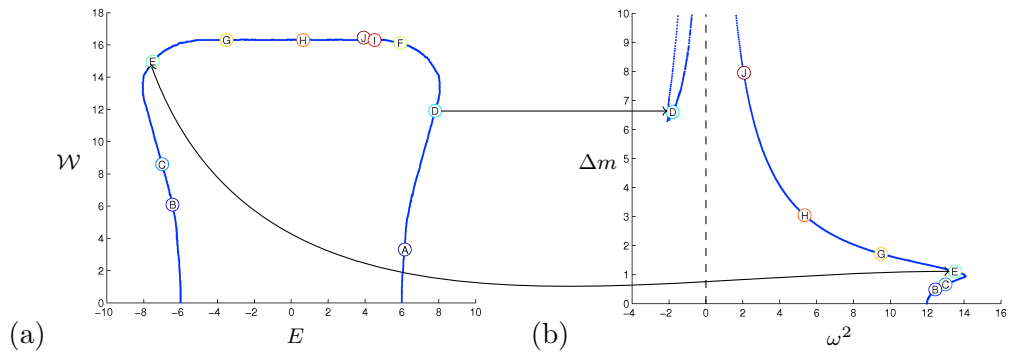


Figure 6.2: (a) Digitised electronic phase diagram from Ref. [25] for the LDT plotted as a function of electronic energy E versus potential disorder box distribution width \mathcal{W} and (b) corresponding phonon phase diagram for mass disordered system for squared frequency ω^2 versus mass disorder box distribution width Δm , obtained by applying the transformation in Eqn. (6.8). The phase boundary diverges to infinity as $\omega^2 \rightarrow 0$ from both negative and positive ω^2 . In the negative ω^2 region the phase boundary is from the transformation of the re-entrant behaviour for $E > 6$ in the the electronic case. Both ends of the phase boundary diverge to infinity when approaching zero and encapsulate extended modes into a “puddle”. The arbitrary minimum of this puddle is defined by the arbitrary maximum of E in the electronic phase diagram.

also prove useful for future conversions (using the transformation method above) to other quantum systems with Hamiltonians that incorporate nearest neighbour coupling and on-site interactions.

There are many reasons to investigate the phase diagram also for disorders Δm and $\Delta k > 2$. We indicate the usefulness of the results to a very interesting new avenue of research on acoustic metamaterials [75]. Hence hitherto unexplored and deemed unphysical regions of the phase diagram for disordered vibrations — those with apparently *negative* masses and spring constants — are now recognised to be of considerable interest for metamaterial applications and offer an entirely novel perspective of Anderson localisation. Let us emphasise that systems with such negative masses and stiffnesses have already been built, e.g. arrays of sub wavelengths Helmholtz resonators [75]. These devices show negative acoustic refraction as well as promise for acoustic superlensing and cloaking applications. Acoustic metamaterials that have been built thus far exhibit an effective negative mass and operate via resonance effects around specific frequencies [134]. Taking a set of those units, slightly detuned individually to be off resonance, will result in a distribution of Δm values. This distribution can be constructed, at least in principle, to mimic the uniform distribution assumed here. When we cross the threshold values $\Delta m, \Delta k = 2$ into the unstable regime, we find that the general characterisation of the vibrational states into extended, critical and localised remains and that the mobility edges continue to exist. We see that upon further increasing the disorder, we retain large regions of extended states, particularly for the case of spring disorder. This implies that extended vibrations — and hence their transport of vibrational energy — in acoustic metamaterials are robust with respect to sizeable amounts of disorder suggesting that acoustic cloaking devices do not need to be perfect. The regimes of extended states for $\omega^2 < 0$ have a particular relevance for acoustic metamaterials. Namely, they show that the disorder in masses and springs can give rise to an attenuation in time of the vibrations throughout all of space. This then indicates that it should be possible to build acoustic cloaking devices which have cloaking properties in some regions, but also damping/attenuation characteristics in others. Other model systems that exhibit a similar LDT to that of the spring constant disorder case on the $\omega^2 < 0$ side is instantaneous-normal mode spectra [135]. The significance of the delocalised unstable modes to the energy landscape of a liquid remains to be discussed.

6.2 Transfer Matrix Method

The TMM is a memory efficient way to iteratively calculate the dimensionless decay length Λ_M of vibrations in a quasi-1D bar with cross section $M \times M$ for lengths $L \gg M$. Eqn. (5.2) has to be rearranged into a form where the amplitude of vibration of a site in layer $x + 1$ — when x is chosen as the direction of transfer — is calculated solely from parameters of sites in previous layers x and $x - 1$,

$$\begin{aligned} u_{x+1,y,z} &= -\frac{1}{k_{x+1,y,z}} [(\omega^2 m_{x,y,z} + k_{\text{all}})u_{x,y,z} - H_x] - \frac{k_{x-1,y,z}}{k_{x+1,y,z}} u_{x-1,y,z} \\ H_x &= k_{x,y,z+1}u_{x,y,z+1} + k_{x,y,z-1}u_{x,y,z-1} + k_{x,y+1,z}u_{x,y+1,z} + k_{x,y-1,z}u_{x,y-1,z} \\ k_{\text{all}} &= k_{x,y,z+1} + k_{x,y,z-1} + k_{x,y+1,z} + k_{x,y-1,z} + k_{x+1,y,z} + k_{x-1,y,z}. \end{aligned} \quad (6.9)$$

H_x denotes the collection of in-plane contributions to the final amplitude and k_{all} is the sum of all surrounding spring constants. U_x is a collection of all in place displacements and is ordered as $U_x = (u_{x,1,1}, u_{x,1,2}, u_{x,2,1}, \dots, u_{x,M,M})$. We therefore define U_x , U_{x+1} and U_{x-1} as vectors containing the amplitudes of the constituent sites in layers x , $x + 1$ and $x - 1$, respectively. Eqns. (6.9) can now be expressed in standard TMM form

$$\begin{bmatrix} U_{x+1} \\ U_x \end{bmatrix} = \underbrace{\begin{bmatrix} -\frac{[(\omega^2 m_x + k_{\text{all}})\mathbf{1} - \mathbf{H}_x]}{k_{x+1}} & -\frac{k_{x-1}}{k_{x+1}}\mathbf{1} \\ \mathbf{1} & \mathbf{0} \end{bmatrix}}_{\mathbf{T}_n} \begin{bmatrix} U_x \\ U_{x-1} \end{bmatrix}, \quad (6.10)$$

where \mathbf{H}_x is an $M \times M$ matrix containing all in-layer contributions and $\mathbf{0}$, $\mathbf{1}$ are the $M \times M$ zero and unit matrices, respectively. Formally, the transfer-matrix \mathbf{T}_n is used to ‘transfer’ vibrational amplitudes U from one slice to the next and repeated multiplication of this gives the global transfer matrix $\tau_L = \prod_{x=1}^L \mathbf{T}_n$. The limiting matrix $\Gamma \equiv \lim_{L \rightarrow \infty} (\tau_L \tau_L^\dagger)^{\frac{1}{2L}}$ exists [78] and has eigenvalues $e^{\pm\gamma_i}$, $i = 1, \dots, M$. The inverse of these Lyapunov exponents γ_i are estimates of localisation lengths and the physically relevant largest localisation length is $\lambda_M(\omega^2) = 1/\min_i [\gamma_i(\omega)]$. The reduced (dimensionless) decay/localisation length may then be calculated as $\Lambda_M(\omega^2) = \lambda_M(\omega^2)/M$.

6.2.1 Numerical Method

Numerically it is more convenient to implement Oseledec’s theorem to obtain the Lyapunov exponents in a different manner to that described above. We begin with a set of orthonormal vectors, each one being a starting condition for the TMM of the

form of U_x . We arrange the starting vectors as the columns of a matrix \mathbf{U}_x the size of which is $M^2 \times M^2$. For simplicity the orthonormal set of vectors is usually chosen to be that of an identity matrix where each starting vector initiates the vibration at only one of the $M \times M$ sites in the first two layer of the lattice. Therefore, all of the available amplitude is located at a single site. Note that the vibrational amplitudes of the first two layers of the system are required for the calculations to proceed, and we connect them with perfect interconnecting spring constants.

We perform the matrix multiplication \mathbf{T}_n (as seen in Eqn. (6.10)) on the starting orthonormal vectors described above, where the in-plane terms in \mathbf{T}_n are treated with periodic boundary conditions and the required disorder is introduced to the system within \mathbf{T}_n . This results in a new set of vectors (\mathbf{U}_{x+1}) on which the process is repeated, this time using the new set as \mathbf{U}_x , and the previous set as \mathbf{U}_{x-1} .

Due to machine precision and the possibility of exponential growth of the vectors, we tend to lose orthogonality after only a few matrix multiplications. We re-orthonormalise the vectors at regular intervals (usually after every tenth matrix multiplication) using the Gram-Schmidt scheme [136]. Numerical application of the Gram-Schmidt scheme is the most time consuming part of the code and its computation reduces the ability to parallelise the code efficiently [137]. The re-orthonormalisation is required so that all U_x vectors yield different Lyapunov exponents and that the smallest may definitely be found in order to obtain the largest localisation length $\lambda_M(\omega^2) = 1/\min[\gamma_i(\omega)]$. The Gram-Schmidt process is as follows, we use $\{U_x^{(1)}, U_x^{(2)}, \dots, U_x^{(N)}\}$ as a set of k linearly independent vectors that span some vector space. We now use $\{V_x^{(1)}, V_x^{(2)}, \dots, V_x^{(k)}\}$ as the orthogonal set of normalised vectors to be determined. We calculate $V_x^{(1)}$ by setting $W^{(1)} = U_x^{(1)}$ to obtain

$$V_x^{(1)} = \frac{W^{(1)}}{\langle W^{(1)}, W^{(1)} \rangle^{1/2}} \quad (6.11)$$

such that $V_x^{(1)}$ is normalised. We set $W^{(2)} = U_x^{(2)} - \langle U_x^{(2)}, V_x^{(1)} \rangle V_x^{(1)}$ so that $W^{(2)}$ is orthogonal to $V_x^{(1)}$ and therefore

$$V_x^{(2)} = \frac{W^{(2)}}{\langle W^{(2)}, W^{(2)} \rangle^{1/2}}. \quad (6.12)$$

Again $V_x^{(2)}$ is normalised, and crucially, orthogonal to $V_x^{(1)}$. The process is continued until all V_x are determined. In general assuming that the necessary V_x are calculated,

$W^{(k)}$ are of the form

$$W^{(k)} = U_x^{(k)} - \langle U_x^{(k)}, V_x^{(k-1)} \rangle V_x^{(k-1)} - \langle U_x^{(k)}, V_x^{(k-2)} \rangle V_x^{(k-2)} - \dots - \langle U_x^{(k)}, V_x^{(1)} \rangle V_x^{(1)} \quad (6.13)$$

so that $W^{(k)}$ is orthogonal to $V_x^{(1)}, V_x^{(2)}, \dots, V_x^{(k-1)}$. The final normalisation of $W^{(k)}$ yields

$$V_x^{(k)} = \frac{W^{(k)}}{\langle W^{(k)}, W^{(k)} \rangle^{1/2}}. \quad (6.14)$$

We have therefore produced a new set of orthonormal vectors V_x based on the original set of linearly independent set U_x . All V_x vectors are a linear combination of the original set and therefore span the same vector space and carry the same information.

Post orthogonalisation the vectors are, automatically as the iteration proceeds, arranged in descending order of their norms so that the final vector U_{M^2} is the eigenvector corresponding to the smallest Lyapunov exponent γ_{\min} . We therefore compute an estimate of the largest localisation length in the system using the formula

$$\gamma_{\min}^N = \frac{1}{N} \sum_{j=1}^n \ln \|U_{M^2}^{jN/n}\|. \quad (6.15)$$

Where N is the total number of transfer matrix multiplications and n is the number of times that the Gram-Schmidt orthogonalisation has been completed. The standard deviation $\delta\gamma_{\min}^N$ of the estimate γ_{\min}^N is calculated as a relative error which is the standard deviation of the Lyapunov exponent divided by itself and therefore given as

$$\frac{\delta\gamma_{\min}^N}{\gamma_{\min}^N} = \frac{1}{n} \sqrt{\frac{n \sum_{j=1}^n \left(\ln \|U_{M^2}^{jN/n}\| \right)^2}{\left(\sum_{j=1}^n \ln \|U_{M^2}^{jN/n}\| \right)^2} - 1}. \quad (6.16)$$

Using the standard progression of error formulation on the inverse relation between γ and λ , the relative error of the Lyapunov exponent is also equal in magnitude to that of the relative error of the estimated localisation length λ .

6.3 Localisation Lengths

We perform TMM calculations for mass disorders $\Delta m = 0.2, 0.4, \dots, 2.2$ and also 4, 6 and 9, whilst for spring constant disorder Δk we use the values 0.2 to 2.2 in steps of 0.2 and 3 to 10 in steps of 1. The average of the mass and spring constant disorder distributions has been kept fixed at 1 for all cases ($\bar{m} = \bar{k} = 1$). For every

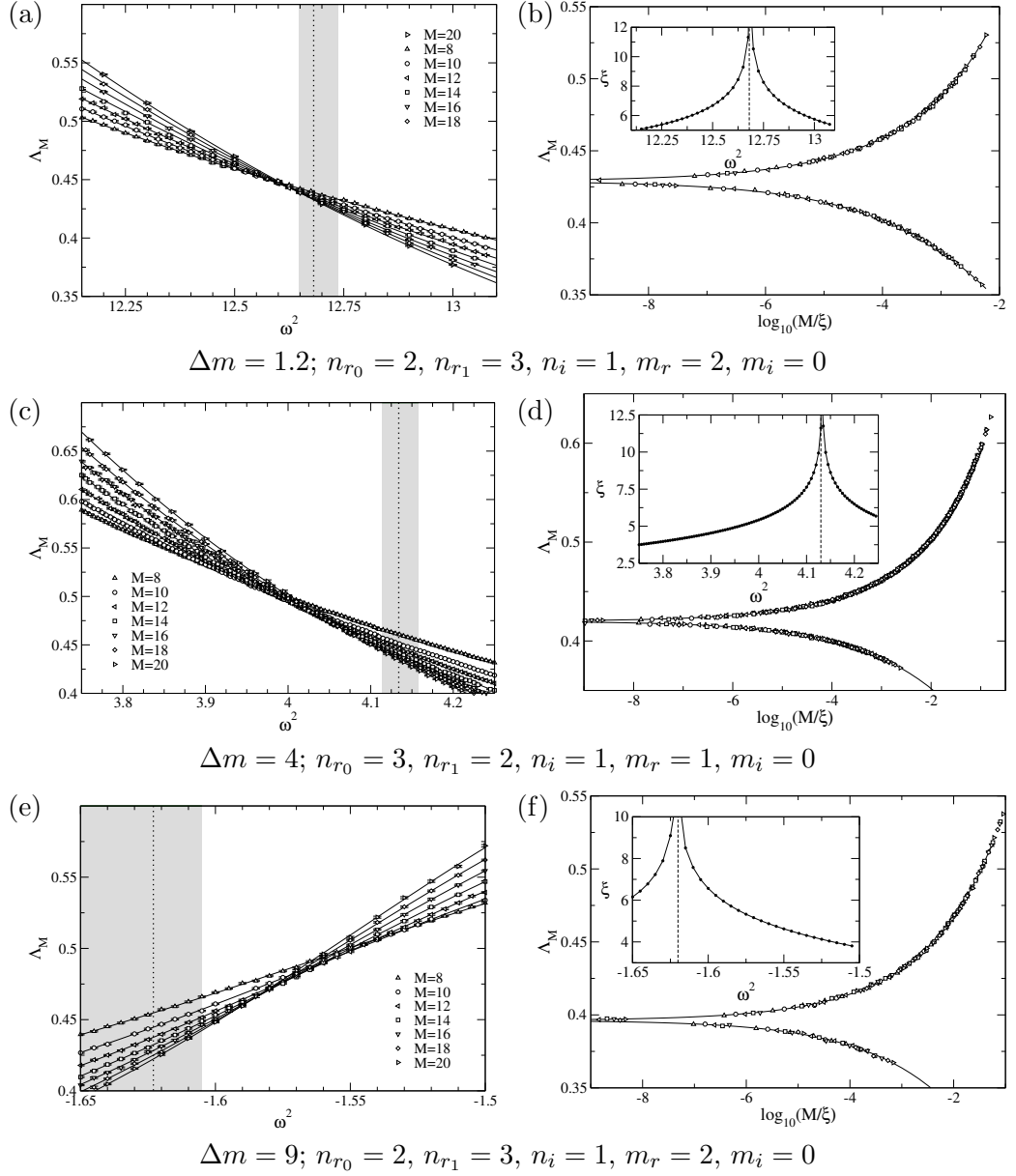


Figure 6.3: Reduced localisation lengths $\Lambda_M(\omega^2)$ plotted as function of squared frequency ω^2 for quasi-1D system sizes indicated by different symbols. From top to bottom box distributed uniform mass disorder widths $\Delta m = 1.2, 4$ and 9 . The solid lines in the left column (a,c,e) show the fits obtained from FSS, the orders of expansion ($n_{r_0}, n_{r_1}, n_i, m_r, m_i$) of the FSS stable fits (Sec. 6.3.1) are given below each figure. The right column (b,d,f) display the obtained scaling function when the irrelevant components have been subtracted. The vertical dotted line represents the estimated values of the critical parameter ω_c^2 from FSS, where grey shading indicates the unsymmetric error obtained from Monte Carlo analysis (Sec. 6.3.1). The insets show the correlation lengths.

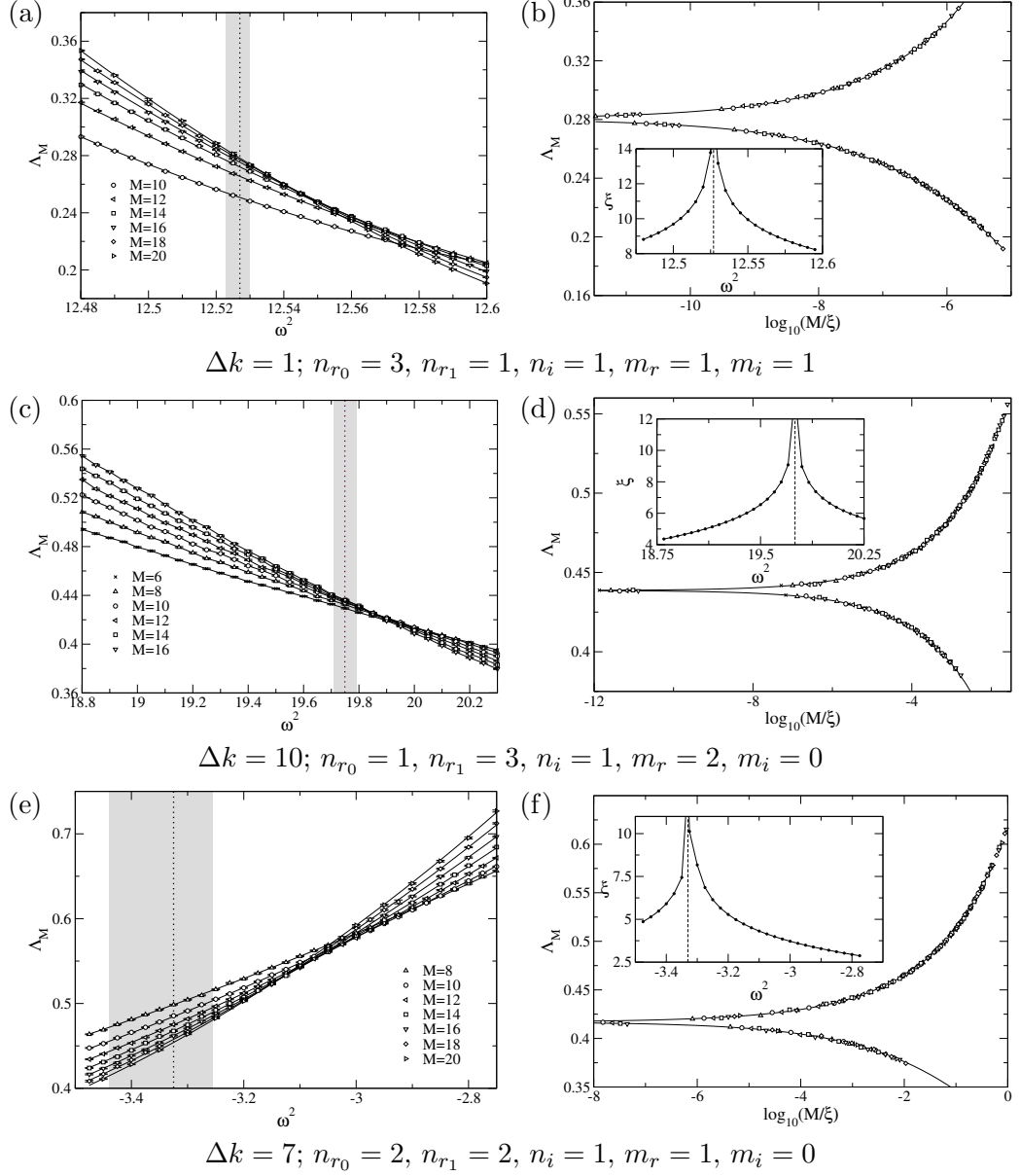


Figure 6.4: Reduced localisation lengths $\Lambda_M(\omega^2)$ for box distributed uniform spring constant disorder widths from top to bottom $\Delta k = 1, 7$ and 10 . All shadings and labels are as in Fig. 6.3.

disorder value, Λ_M has been calculated for a range of frequencies and system widths $M = 6, 8, 10$ and 12 to an accuracy of 0.1 percent of the standard deviation. In Figs. 6.3(a)(c)(e) and 6.4(a)(c)(e), we show the resulting disorder and frequency dependencies for 3 representative mass and spring constant disorder regions. At all disorder magnitudes for both spring constant and mass disorder, these figures reveal clear transitions from extended behaviour, with increasing Λ_M values for increasing M , to localised behaviour, where Λ_M decreases when M increases. We also see in these figures frequency regions where Λ_M remains roughly constant upon changing M . Such regions are in the vicinity of a change from delocalisation to localisation and hence Figs. 6.3(a)(c)(e) and 6.4(a)(c)(e) indicate the possible existence of a LDT. For all disorder magnitudes we locate an initial estimate of the transition using system widths $M = 6, 8, 10$ and 12 . We estimate this transition region roughly by the frequency value at which the values of Λ_M cross for system widths $M = 10$ and 12 . We obtain a similarly rough estimate of the error of this estimate from the difference with respect to the frequency value which we obtain when we take the crossing point between $M = 12$ and 6 . Most interestingly, the predicted re-entrant behaviour in the complex frequency spectrum of the mass disorder phase diagram Fig. 6.2 is also observed in the TMM results. The small pocket of extended states in the phase diagram is clearly identified by the two transitions from localised to delocalised and back to localised at $\Delta m = 9$ as seen in Fig. 6.5.

6.3.1 Finite Size Scaling

In order to obtain more reliable estimates for the transition frequency ω_c^2 and to ascertain the existence of a divergent correlation length ξ , that scales such that

$$\xi(\omega^2) \propto |\omega^2 - \omega_c^2|^{-\nu} \quad (6.17)$$

at ω_c^2 with critical exponent ν ; we need to proceed to the $M \rightarrow \infty$ limit. Assuming that the one parameter scaling law [28] applies, the only relevant length scale in the system is the correlation/localisation length $\xi_{L \rightarrow \infty}$. According to the one parameter scaling theory, the dimensionless localisation lengths Λ_M for different system sizes and frequencies around the critical frequency ω_c^2 are described by the one scaling function

$$\Lambda_M = f\left(\frac{M}{\xi}\right). \quad (6.18)$$

All values of $\Lambda_M(M, \omega^2)$ collapse onto the scaling function which has two branches (as seen in Figs. 6.4(b)(d)(f) and 6.3(b)(d)(f)), one for localised ($\omega^2 > \omega_c^2$) and the

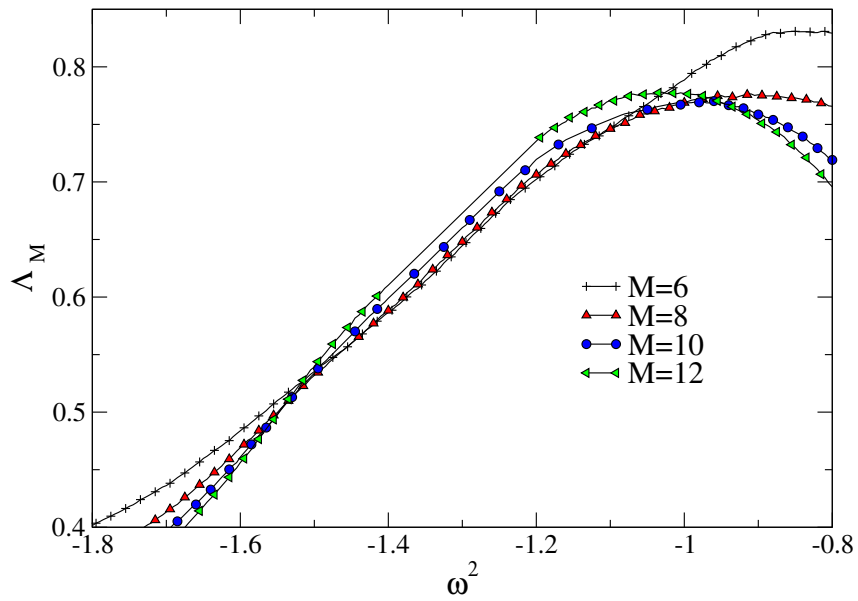


Figure 6.5: Two transitions (localised-delocalised-localised) in the negative squared frequency regime for box distributed mass disorder with width $\Delta m = 9$. Data points obtained with the TMM set to an accuracy of 0.1% of the variance. Error bars are within symbol size and therefore not shown, lines are linear interpolations between data points. For clarity only every fourth symbol is shown.

other for extended ($\omega^2 < \omega_c^2$). From the first order approximation in Eqn. 6.17, the scaling function can be expressed as $f(wM^{\frac{1}{\nu}})$ where w is the dimensionless squared frequency given as $w = (\omega_c^2 - \omega^2)/\omega_c^2$ and the critical exponent ν defines the divergence of the correlation length near the critical frequency. Since the scaling function equals zero at the critical frequency, we can Taylor expand around the critical frequency to obtain

$$\Lambda_M = \Lambda_c + a_1 w M^{\frac{1}{\nu}} + a_2 w^2 M^{\frac{2}{\nu}} + \dots \quad (6.19)$$

where the first term is the critical value at the critical frequency ω_c^2 . Fitting $\Lambda_M(M, \omega^2)$ near to the transition frequency to the above Taylor expanded function would obtain accurate estimates of the transition frequency and the critical exponent. Plotting $\Lambda_M(M, \omega^2)$ for all ω^2 will show the transition frequency ω_c^2 as a scale invariant common crossing point for many values of M .

As we are unlikely to be close to the thermodynamic limit in our simulations we apply a FSS procedure [37] that includes two types of corrections to scaling, namely those which account for the nonlinearities of the disorder (Δm or Δk) dependence of the scaling variables (relevant scaling) and those for the systematic shift of the point at which the $\Lambda_M(\omega^2)$ data cross (irrelevant scaling). The starting point for this FSS in terms of ω^2 is the scaling ansatz

$$\Lambda_M(\omega^2) = f\left(\chi_r M^{\frac{1}{\nu}}, \chi_i M^y\right). \quad (6.20)$$

This represents a simplified renormalisation group equation that expresses the reduced localisation length Λ_M as a function of the scaling variables, where χ_r and χ_i are the relevant and irrelevant scaling variables, respectively. Note that $y < 0$, so that as the system gets larger the contribution of the irrelevant scaling variable χ_i is reduced. As discussed above and in Sec. 2.2.2, for these larger systems where the irrelevant variables become negligible, we would find the one parameter scaling law. We make a Taylor expansion of the irrelevant scaling variable up to the order n_i , so that

$$\Lambda_M = \sum_{n=0}^{n_i} \chi_i^n M^{ny} f_n\left(\chi_r M^{\frac{1}{\nu}}\right), \quad (6.21)$$

from where we obtain a series of functions f_n which are in turn Taylor expanded up to an order n_r giving

$$f_n\left(\chi_r M^{\frac{1}{\nu}}\right) = \sum_{k=0}^{n_r} a_{nk} \chi_r^k M^{\frac{k}{\nu}}. \quad (6.22)$$

Nonlinearities are taken into account by expanding both χ_i and χ_r in terms of the w such that

$$\chi_r(w) = \sum_{m=1}^{m_r} b_m w^m, \quad \chi_i(w) = \sum_{m=0}^{m_i} c_m w^m, \quad (6.23)$$

where the orders of the expansions are m_r and m_i . This gives the number of expansion parameters as

$$N_p = (n_i + 1)(n_r + 1) + m_r + m_i + 2. \quad (6.24)$$

For more control over the increase of expansion parameters we hard-code the zero-th and first order of the irrelevant expansion assuming that higher orders will not be required. We then Taylor expand each appearance of f_n independently [138]. This now makes N_p of the form

$$N_p = n_i + n_{r_0} + n_{r_1} + m_r + m_i \quad (6.25)$$

and an increase to either expansion parameter by one only increases the total degrees of freedom by one. It is understood that each individual data set is best suited to a particular expansion, the general rule being that the orders of expansion (and total degrees of freedom) should be kept as low as possible while giving the best fit to the data ($\Gamma_q > 0.1$ by minimising χ^2); and minimising the estimated standard errors for the critical parameters ω_c^2 and ν . The expansions of the fit functions and the fit itself are performed using the function **NONLINEARMODELFIT** in MATHEMATICA[®] up to the orders n_{r_0} , n_{r_1} , n_i , m_i and m_r , where previously n_{r_0} and n_{r_1} would be equal to n_r . The minimisation is performed iteratively using the Levenberg-Marquardt method [139, 140]. We check for stability of the fit by individually increasing each expansion parameter by one and confirming that the newly obtained parameters remain within the 95% confidence intervals of the original fit.

As mentioned above, χ^2 is minimised automatically and can be calculated using the relation

$$\chi^2 = \sum_{i=1}^N \left(\frac{\Lambda_{Mi} - f(w_i)}{\sigma_i} \right)^2 \quad (6.26)$$

where σ_i is the standard deviation. A fit is considered reasonable if $\chi^2 \approx \mu$, where μ is the degrees of freedom of the fit, and defined as the number of data points less the number of fitting parameters. We additionally examine the probability distribution

of different values of χ^2 . For this, we require the function Γ_p , defined as

$$\Gamma_p(a, z) = \frac{\int_0^z t^{a-1} e^{-t} dt}{\int_0^\infty t^{a-1} e^{-t} dt}. \quad (6.27)$$

Here $\Gamma_p(\frac{\mu}{2}, \frac{\chi^2}{2})$ gives the probability that the observed χ^2 value for a correct fit is less than χ^2 . It is more convenient to define $\Gamma_q = 1 - \Gamma_p$, then the closer $\Gamma_q(\frac{\mu}{2}, \frac{\chi^2}{2})$ to 1 the better the fit. Generally the fit is considered good if $\Gamma_q(\frac{\mu}{2}, \frac{\chi^2}{2}) > 0.1$, but if $\Gamma_q(\frac{\mu}{2}, \frac{\chi^2}{2}) \approx 1$ the fit is considered exceptional and it is reasonable to assume that errors of the original fit are overestimated. Therefore Monte Carlo error analysis is useful for additional “stability analysis” [138].

We apply the FSS procedure with full Monte Carlo error analysis outlined below, to the previously obtained reduced localisation lengths in Sec. 6.3. The fits from the FSS are plotted as the solid lines with the reduced localisation lengths in Figs. 6.3(a)(c)(e) and Figs. 6.4(a)(c)(e) for mass and spring constant disorders, respectively. The lines shown are for the stable fit with the lowest expansion coefficients, where the subcaptions in Fig. 6.3 are the coefficients.

Once a stable fit is found via Monte Carlo methods, we subtract all terms in the expansion that are governed by the irrelevant scaling exponent y from Λ_M . The corrected Λ_M is now described by the one parameter scaling law as in Eqn. (6.18) above. We plot the corrected Λ as a function of M/ξ in Figs. 6.3(b)(d)(f) and Figs. 6.4(b)(d)(f) to obtain the scaling function. We find both branches for the extended and localised regimes and that the corrected reduced localisation lengths collapse onto the scaling curve. Inset in the figures we plot the associated correlation lengths ξ as a function of frequency ω^2 . As expected the correlation lengths ξ have a power law dependance on ω^2 due to the enforcement of the dependance in the original scaling ansatz in Eqn. (6.20).

Monte Carlo Error Analysis

The error estimates for the critical parameters that are calculated within the proprietary fitting routine are difficult to verify and as such cannot necessarily be immediately trusted as accurate. We approximate errors based on a Monte Carlo method that tests the robustness of the fit itself. We first obtain an approximately stable fit using the standard FSS procedure outlined above. If all critical parameters obtained for the higher order expansions are within the 95% confidence intervals of the original critical parameters, the fit is provisionally accepted as stable. We then generate an artificial data set for which the stable fit has perfect goodness of fit

$\Gamma = 1$. We vary the synthetic data points according to a Gaussian distribution that has the standard deviation of the original set of data. The nonlinear fitting routine is repeated, with the same expansion indices to again obtain the critical parameters. This process is repeated 5000 times and histograms are produced for the critical parameters. Representative examples of the histograms are given in Figs. 6.6 and 6.7 for a mass disorder distribution of width $\Delta m = 1.2$ and spring constant disorder distribution of width $\Delta k = 1.0$, respectively. The Monte Carlo analysis is run for both the provisionally stable fit, and the higher order expansions used for stability analysis. New errors are estimated from the 95% confidence intervals of the obtained unsymmetric distributions. The fit is finally accepted as stable if the new estimated critical parameters from the Monte Carlo analysis are within error of the critical parameters of the higher order expansions that are also computed with Monte Carlo. We use the stable fit with the smallest number of expansion parameters and a goodness of fit $\Gamma_q > 0.1$ as the best stable fit. Increasing the number of expansion coefficients may increase the goodness of fit, but will also begin to unnecessarily account for fluctuations of data and reduce the quality of the critical parameters. We note that although unlikely, it is still possible at this stage to reject a fit and the process of finding a fit restarts for higher order expansions using the original proprietary routine. This in turn requires repetition of the Monte Carlo error estimation process.

For both Figs. 6.6 and 6.7, (a) is the histogram of the minimised χ^2 (Eqn. (6.26)). In (b), (c) and (d) we show the histograms of the critical parameters ν , ω_c^2 and y , respectively. In (e) we see the standard deviation of the synthetic data set, had the Gaussian been applied to the original data set. In (f) we see the histogram of goodness of fit Γ_q values. The distribution of Γ_q is almost flat, indicating that the statistical fluctuations applied to the synthetic data set of $\Gamma_q = 1$ alter the goodness of fit randomly. This ensures that the fit is accurately tested.

Finite Size Scaling comparison using both ω vs. ω^2

We now discuss the choice of spectral variable ω or ω^2 used to obtain the dimensionless scaling parameter w required for FSS. The case for scaling with either ω or ω^2 is not clear cut. Theories of thermal conductivity due to phonons are usually expressed in terms of frequency ω [69] but in many cases we see that ω^2 is a more natural unit to work with [79, 90, 99, 141], being analogous to the electron energy in the tight binding model and being the eigenvalue obtained from diagonalisation of the dynamical matrix. We also note that working with ω^2 reduces the additional complexity of converting to complex frequencies ω in the region of negative ω^2 . The

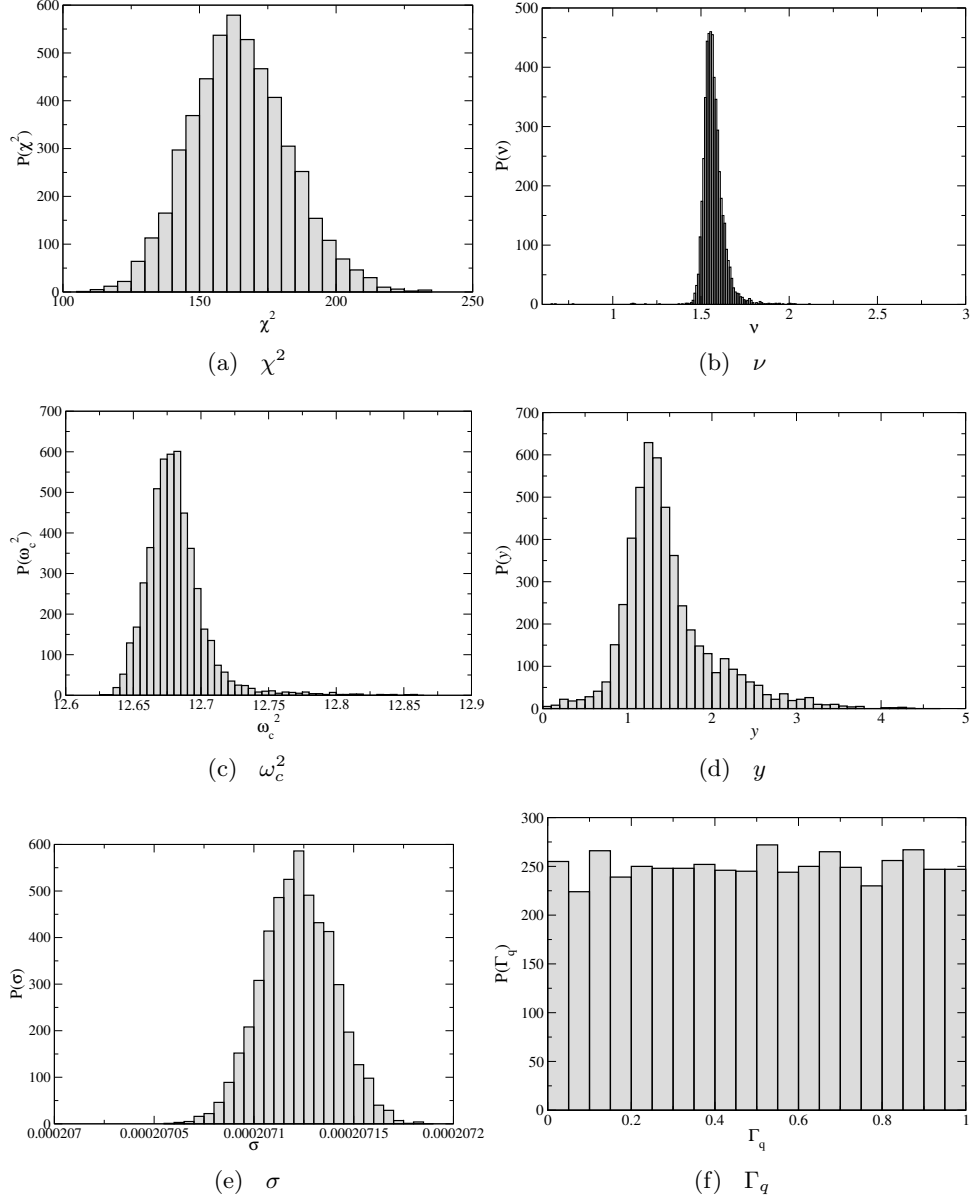


Figure 6.6: Monte Carlo error analysis histograms for critical parameters from 5000 fits. Critical parameters are for the LDT of the system with applied uniform box distributed mass disorder with width $\Delta m = 1.2$ for the expansion $n_{r_0} = 2$, $n_{r_1} = 3$, $n_i = 1$, $m_r = 2$, $m_i = 0$. The standard error of the data is obtained from the 95% confidence interval for unsymmetric distributions.

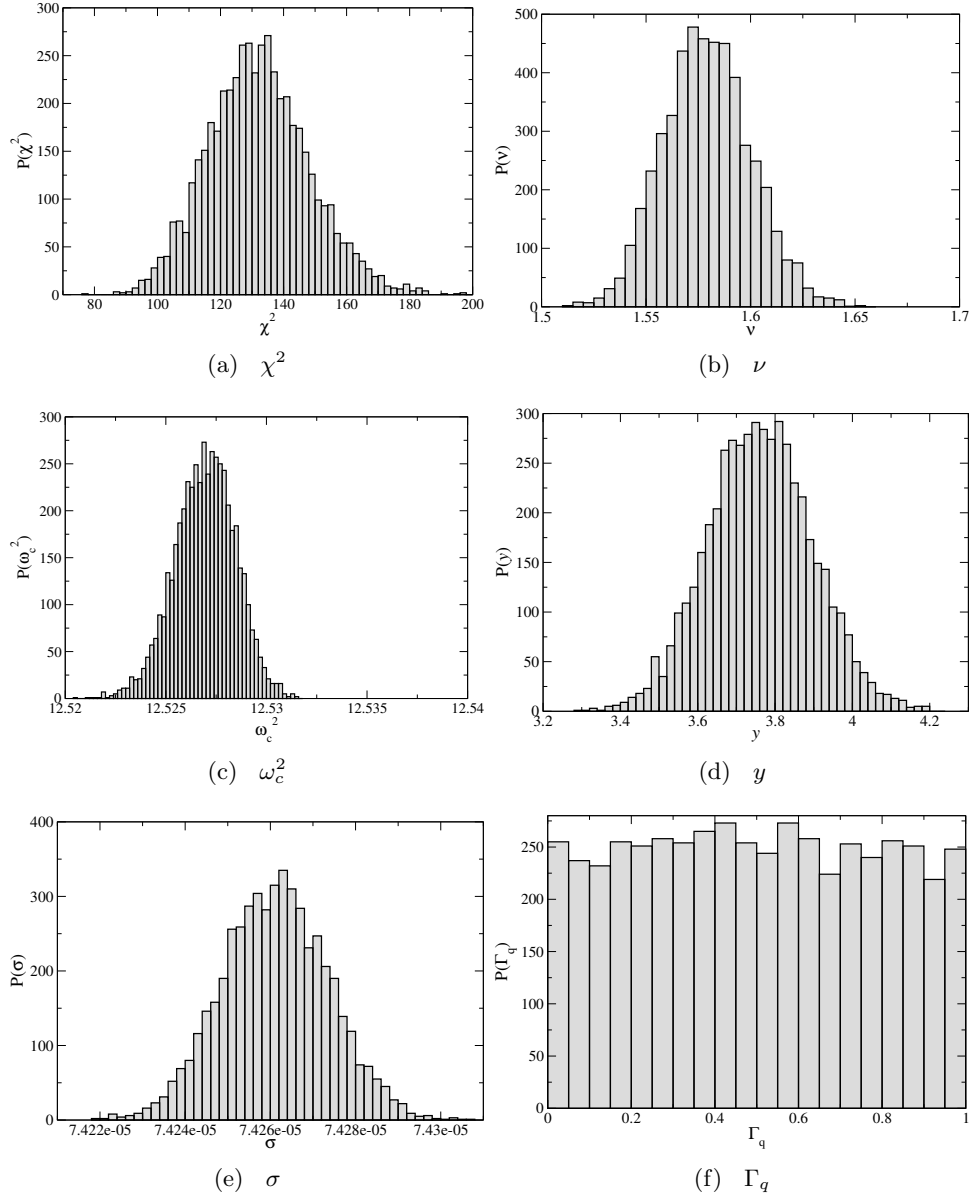


Figure 6.7: Similar to Fig. 6.6 for uniform box distributed spring constant disorder with width $\Delta k = 1$ for the expansion $n_{r_0} = 3$, $n_{r_1} = 1$, $n_i = 1$, $m_r = 1$, $m_i = 1$.

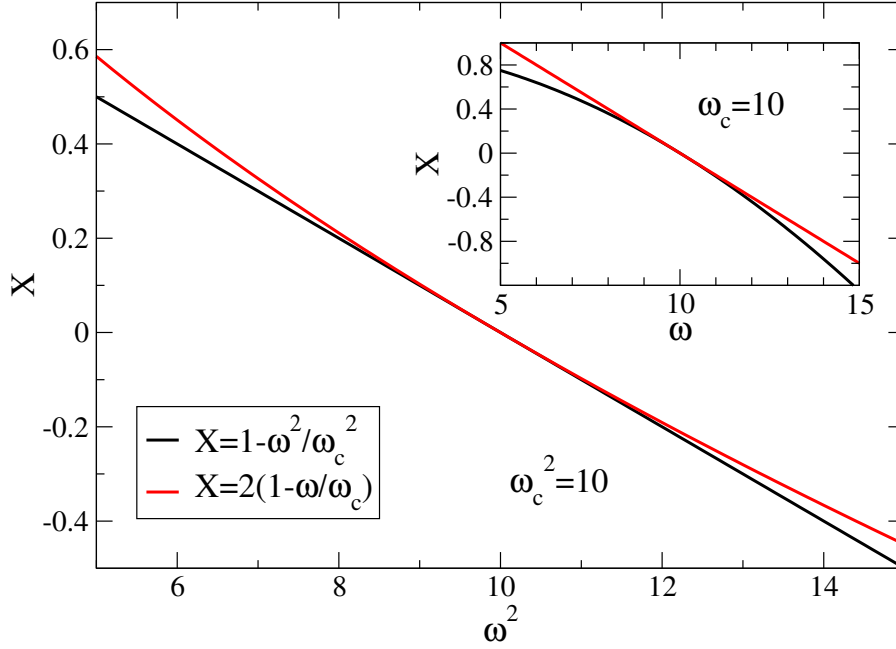


Figure 6.8: Comparison of scaling using dimensionless parameters obtained from either ω or ω^2 for a synthetic data set between $\omega^2 = 5-15$, using $\omega_c^2 = 10$. Inset is the same comparison but plotted as a function of ω using $\omega = 5-15$ and $\omega_c = 10$.

dimensionless parameter as mentioned before in Sec. 6.3.1 is calculated as

$$w = \frac{(W_c - W)}{W_c} \quad (6.28)$$

where W can represent either the quantity ω or ω^2 . We look towards a comparison of scaling between both parameters by using the ω^2 notation and working towards a comparable ω based dimensionless representation.

$$\begin{aligned} 1 - \frac{\omega^2}{\omega_c^2} &= \frac{1}{\omega_c^2}(\omega_c^2 - \omega^2) \\ &= \frac{1}{\omega_c^2}(\omega_c - \omega)(\omega_c + \omega) \\ &= \left(1 - \frac{\omega}{\omega_c}\right) \left(1 + \frac{\omega}{\omega_c}\right) \\ &\approx 2 \left(1 - \frac{\omega}{\omega_c}\right). \end{aligned} \quad (6.29)$$

We now pick some arbitrary units of ω or ω^2 and plot both forms on the same axis. We use a range of ω or $\omega^2 = 5$ to 15, and the critical value ω_c or $\omega_c^2 = 10$. In Fig. 6.8 we can see that the dimensionless units are most accurate at the critical

frequency and separate when away from the critical point. Close enough to the transition, very little difference between the two model exists. By definition the FSS equations are derived based on the assumption that data is close to the critical point [37]. Therefore we expect little change between FSS for both ω and ω^2 . For completeness we perform the scaling for the six chosen points, this time with the independent variable of ω . The results of the scaling curves are shown for mass and spring disorder in Figs. 6.9 and 6.10, respectively. For the interested reader, Appx. A contains tables for all lowest stable FSS fits and stability checking expansions for all six representative disorders in both ω and ω^2 .

6.3.2 Critical Parameters

We choose 3 disorder values for each disorder type, from the 3 different domains of the phase diagrams of Figs. 6.12 and Figs. 6.13, namely (i) $\omega^2 \geq 0$, $\Delta m, \Delta k < 2$, (ii) $\omega^2 \geq 0$, $\Delta m, \Delta k \geq 2$, and (iii) $\omega^2 < 0$. For mass disorder, we have (i) $\Delta m = 1.2$ at $\omega^2 \approx 12.83$, (ii) $\Delta m = 4$ at $\omega^2 \approx 4.12$ and (iii) $\Delta m = 9$ at $\omega^2 \approx -1.61$ and for spring constant disorder (i) $\Delta k = 1$, $\omega^2 \approx 12.61$, (ii) $\Delta k = 6$, $\omega^2 \approx 12.85$, and (iii) $\Delta k = 7$ at $\omega^2 \approx -3.33$. For these six points, we have computed additional high-precision data for $M = 14, 16, 18$ and 20 . The additional Λ_M values for these six transitions have also been shown in Figs. 6.3(a)(c)(e) and 6.4(a)(c)(e) plotted as functions of ω^2 and Figs. 6.9(a)(c)(e) and 6.10(a)(c)(e) as functions of ω .

We apply the FSS procedure of Sec. 6.3.1 to obtain the lowest order stable fits and hence obtain precise estimates of the critical parameters and transition frequencies ω_c^2 of a vibrating solid at the thermodynamic limit. In Tab. 6.1, we show results for the stable fits obtained from high-precision FSS analysis at the six representative points mentioned above. All critical parameters are shown for scaling with the dimensionless independent variables derived from ω^2 and ω . For full tables that include the higher order fits used to test stability, please see Appx. A. We find that in all cases, a consistent, robust and stable fit can be found with goodness of fit parameter Γ_q larger than 0.1. We see from the tables that the critical parameters obtained using either ω or ω^2 scaling are the same for identical disorders within error estimates. In most cases even the expansion indices of the stable fits themselves are identical for both ω and ω^2 . This indicates that we are close enough to the transition that the change in independent variable has little or no effect (see section 6.3.1).

In Fig. 6.11 we plot all critical exponents from both disorders (mass and spring constant) and both independent scaling variables (ω^2 and ω). We see that all critical exponents are consistent within error and all errors encapsulate the weighted

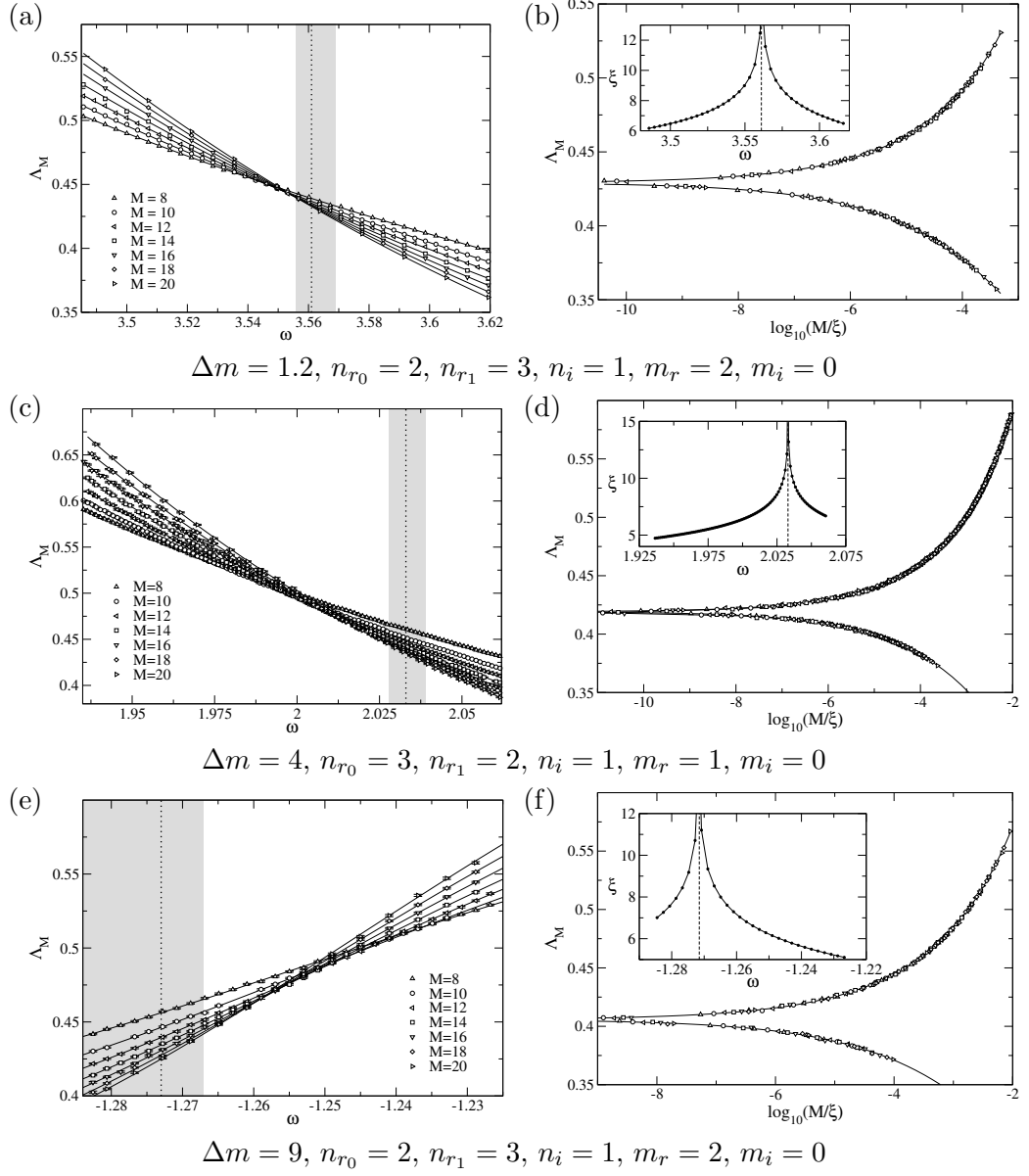


Figure 6.9: Reduced localisation lengths $\Lambda_M(\omega)$ plotted as function of frequency ω for various quasi-1D system sizes as indicated by different symbols for box distributed uniform mass disorder widths $\Delta k = 1.2, 4$ and 9 . The left column (a,c,e) show the fits obtained from FSS, the orders of the expansion are given below each figure, while the right column (b,d,f) display the obtained scaling function when the irrelevant components have been subtracted. The vertical dotted line represents the estimated values of ω_c^2 with grey shading indicating the unsymmetric error obtained from Monte Carlo analysis. The insets show the correlation lengths.

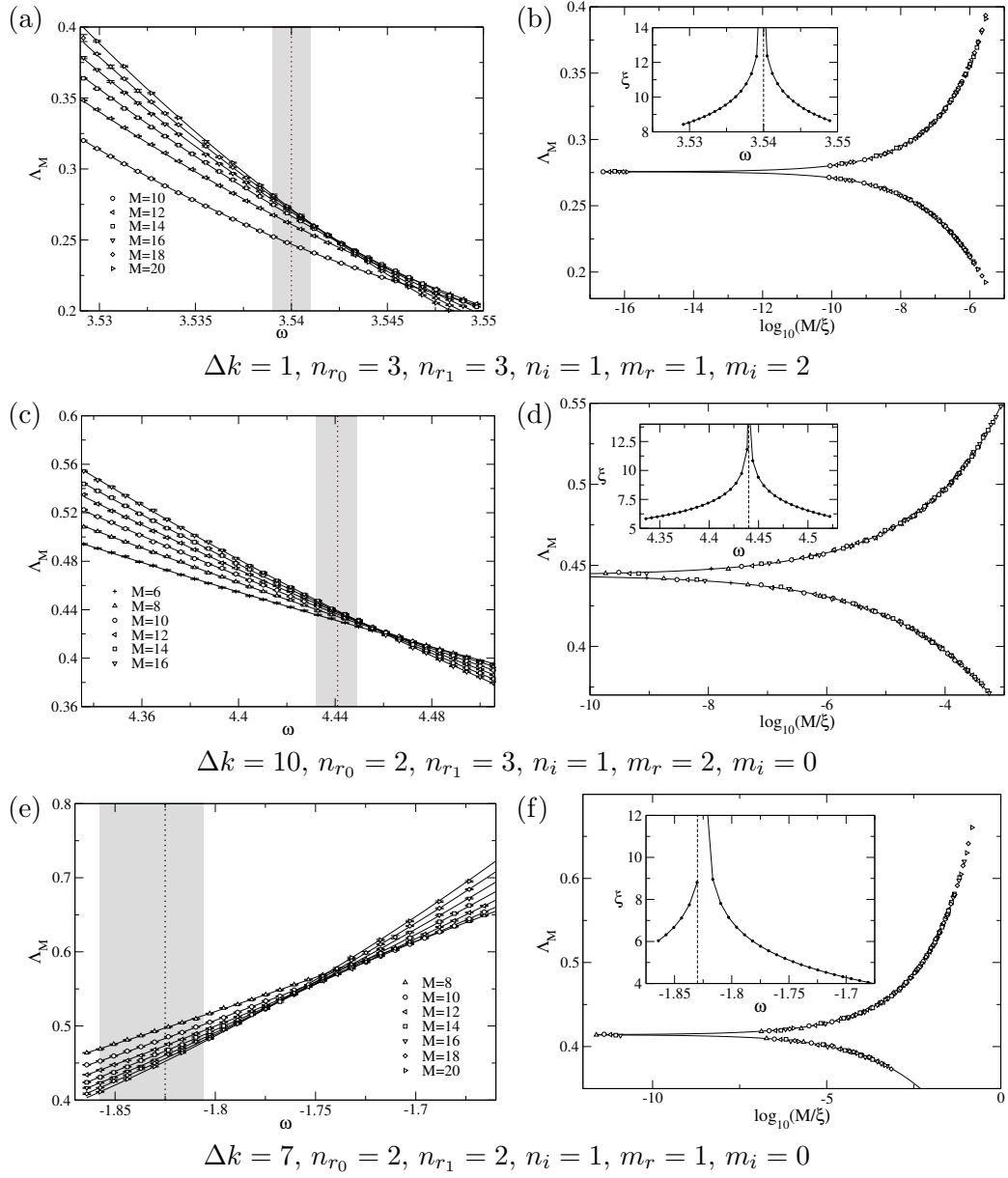


Figure 6.10: Similar to Fig. 6.9. Reduced localisation lengths $\Lambda_M(\omega)$ for box distributed uniform spring constant disorder widths $\Delta k = 1, 7$ and 10 . The left column (a,c,e) show the fits obtained from FSS, the orders of the expansion are given below each figure, while the right column (b,d,f) display the obtained scaling function when the irrelevant components have been subtracted. The insets show the correlation lengths.

Δm	M	ω	ω^2	n_{r0}	n_{r1}	n_i	m_r	m_i	ω_c	ω_c^2	ν	χ^2	μ	Γ_q
1.2	8-20		[12.15, 13.1]	2	3	1	2	0		$12.681^{+0.056}_{-0.034}$	$1.57^{+0.14}_{-0.09}$	165^{+38}_{-34}	165	0.84
4.0	8-20		[3.75, 4.25]	3	2	1	1	0		$4.134^{+0.024}_{-0.020}$	$1.57^{+0.06}_{-0.08}$	572^{+69}_{-64}	574	0.99
9.0	8-20		[-1.65, -1.5]	2	3	1	2	0		$-1.623^{+0.018}_{-0.037}$	$1.56^{+0.41}_{-0.18}$	154^{+37}_{-33}	154	0.87
1.2	8-20	[3.485, 3.62]		2	3	1	2	0	$3.561^{+0.008}_{-0.005}$		$1.57^{+0.15}_{-0.09}$	164^{+38}_{-34}	165	0.84
4.0	8-20	[1.936, 2.062]		3	2	1	1	0	$2.033^{+0.006}_{-0.005}$		$1.55^{+0.07}_{-0.08}$	573^{+65}_{-63}	573	0.99
9.0	8-20	[-1.284, -1.225]		2	3	1	1	0	$-1.273^{+0.006}_{-0.014}$		$1.56^{+0.44}_{-0.17}$	155^{+36}_{-33}	155	0.83
Δk	M	ω	ω^2	n_{r0}	n_{r1}	n_i	m_r	m_i	ω_c	ω_c^2	ν	χ^2	μ	Γ_q
1.0	10-20		[12.48, 12.6]	3	1	1	1	1		$12.527^{+0.003}_{-0.004}$	$1.58^{+0.05}_{-0.04}$	132^{+34}_{-30}	132	0.62
10.0	6-16		[18.8, 20.3]	1	3	1	2	0		$19.749^{+0.043}_{-0.038}$	$1.51^{+0.08}_{-0.08}$	176^{+36}_{-36}	176	0.84
7.0	8-20		[-3.5, -2.75]	2	2	1	1	0		$-3.325^{+0.070}_{-0.115}$	$1.59^{+0.23}_{-0.29}$	162^{+38}_{-33}	162	0.51
1.0	10-20	[3.529, 3.55]		3	3	1	1	2	$3.540^{+0.001}_{-0.001}$		$1.47^{+0.15}_{-0.05}$	157^{+39}_{-34}	156	0.49
10.0	6-16	[4.335, 4.506]		2	3	1	2	0	$4.441^{+0.008}_{-0.009}$		$1.52^{+0.15}_{-0.53}$	199^{+41}_{-38}	199	0.87
7.0	8-20	[-1.87, -1.66]		2	2	1	1	0	$-1.825^{+0.019}_{-0.033}$		$1.60^{+0.21}_{-0.19}$	162^{+38}_{-34}	162	0.79

Table 6.1: Values of critical parameters ω_c or ω_c^2 and ν for pure mass (top) and pure spring constant (bottom) disorder computed from FSS obtained with given M , ω , ω^2 ranges and with the orders of the expansion (6.20) given by n_{r0} , n_{r1} , n_i , m_r and m_i . The minimised χ^2 value, the degrees of freedom μ and the resulting goodness-of-fit parameter Γ_q are also shown for each fit. The errors correspond to non-symmetric 95% confidence intervals. More extensive tables with all stability check expansions are given in Appx. A.

average (see Appx. B) of the critical exponents. The errors for the mass disordered case are larger in the complex frequency regime, yet all critical exponents are within error of the weighted average. In the spring constant disorder case there is much higher discrepancy as some critical exponents fall outside of the error of the weighted average and may mean that the critical parameters are not accurately estimated.

Highly accurate numerical studies of the AM for electron localisation have found the critical exponent $\nu \equiv 1.5 \pm 0.1$ [37,132,138,142] for uniform box distributed disorder applied to the potential at lattice sites. In a phonon model, Akita and Ohtsuki [90] previously found a critical exponent of $\nu \approx 1.2 \pm 0.2$ with 2% accuracy TMM data for spring constant disorder $\Delta k = 1.8$. Recently Monthus and Garel [143], assuming that $\nu = 1.57$, showed that their PR data for high disorder at an LDT collapsed fairly well onto a scaling function. The weighted average of the critical exponent for the six chosen disorders is found to be $\nu = 1.550^{+0.020}_{-0.017}$ and therefore we assume that the phonon model is of the same orthogonal universality class as the AM.

6.4 Phase Diagrams

We plot the initial estimates of the critical frequencies discussed in Sec. 6.3 in the phase diagrams of Figs. 6.12 and 6.13. As we can see, for the pure mass disorder case, Fig. 6.12 very well reproduces the estimated phase diagram obtained by the

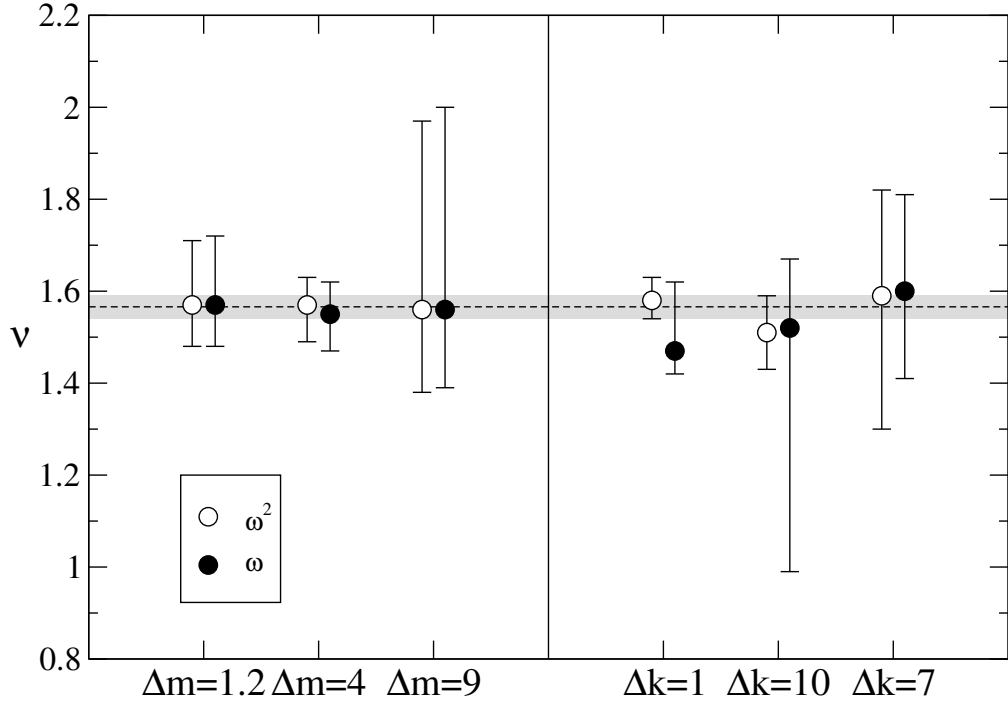


Figure 6.11: Critical exponents ν obtained from FSS of the 6 representative LDTs for both frequency ω and squared frequency ω^2 scaling. Dashed line is the weighted average (Appx. B) of all critical exponents and the weighted unsymmetric error is shaded grey.

relation Eqn. (6.4) with the electronic phase diagram in the AM as discussed in Sec. 6.2. The ω_c^2 values obtained from FSS have also been indicated in the phase diagrams. We see that the critical parameter found for the transition frequency ω_c^2 in the thermodynamic limit via FSS vary little from that of the transition frequency estimates using system size crossing points.

The positions of the states in Figs. 5.2(a)-(c) and 5.3(a)-(c) are labelled on the phase diagrams in Figs. 6.12 and 6.13 as the symbols (a)-(c) for mass and spring constant disorder, respectively. We see that the initial assumptions that localisation occurs in disordered phonon systems based on visualising the normal modes are in fact acceptable.

In line with the previously known phase diagrams [81, 124] for phonons in a face-centred cubic lattice we additionally include the positions of the peak in the reduced VDOS from Chap. 5 in both mass and spring constant disorder phase diagrams.

For the pure spring constant disorder, the phase diagram seems less surpris-

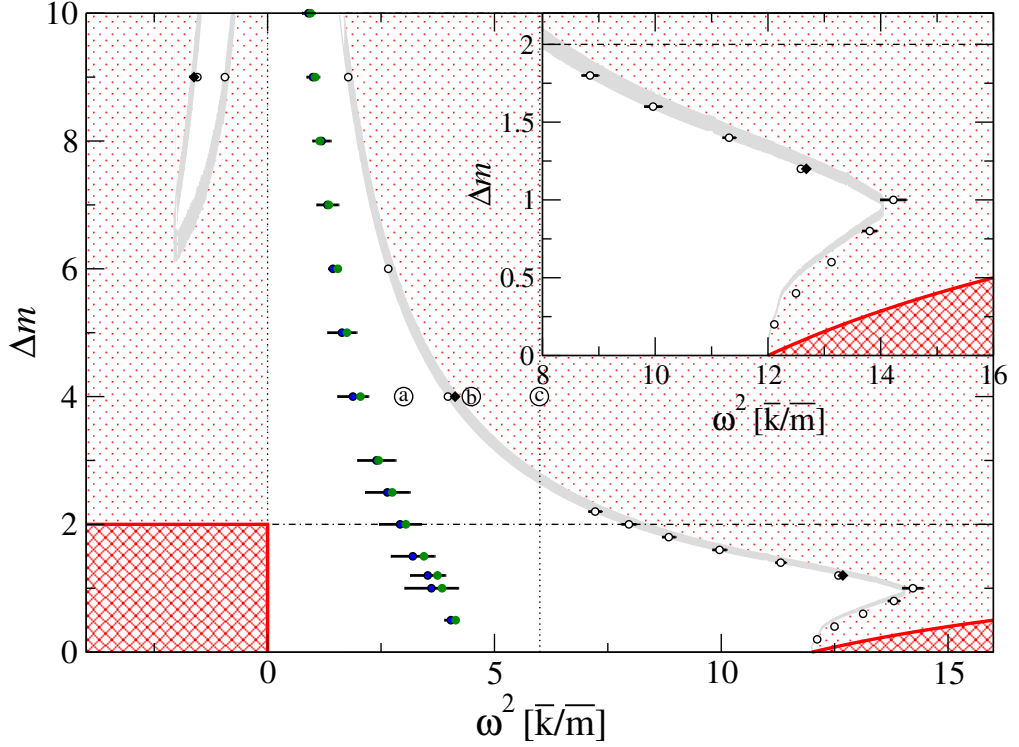


Figure 6.12: Mass disorder phase diagram (Δm vs. ω^2) for box distribution disorder applied to the masses at sites in a simple cubic lattice. Grey shading is the critical region obtained from the transformation from the electronic phase diagram in Ref. [25]. Red dotted regions are of localised states, red cross hatched regions enclosed by a red line (band edges) are inaccessible. Black diamonds and white circles are the finite size scaled transitions and estimated transitions, respectively. Green circles and blue circles are BP positions determined by the CPA and numerical diagonalisation respectively. Inset is the region of realistically attainable disorder. Labels (a)–(c) show the positions of the states in Fig. 5.2.

ing than in the mass disorder case. We see that in the region $0 \leq \omega^2 < 12$, all states remain extended up to the largest considered disorder $\Delta k = 10$. This is similar to the electronic case with pure hopping disorder [26, 144, 145], where even very strong hopping disorder does not lead to complete localisation close to $E = 0$. For completeness we show the electronic phase diagram for uniform box distributed disorder applied to the hopping integrals of electrons in Fig. 6.14. We remark that the analogous phonon disorder (namely in the spring constants) has a phase boundary that isn't continuous and therefore similarly does not experience an analogous MIT. Like the potential disordered phase diagram (Fig. 6.1) the hopping disorder diagram is symmetric around $E = 0$. There are definite similarities between the phase diagrams

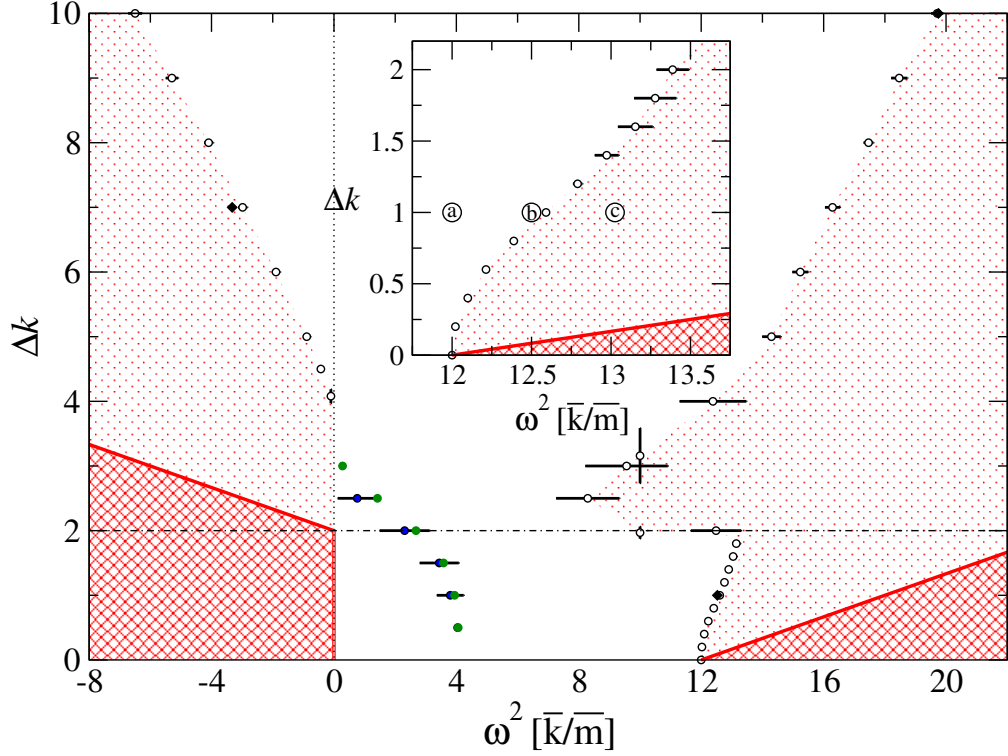


Figure 6.13: Spring constant disorder phase diagram (Δk vs. ω^2) for box distribution disorder applied to the spring constant between sites in a simple cubic lattice. All data points and shadings as Fig. 6.12. Labels (a)–(c) show the positions of the states in Fig. 5.3.

which indicates the possibility to mathematically transform between the two.

We see in Figs. 6.12 and 6.13 that for both mass and spring constant disorder no phase boundaries cross $\omega^2 = 0$, therefore the $\omega^2 = 0$ ‘Goldstone’ mode [79–82] remains extended throughout the phase diagrams up until the maximum disorder strengths that have been numerically investigated. We also note the $1/\omega^2$ dependance of the transformation for the mass disorder phase boundary from Sec. 6.1. This dependance indicates that for a mass disordered system, an infinite disorder strength is required to localise the zero-frequency mode. This is in agreement with previous studies in 1D and 2D systems.

What is also common to the TMM result for both mass and spring constant disorder is the observation of strong shifts of the crossing points of Λ_M when changing M . This is indicated by the relatively large error in estimated critical transitions in the phase diagram, as the estimates have been made with modest system sizes. Such a behaviour is to be expected, however, since we are effectively dealing with

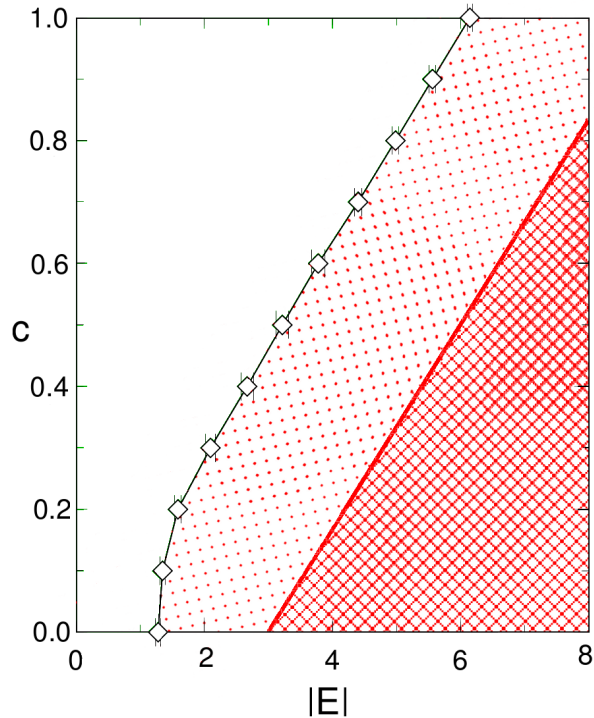


Figure 6.14: Electronic hopping disorder phase diagram (c vs. $|E|$) for a box distribution disorder of width c applied to the hopping integrals at sites in a simple cubic lattice and obtained using the TMM with 1% accuracy. Shadings are the same as in Fig. 6.12. Adapted from Ref. [26].

transition regions in the vicinity of the tails of the VDOS and hence the systematic size changes are also strongly influenced by changes in the VDOS. This is again similar to the situation for the electronic case where the transition at the mobility edges for $E \neq 0$ is also more difficult to study [132, 133, 146]. We note that the shifts are stronger for spring constant disorder of $\Delta k > 2$ where negative spring constants begin to be introduced into the system. We therefore go on to investigate the possible contributing factors for the enlarged error.

6.4.1 Truncated Spring Distribution Phase Diagram

We recall that the transfer matrices \mathbf{T}_n in Eqn. (6.10) contain terms that include a multiplication by the reciprocal of the spring constants connecting the current layer to the next. When we include disorder of $\Delta k \gtrsim 2$ it is likely that the spring constant will on occasions be approximately zero. The probability of such an occurrence is highest around $\Delta k \approx 2$ and slowly drops off as Δk increases and the disorder

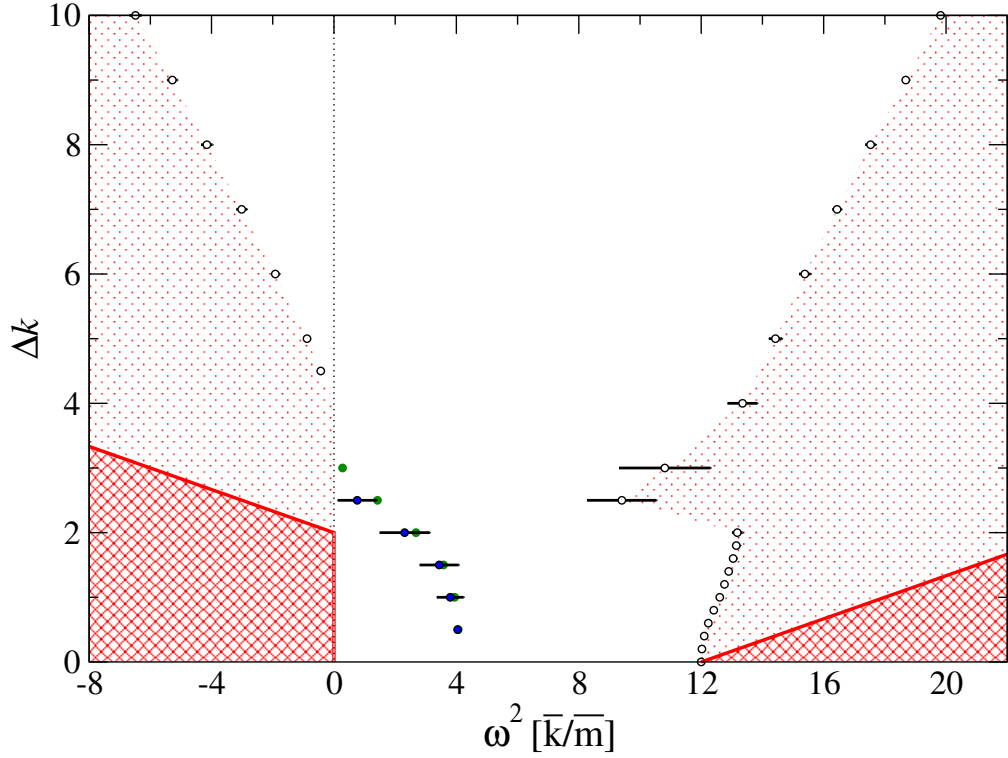


Figure 6.15: Spring disorder phase diagram (Δk vs. ω^2) for a truncated box distribution disorder $|k| > 10^{-4}$ applied to the springs at sites in a simple cubic lattice. All data points and shadings as Fig. 6.12.

distribution widens. In such an event, the new amplitude of the site connected to a spring of minimal stiffness will ‘blow up’, dwarfing the surrounding amplitudes. This could manifest itself as a reset of the whole computation when the amplitude vectors are reorthogonalised, as the computation is generally started with an orthogonal set of initial excitations in the form of an identity matrix. These effects may be a contributing factor for the change in direction of the phase boundary for spring disorder for positive frequencies at $\Delta k = 2$ in Fig. 6.13. We therefore recalculate all reduced localisation lengths for all previous disorders where $\Delta k \geq 2$ and restrict the distribution so that $|k| > 10^{-4}$ for all interlayer springs. We re-estimate the critical transition frequencies using the previously described methods and find that the phase diagram with the truncated distribution is the same as before within error (see Figs. 6.15 and 6.13 for truncated and original distributions, respectively). Therefore we can exclude that the change of direction of the phase boundary at $\Delta k = 2$ is due to the inclusion of spring constants $|k| < 10^{-4}$ in the disorder distribution.

We further investigate the directional changes of the phase boundary at $\Delta k = 2$ in the original spring disordered phase diagram (Fig. 6.13) by calculating reduced localisation lengths whilst sweeping across the disorder distribution width Δk rather than the frequency ω^2 . This will cut across the cleft of localised states from top to bottom rather than left to right in the phase diagram. We do this for a fixed $\omega^2 = 10$ and find two LDTs from extended to localised and back to extended states, with which we estimate the critical transitions in the same manner as before. The two points are plotted on Fig. 6.13 and complement the existing transitions found when sweeping across the frequency domain.

Chapter 7

Three Dimensional Vibrational Eigenstate Statistics

In the present chapter we will use random matrix theory (RMT) to describe the statistics of vibrational displacement fluctuations [147,148] in our disordered systems for states throughout the phase diagram. In the universal regime of mostly weak disorder, RMT can classify these fluctuations into universality classes such as the PTD [149] of the GOE [150]. Upon increasing the disorder, corrections to the GOE have been studied for electronic disordered system [151,152] which we also expect to see present in the disordered vibrational systems. We pay particular attention to the statistical fluctuations within vibrational eigenstates in the vicinity of the BP and the LDT. In the past, the BP has been conjectured to indicate the crossover of numerous phonon transport regimes [115]; we expect, if this is the case, that the fluctuations will behave anomalously in the vicinity of the BP. Thus far we have only qualitatively studied the vibrational eigenstates near the BP by visualising normal modes in Sec. 5.5 and as the appearance of the states appears to change as a consequence of the location of the BP, further quantitative analysis is required.

7.1 Random Matrix Theory

The RMT was first formulated by Wigner to describe resonances in compound nuclear reactions [153]. In order to model the excitation spectra of a complex nuclei, Wigner replaced a complicated and unknown Hamiltonian with a large random matrix and subsequently brought about the beginnings of RMT [154]. Dyson further developed the theory by introducing the GOE ($\beta = 1$) and the Gaussian unitary ensemble ($\beta = 2$) that describe systems with and without time reversal symmetry,

respectively [150].

RMT can be used to investigate both level spacing statistics and vibrational eigenstate fluctuations [154]. We choose to solely study the eigenstate fluctuations, the reason being two-fold; firstly level spacing statistics have already been explored to a great extent [155]. Their use on the same model system as this study confirmed that the BP does not mark the onset of the LDT [72]. Secondly, the study of level spacing statistics requires *all* eigenvalues. Eigenstate statistics requires only individual eigenstates at particular frequency values. We can therefore use sparse matrix diagonalisation methods to study substantially larger system sizes of $L^3 = 70^3$.

We determine the distribution function [152, 155]

$$f_\beta(\omega^2; v) = \frac{\Delta}{L^3} \left\langle \sum_j \delta(v - |u_j(n)|^2 L^3) \delta(\omega^2 - \omega_n^2) \right\rangle, \quad (7.1)$$

where Δ is the mean eigenvalue, $\langle \rangle$ denotes an average over disorder realisations and the vibrational eigenvectors are normalised so that $\langle |u_j(n)|^2 \rangle = L^{-3}$. For all disorders mentioned in Sec. 5.3 we calculate $f_\beta(v)$ for frequencies throughout the phase diagram at intervals of $\delta\omega^2 = 0.5$. Examples of the distributions obtained using 1,715,000 displacements are given in Figs. 7.1(a) and 7.2(a) for disorders $\Delta m = 1$ and $\Delta k = 1$, respectively.

7.1.1 The Porter-Thomas Distribution

In order to characterise the eigenstates, we compare the computed distribution with other well known distributions for frequencies $\omega^2 > 0$. Disorder has little/no effect on the zero-frequency modes. Hence the distribution (7.1) of a perfectly ordered system is a delta function centred around the normalised average displacement $\langle |U_j(\mathbf{r})|^2 \rangle_W = V^{-1}$, and is omitted from any plots.

We include the analytical solution to (7.1) that describes the local distribution of a classically chaotic system known as the PTD and given as

$$f_1^{(0)}(v) = \exp(-v/2)/\sqrt{2\pi v}. \quad (7.2)$$

The PTD was derived by Porter and Thomas [156] by assuming that the co-ordinate representation eigenstate in a disordered system is a Gaussian random variable. It is a special solution of the GOE. We see that for mass disorder $\Delta m = 1$ in Fig. 7.1(a) the distribution curves increasingly depart from the PTD with increasing frequency. A greater departure for the $\omega^2 = 15$ distribution is observed. This is

expected as $\omega^2 = 15$ is in the localised regime as for this disorder $\Delta m = 1$ the LDT is at $\omega^2 \approx 14$ (See Fig. 6.12). For spring constant disorder $\Delta k = 1$ in Fig. 7.2(a) the nature of the departure of the distribution curves from PTD is very different. For low frequencies the distributions remain close to the PTD, only when the LDT ($\omega^2 \approx 12.5$) is crossed with frequency $\omega^2 = 13$ there is an abrupt departure from the PTD. Comparison of the behaviour of the distributions at frequencies less than the LDT for disorders $\Delta m = 1$ and $\Delta k = 1$ may indicate that spring constant disorder has lesser effect on the vibrational eigenstates at low frequencies.

We characterise the deviation from the expected PTD behaviour with the difference function δf_β between $f_\beta(v)$ and $f_1^{(0)}$ as [152]

$$\delta f_\beta = \frac{f_\beta(\omega, \mathbf{r}; v)}{f_1^{(0)}} - 1. \quad (7.3)$$

We plot the difference function for frequencies near the BP in Figs. 7.1(b) and 7.2(b) for mass and spring constant disorder, respectively. We include the analytical estimate of departure from PTD as derived for the AM [151]

$$\delta f_\beta \simeq P \left(\frac{3}{4} - \frac{3v}{2} + \frac{v^2}{4} \right), \quad (7.4)$$

where P is a constant relating to the diffusion in the system and in the electronic case is known as the one-dimensional diffusion propagator [152].

We see that for small frequencies the analytical estimate is very well suited to our data. We show that for the mass disordered case (Fig. 7.1(b)) a value of $P_1 = 0.0545$ has a good fit for δf_β of $\omega^2 = 2$ and similarly $P_1 = 0.0315$ has a good fit for δf_β of $\omega^2 = 2.5$ in the spring constant disorder case (Fig. 7.2(b)). For higher frequencies this fit continues in the spring constant disorder case, where for a value of $P_2 = 0.0545$ we have a good agreement for δf_β at $\omega^2 = 6$. This is not the case for mass disorder where the minimum values of δf_β shift from $v = 3$ and to illustrate we show that for $P_2 = 0.195$ the difference δf_β fits the $\omega^2 = 3.5$ results only for small v but deviates for increasing v . Therefore for spring constant disorder we see that the deviations from PTD are standard in form, fitting Eqn. (7.4). For mass disorder, we leave the PTD regime fully before reaching localisation, where the analytical form of the intermediate distribution is not yet known.

7.1.2 Maximally Localised Distribution

We look for an analytical approximation for the distribution of vibrational displacements for eigenstates in the localised regime. We assume that for phonon frequencies

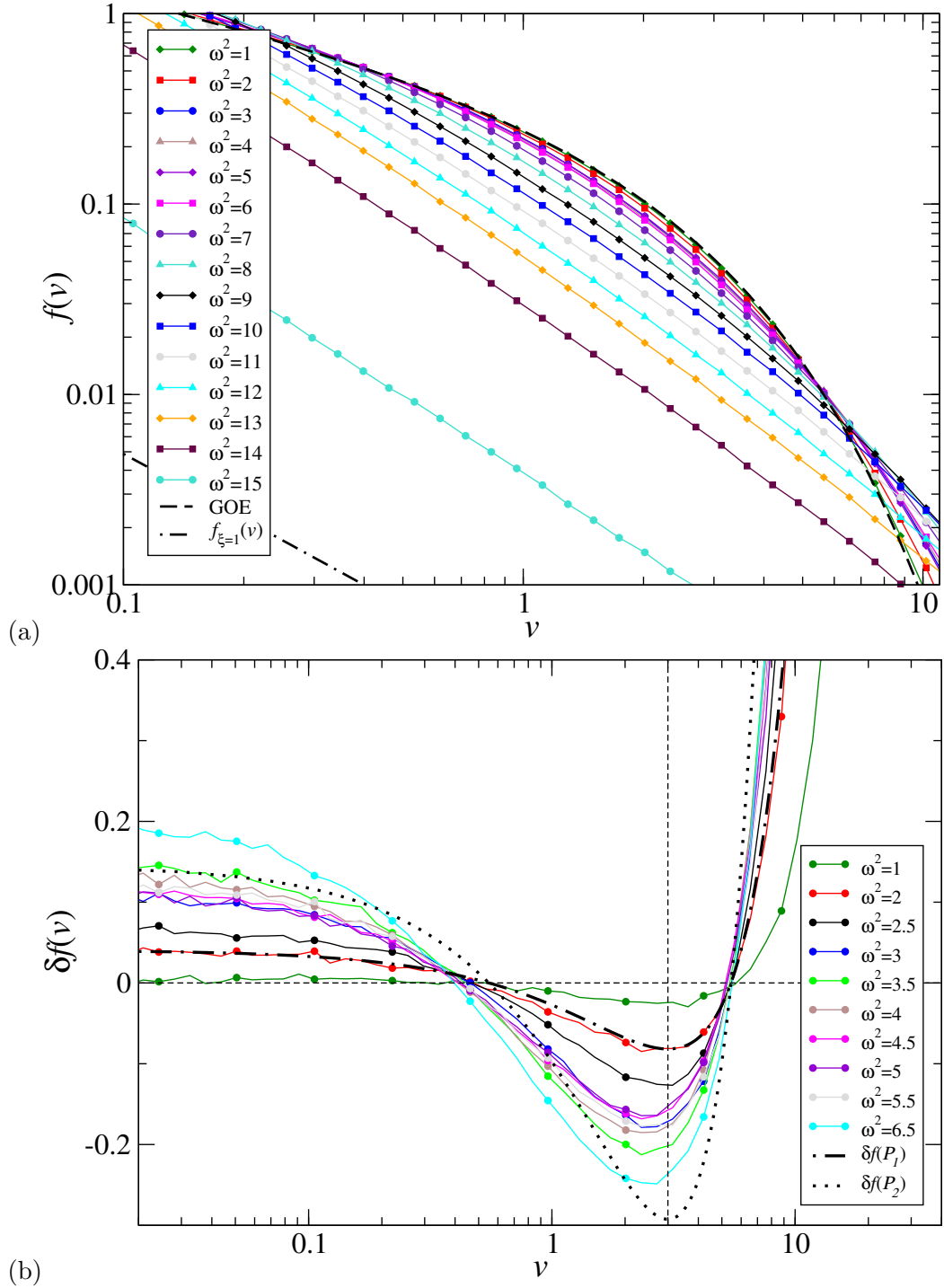


Figure 7.1: Fluctuation distributions for disorder $\Delta m = 1$ (a) $f_\beta(\omega^2, \mathbf{r}; t)$ and a range of frequencies as labelled in the figure with GOE as a dashed line and (b) δf_β for a range of frequencies. GOE here is the $\delta f_\beta = 0$ line, the $\nu = 3$ line is the theoretical minimum of the analytical δf_β . $P_1 = 0.0545$ and $P_2 = 0.195$ are used to fit the theoretical deviation from PTD.

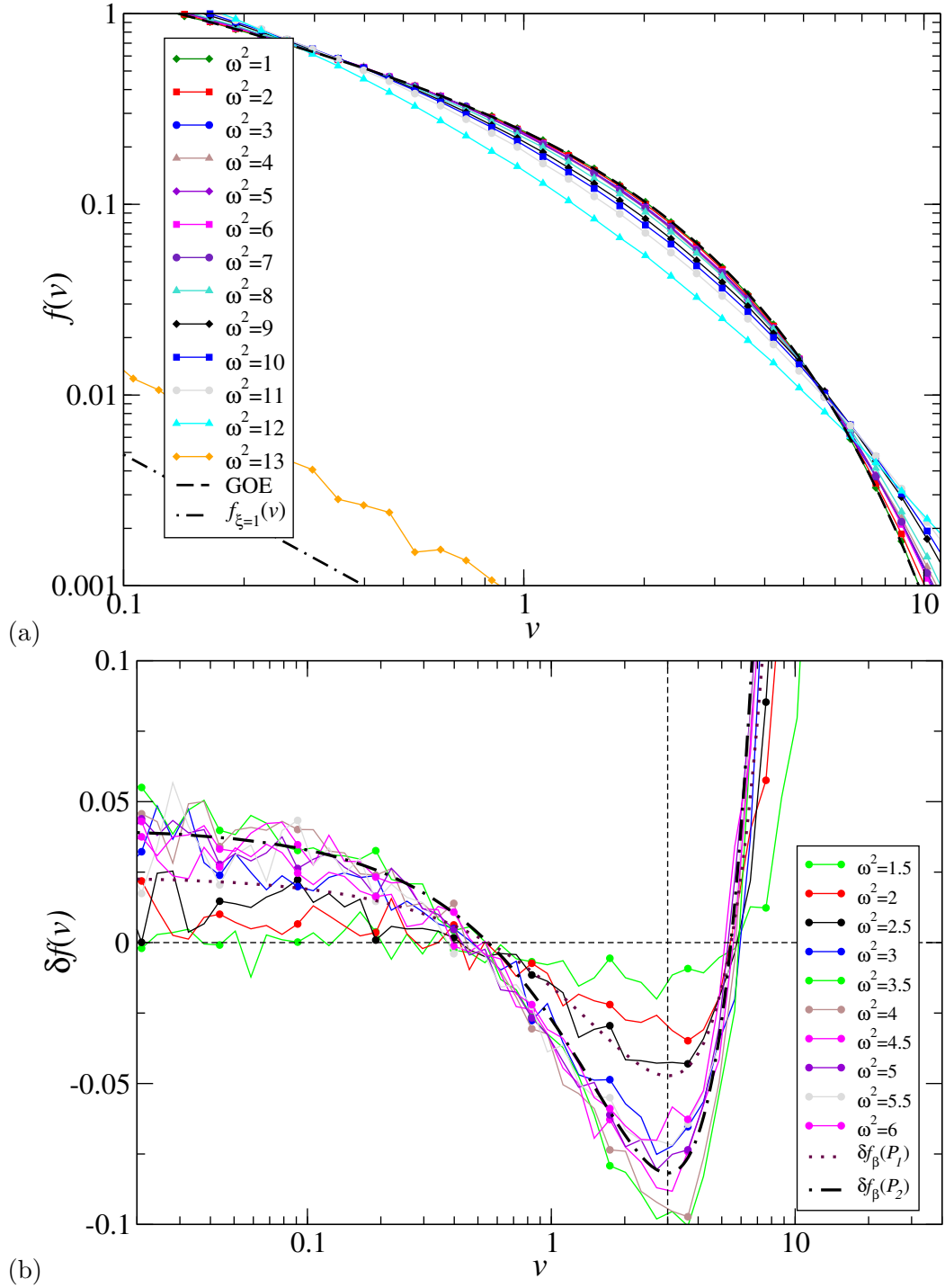


Figure 7.2: Fluctuation distributions for disorder $\Delta k = 1$ (a) $f_\beta(\omega^2, \mathbf{r}; t)$ and a range of frequencies as labelled in the figure with GOE as a dashed line and (b) δf_β for a range of frequencies. GOE here is the $\delta f_\beta = 0$ line, the $\nu = 3$ line is the theoretical minimum of the analytical δf_β . $P_1 = 0.0315$ and $P_2 = 0.0545$ are used to fit the theoretical deviation from PTD.

$\omega^2 > \omega_c^2$, the vibrational states are exponentially localised. This in turn invokes the typical picture that the vibrational displacements decay exponentially from the maximum displacement centred somewhere within the box, where the system size of the box $L > \xi$. The analytical expression of such a localised state can be more readily derived in a spherical system and as such the distribution becomes [155]

$$f_\xi(v) = \frac{4\pi}{V} \int_0^{\frac{L}{2}} dr r^2 \delta(v - |U_j(r)|^2 V) = \frac{\pi \xi^3}{4Vv} \ln^2 \left(\frac{c^2 V}{v} \right), \quad (7.5)$$

where c^2 is a normalisation constant of the form [155]

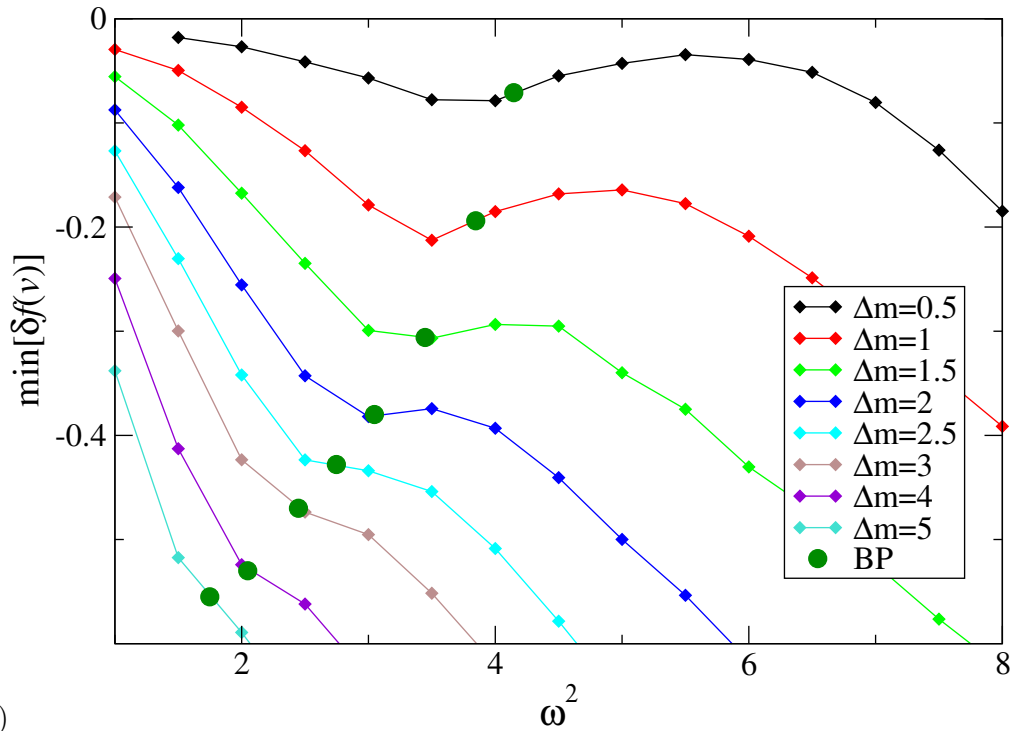
$$c^2 = \frac{2}{\pi \xi^3} \left[1 - \left(1 + \frac{L}{\xi} + \frac{L^2}{2\xi^2} \right) e^{-\frac{L}{\xi}} \right]^{-1}. \quad (7.6)$$

Due to the localised nature of the state and the isotropy of the disorder, it is acceptable to make the simplification of a spherical system. The integration in Eqn. (7.5) is over the radius r of the system, but beyond the vibrational displacements of the localised excitation, all vibrational displacements (in the cubic system) can be safely assumed to be zero. We use a correlation/localisation length of $\xi = 1$ for the theoretical maximally localised state $f_{\xi=1}(v)$ and plot the associated distribution in Figs. 7.1(a) and 7.2(a) (as dot-dashed lines). We can see in both figures that for frequencies $\omega^2 > \omega_c^2$ the vibrational eigenstate distributions approach the maximally localised distribution as frequency is increased and, crucially, do not exceed it.

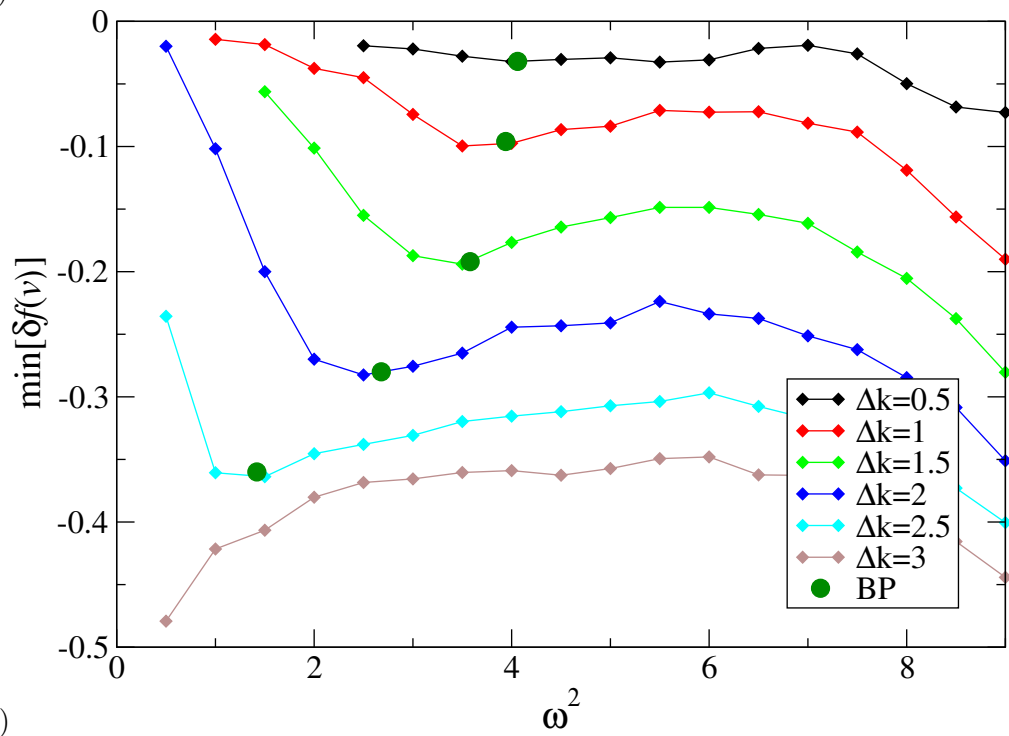
7.1.3 Deviations and the Boson Peak

In the plots of deviations from the PTD (Figs. 7.2(b) and 7.2(b)) for frequencies near the BP, we see that upon further increasing ω^2 , there is again a region where the agreement with $f_1^{(0)}$ becomes better. This behaviour has not previously been observed (neither in the electronic case nor in calculations on vibrational eigenstates).

We use the position ω^2 of the minimum of the deviation function $\min[\delta f(\nu)]$ as an indicator of the level of deviation. This is acceptable only for small frequencies where the deviations of both disorders Δk and Δm follow the form in Eqn. (7.4). We note that in this case, $\min[\delta f(\nu)]$ is proportional to the so called diffusion constant P as the minima occur at $\nu = 3$. We plot the minima $\min[\delta f(\nu)]$ as a function of ω^2 for different disorders in Fig. 7.3 and indicate the position of the BP frequency ω_{BP}^2 as solid green circles. We see that for both mass and spring constant disorder there is either a dip or shoulder in $\min[\delta f(\nu)]$ (and P) that coincides with ω_{BP}^2 . Note that in the spring constant disordered case, when $\Delta k = 3$ there is no BP and similarly



(a)



(b)

Figure 7.3: For disorders (a) $\Delta m = 1$ and (b) $\Delta k = 1$, $\min[\delta f(v)]$ as a function of frequencies ω^2 for disorders as indicated in the legends, primarily around the BP frequency ω_{BP}^2 .

no dip in $\min[\delta f(\nu)]$.

Both the disorder-modified plane waves ($\omega < \omega_{\text{BP}}$) as well as the random-matrix states ($\omega > \omega_{\text{BP}}$) obey the GOE statistics rather well, whereas the states at the cross-over (i.e. the states with $\omega \approx \omega_{\text{BP}}$) have a maximum deviation from the PTD. This indicates some significance of the position of the BP and may be the cross-over of vibrational states between Debye-like waves and random-matrix type eigenstates [72].

Chapter 8

Three Dimensional Participation Ratios and Multifractal Analysis

In this chapter we will initially study the character of the vibrational eigenstates throughout the phase diagram with PRs. The PR is a measure which is regarded as an estimation of the extension of a vibrational eigenstate and often used to investigate LDTs. It has been applied to both electronic wave function amplitudes and amplitudes of classical waves in crystalline systems for many years with mixed success [143].

We will define the gIPR by extending the concept of PR to higher moments of the intensity. In the latter parts of this chapter we will exploit the gIPR to investigate the fine structure of normal modes populating the phase boundaries and perform a numerical multi-fractal analysis (MFA) to obtain the singularity spectrum at the critical transition frequencies of mass and spring constant disorders $\Delta m = 1.2$, $\Delta k = 1$ and $\Delta k = 10$. The obtained phonon singularity spectra are compared to the electronic multifractal spectrum obtained for the MIT in Ref. [157] to identify whether both models exhibit the same critical properties.

8.1 Participation Ratios

The PR¹ is a measure of the involvement of the system in the particular eigenstate n of vibration, and can be useful in determining the location of an LDT of the

¹The PR has already been widely used for analysis of 1D systems in Chap. 4. Here we present a more comprehensive introduction to the measure.

excitation. The PRs $P_L(n)$ of a cube of sites with system size L is often given as [67]

$$P_L(n) = \frac{\left[\sum_{j=1}^{L^d} u_j^2(n) \right]^2}{L^d \sum_{j=1}^{L^d} u_j^4(n)}, \quad (8.1)$$

where $u_j(n)$ is a single site amplitude within a particular mode at lattice site j and d is the dimension of the system. We emphasise that the normalisation of the vibration, automatically observed for electronic eigenstates by the Born rule, is $\sum_j u_j^2(n) = 1$ for consistency when comparing different eigenstates. As the normalisation is already enforced we use the general form of the PR given as

$$P_L(n) = L^{-d} \left(\sum_{j=1}^{L^d} u_j^4(n) \right)^{-1}. \quad (8.2)$$

For a fully extended vibration where the total amplitude within the system is evenly distributed across all sites, such that $u_j^2 \sim L^{-d}$ we find

$$P_L(n) = L^{-d} \left(\sum_{j=1}^{L^d} L^{-2d} \right)^{-1} = L^{-d} (L^{-d})^{-1} = 1 \quad (8.3)$$

so that P_L for a fully extended mode is unity. On the other hand for a maximally localised state, the total amplitude in the system is centred on a single site say, $j = 1$, such that

$$u_j(n) = \begin{cases} 1, & \text{if } j = 1, \\ 0, & \text{otherwise.} \end{cases} \quad (8.4)$$

Therefore in the fully localised regime the PR is given as

$$P_L(n) = L^{-d} \left(\sum_{j=1}^{L^d} \delta_{j,1} \right)^{-1} = L^{-d} \quad (8.5)$$

so that a perfectly localised vibration corresponds to $P_L(n) = 0$ in the limit $L \rightarrow \infty$. We therefore see from Eqn. (8.5) that in the localised regime the PR decreases with system size L and for the extended regime in Eqn. (8.3), the PR increases with L until the PR saturate and occupies the whole system leading to $P_L = 1$. We expect an intermediate regime that is independent of L and manifests itself as the crossing of PR results for different system sizes. This indicates a possible LDT.

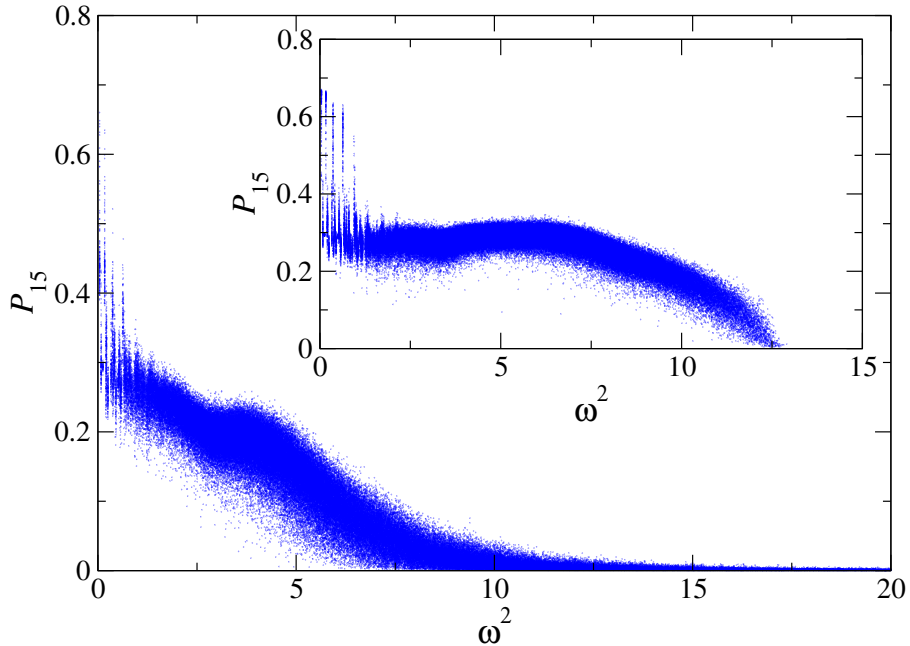


Figure 8.1: Scatter plot of PR (P_{15}) versus squared frequency ω^2 for all normal modes in a cubic system of length $L^3 = 15^3$ for 50 disorder realisations of uniform box distributed mass $\Delta m = 1.5$ and inset spring constant $\Delta k = 1$ disorders. Note that for all $\omega^2 = 0$ modes $P_{15} = 1$. We terminate the PR axis at 0.8 to simplify the appearance.

8.1.1 Typical Participation Ratio Data

To obtain the PRs we perform a dense matrix diagonalisation of the dynamical matrices as described in Sec. 3.1 and keep all vibrational eigenstates for the whole frequency spectrum. We present some typical PR results in a system of size $L^3 = 15^3$ for 50 disorder realisations of typical disorders $\Delta m = 1.5$ and $\Delta k = 1$ in Fig. 8.1. Although a general trend is apparent, this figure demonstrates the difficulty of working with PRs. The results can dramatically change from one realisation to the next for the same disorder magnitude. Not only do the calculated PRs vary between disorder realisations but so do the obtained frequencies. This results in the overlapping of frequency values from different disorder realisations observed in the scatter plots of Fig. 8.1. We note that at low frequencies there are defined vertical lines formed from similar frequencies and varying participation across disorder realisations. This indicates that disorder has a lesser effect at low frequencies as the disorder has not shifted the eigenvalues to different frequencies.

8.1.2 Average Participation Ratio for Constant System Size

We plot the average PR spectrum as a function of frequency squared and disorder magnitude for both mass and spring constant type disorder in Fig. 8.2. We note that even extended modes with $\omega^2 < 0$ have a non-zero PR for both mass and spring constant disorder.

We have plotted the trajectories of the BP in the base of Figs. 8.2(a) and (b) and within the disorder planes we link the level of the average PR to the position of the BP. We see at these positions either a slight plateau or kink in the PR level that relates to the maximum deviation from the PTD in the vibrational eigenstate statistics in Sec. 7.1.3. The significance of the correspondence between lowering of participation in the PR spectrum, the deviation from PTD in the vibrational eigenstate statistics and the position of the BP will remain a topic for future investigation.

8.1.3 Localisation-Delocalisation Transition from Participation Ratios

To identify a LDT we require data for a range of system sizes. We calculate the PRs of system sizes $L^3 = 5^3, 10^3$ and 15^3 for 1360, 170 and 50 disorder realisations, so that we have 170,000, 170,000 and 168,750 modes for each system size/disorder combination, respectively, for statistical averaging. The eigenvalues (squared frequencies) obtained from diagonalisation vary between disorder realisations for the same disorder distribution. Therefore averaging of PRs for identical eigenvalues is not possible even though the PR of each individual normal mode is readily available. There are numerous averaging techniques available for this type of data. We use a running average over 100 frequency values and present the results in Fig. 8.3.

We note that there is no clear indication of the LDT transition in the plots of P_L in Fig. 8.3 as there is no simple crossing of PR data for system sizes $L^3 = 5^3, 10^3$ and 15^3 . In the spring constant disordered case where $\Delta k = 1$ we see that the running average does not reach the predicted position of the LDT from TMM and therefore we cannot draw any definite conclusion from this data. Monthus et al. [143] find the same behaviour in their low disorder results. We note that as system size is increased the running averages get closer to the previously determined critical transition frequency. This indicates that an increase in system size is necessary for this disorder magnitude. Instead, to obtain an LDT in their PR data, Monthus et al. increase the width of their disorder distribution. In the mass disorder case, we do not have an estimate of the transition frequency for the disorder $\Delta m = 1.5$ from

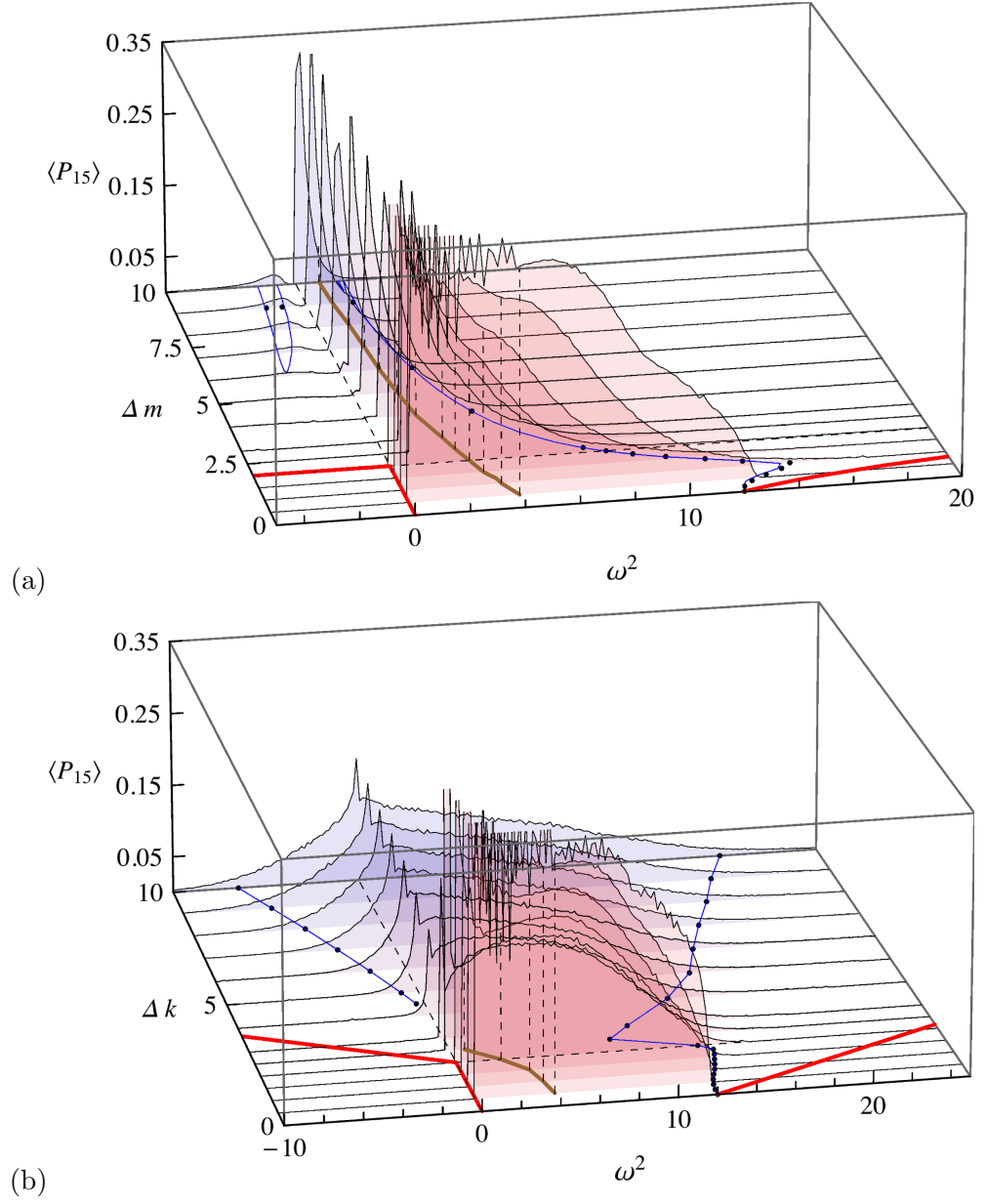


Figure 8.2: Average PRs $\langle P_{15} \rangle$ as a function of ω^2 for various (a) mass Δm and (b) spring constant Δk disorders averaged over 50 disorder realisations for a system of size $L^3 = 15^3$. The grey and red lines in the base denote the phase boundaries and the band edges respectively as in Figs. 6.12 and 6.13. The green and black dashed lines indicate the trajectory of the BP.

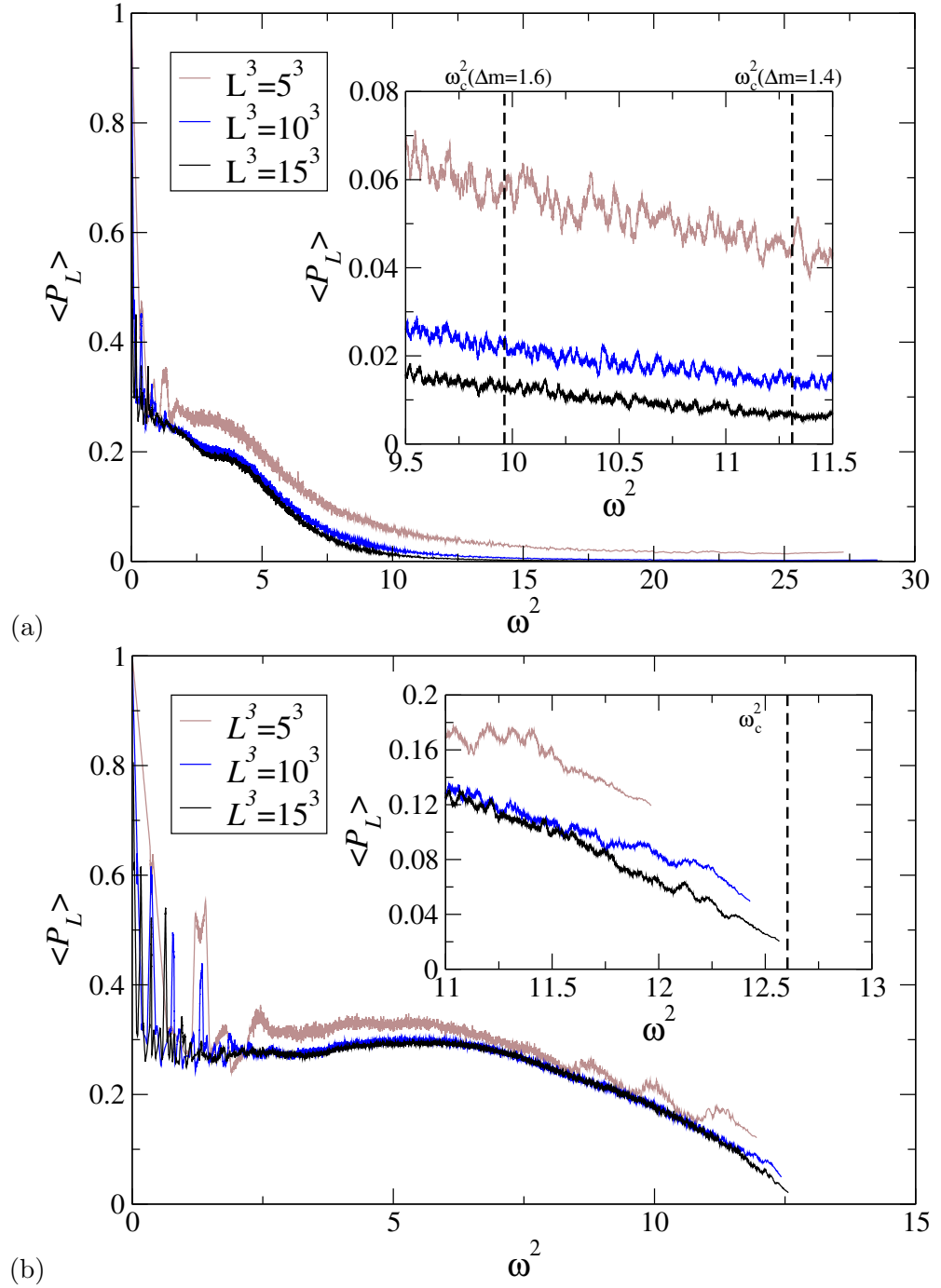


Figure 8.3: Running average with width 100 frequencies of PRs as a function of squared frequency ω^2 for uniform box distributed (a) mass $\Delta m = 1.5$ and (b) spring constant $\Delta k = 1$ disorders. Results are for system sizes $L^3 = 5^3$, 10^3 and 15^3 with 1360, 170 and 50 disorder realisations, resulting in 170,000, 170,000 and 168,750 states per disorder/system size combination, respectively. Insets are likely regions of transition.

TMM. We include in the running average PR plot, estimates of critical transition frequencies for disorders $\Delta m = 1.4$ and 1.6 as vertical dashed lines in the inset of Fig. 8.3. The transition frequency is expected to be between the included transitions, but there is no evidence for this whatsoever.

We attribute the missing transitions that have been previously obtained using TMM to the low DOS available for statistical averaging near the transitions. Increasing the system size would increase the available data for statistical averaging and should fulfil the requirement of being closer to the thermodynamic limit. We have seen the difficulty in working with PRs and the lack of the expected LDT in the PR spectrum due to the low DOS and moderate system sizes. From this data it is difficult to give an accurate conclusion whether or not the LDT exists.

8.2 Multifractal Analysis

The PRs for small L above are unable to support the findings of the LDT apparent in Chap. 6, we therefore require a more rigorous analysis of the nature of the states at the previously obtained LDTs. We continue to use the PR measure but we define an extension known as MFA of the gIPR with system size scaling [157]. With MFA we can probe the fine structure of the vibrational amplitudes in a box and for best results we must approach the thermodynamic limit and compute the largest possible vibrational eigenstates. It is well known that at a critical transition within a given universality class the eigenmodes of the respective eigensystems have universal characteristics [20, 158]. As such we expect the vibrational amplitudes at the critical transition to be of a multifractal nature in line with findings for electronic wave functions [93, 131, 157, 159].

8.2.1 Fractal Structures and Dimensions

Benoît Mandelbrot died on the 14th of October 2010. His death sparked a series of high profile media obituaries that labelled him the ‘father of fractals’.² He coined the term ‘fractal’ and introduced the concept of fractals and fractal dimensions in his seminal work in 1975 [160]. Mandelbrot described a fractal as “a rough or fragmented geometric shape that can be split into parts, each of which is (at least approximately) a reduced-size copy of the whole” [160]. Fractal structures come in two distinct categories, deterministic and random. The most commonly modelled

²Please see the following URLs for a small subset of articles: <http://www.independent.co.uk/news/science/father-of-fractals-dies-at-85-2109421.html>, http://www.theregister.co.uk/2010/10/18/mandelbrot_obituary/, <http://phys.org/news/2010-10-father-fractals.html>



Figure 8.4: Romanesco broccoli is a natural self-affine structure whose cross-section resembles the Koch curve, a fractal with fractal dimension $D_f = 1.2619$ [162].

random fractals in nature are rivers and coastlines, and require statistical treatment. Those that can be described with a more formal mathematical treatment are that of the deterministic category. In nature there are structures that resemble deterministic fractals, a well known example of this is the Romanesco broccoli pictured in Fig. 8.4. The Romanesco broccoli is not a fractal in the sense that its self-affine structure can only be magnified a finite number of times. Equally, all Romanesco broccoli would be identical if they were a true deterministic fractal. Nevertheless the straight line path of say an insect traversing the broccoli is a good representation of the Koch curve [161]. The Koch curve has a fractal dimension $D_f = 1.2619$ that is less than the Euclidean dimension $d = 2$ [160]. It is easier to describe a deterministic fractal and we give an example of the construction of the initial stages of the Mandelbrot-Given fractal in Fig. 8.5. We wish to formulate an equation for the dimension of the system based on the number of identical parts that make up a given system $N(a)$, and the size of these parts $\frac{1}{a}$. We start by defining a measure of volume in terms of the system size

$$N(a) = a^d, \quad (8.6)$$

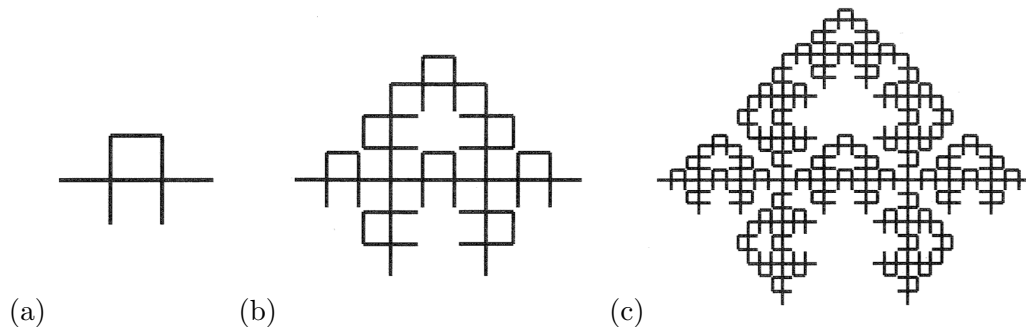


Figure 8.5: The construction of the Mandelbrot-Given fractal in the first stage where (a) is the initial structure made up of 8 distinct lines, (b) the next step by replacing each line with an exact copy of the original structure and (c) is constructed by replacing each line in (b) by an exact copy of (a) [163]. The process is repeated indefinitely to build a self-similar structure that is a fractal, such that when magnifying any section of the structure we arrive at a seemingly identical structure.

this can be re-arranged into a form to obtain the dimension of the system

$$d = \frac{\log N(a)}{\log a}. \quad (8.7)$$

This process is easiest to visualise by taking a simple example for 1, 2 and 3 Euclidean dimensions, these being a line, square and cube each with sides of unit length. Then along each dimension we split the object in half ($a = 2$), leaving 2, 4 and 8 identical pieces that made up the original line, square and cube, respectively. Substituting these values into Eqn. (8.7) we confirm the relationship and find the integer Euclidean dimensions of the original objects ($d = 1, 2$ and 3 , respectively).

We now extend the calculation to the Mandelbrot-Given fractal in Fig. 8.5. The fractal is made up of 8 parts each of which are of size $\frac{1}{3}$. We can see using Eqn. (8.7) that the dimensionality of this test system is not an integer, and therefore d becomes the more general D_f , known as the fractal dimension. We find

$$D_f = \log_3 8 = 1.892 \dots \quad (8.8)$$

and in general the fractal dimension D_f is less than that of the Euclidean dimension within which the fractal resides (in this case $d = 2$). Although this treatment does not work with random fractals, there are numerous methods that can be used to obtain the fractal dimension of random fractals, all of which are compatible with deterministic fractals and give identical fractal dimensions to the above treatment.

In most cases a single fractal dimension D_f is not enough to describe a com-

plex structure. It is common when analysing complex systems that the constituent parts (densities, flows, etc.) are distributed differently, each part with its own fractal dimension. Depending on the system there may be a spectrum comprising of infinitely many exponents (singularity spectrum) describing it. In order to characterise these more complex systems we introduce mass exponents and generalised dimensions in the following section.

8.2.2 Mass Exponents and Generalised Dimensions

In direct analogy to the Anderson MIT where one would typically study the intensities of the normalised electronic wave function amplitudes $|\Psi|^2$ [93], we study the normalised amplitudes of the normal modes of vibration at the LDT. We partition the box of amplitudes $u_n = u_1, u_2, \dots, u_N$ in a d -dimensional system of volume L^d equally into N_l boxes, each of volume l^3 . The summed amplitude of vibration in the k^{th} box is

$$\mu_k(l) = \sum_{n=1}^{l^d} |u_n|^2, \quad k = 1, \dots, N_l. \quad (8.9)$$

From the standard Born normalisation it follows $\sum_{k=1}^{N_l} \mu_k(l) = 1$. The q -th moment of the box probability in the system is defined as

$$R_q(l) = \sum_{k=1}^{N_l} \mu_k^q(l), \quad (8.10)$$

and is called the gIPR. We can see that in the limit where $l = 1$ and $q = 2$ we have the standard inverse participation ratio (IPR), with the exclusion of the normalisation term L^d , as discussed in Sec. 8.1. For varying q we have different moments of the intensities of vibrational amplitudes. The gIPR is often referred to as a q -microscope [163] that probes the fluctuations of $|u_n|^2$'s, where positive (negative) q 's enhance the contribution of large (small) $|u_n|^2$'s to the overall vibrational eigenstates.

Multifractality implies that within a range of values of the ratio $\lambda \equiv l/L$, the moments R_q exhibit a power-law dependance on λ , indicating the absence of length scales in the system [158] such that,

$$R_q(\lambda) \propto \lambda^{\tau(q)} \quad (8.11)$$

where $\tau(q)$ are the so called mass exponents and can be defined as

$$\tau(q) = \lim_{\lambda \rightarrow 0} \frac{\ln R_q(\lambda)}{\ln \lambda}. \quad (8.12)$$

In the thermodynamic limit ($\lambda \rightarrow 0$) we obtain the true value of the mass exponent τ_q at criticality. The limiting cases for the mass exponent are as follows

$$\tau(q) = \begin{cases} d(q-1) & \text{extended,} \\ D_q(q-1) & \text{criticality,} \\ 0 & \text{localised (for } q > 0), \end{cases} \quad (8.13)$$

for the appropriately labelled transport regimes. This can be seen when applying the appropriate limits to the vibrational amplitudes. When in an extended state the total available amplitude is uniformly distributed throughout the system, such that $u_n^2 \rightarrow L^{-d}$, and R_q is of the form $R_q = \lambda^{d(q-1)}$. Whereas in the strong disorder limit, where the total available amplitude is localised on a single site of the system $u_{n=n_0}^2 \rightarrow 1$, $R_q = 1$ for all positive q 's and therefore $\tau = 0$. It is also easy to see from Eqns. (8.10) and (8.11) that $\tau(0) = -d$ and due to the normalisation $\tau(1) = 0$.

An eigenstate is multifractal when $\tau(q)$ is nonlinear in q . The values of $\tau(q)$ transform to a set of generalised dimensions D_q that describe the multifractality of the system. Therefore, from Eqn. (8.12) we obtain the generalised fractal dimension as

$$D_q = \frac{1}{q-1} \lim_{\lambda \rightarrow 0} \frac{\ln R_q(\lambda)}{\ln \lambda} \quad (8.14)$$

and similarly to $\tau(q)$, the dependance of D_q on q is an indication of multifractality. D_0 is equal to the dimension of support of the measure.

8.2.3 The Singularity Spectrum

The singularity spectrum $f(\alpha)$ is the set of fractal dimensions that fully describe the statistical distribution of the vibrational amplitudes in the eigenstate at criticality. Given a system of size L^d partitioned into $k = (L/l)^d$ boxes of volume l^d , each box k has an associated summed amplitude of vibration μ_k as outlined by Eqn. (8.9). It is more convenient to work with a related variable α , defined as

$$\alpha \equiv \frac{\ln \mu}{\ln \lambda}, \quad (8.15)$$

giving a set of different exponents α . Now, the number of boxes N_α that have the same α scales as $N_\alpha \propto \lambda^{-f(\alpha)}$ with fractal dimension $f(\alpha)$. The multifractal vibrational eigenstate is completely defined by an infinite set of $f(\alpha)$ values known as the singularity spectrum [164].

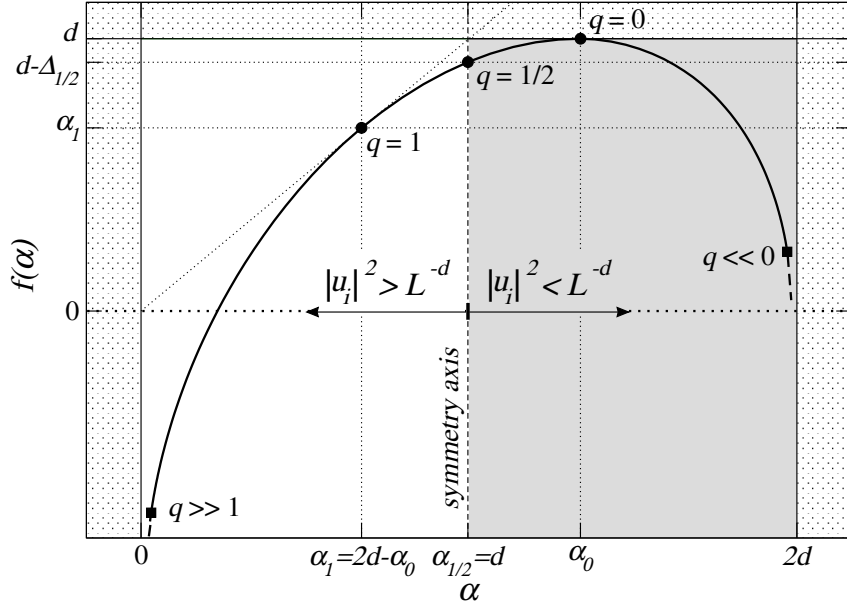


Figure 8.6: Schematic example of an $f(\alpha)$ spectrum where every point on the line is generated by the evaluation of a q -moment of the gIPR. The maximum is at $q = 0$ where $f(\alpha_0) = d$ and therefore anything greater than d is inaccessible signified by the dotted region. At $q = 1$, $f(\alpha_1) = \alpha_1$ and $f'(\alpha_1) = 1$ signified by the dotted diagonal line. At $q = \frac{1}{2}$ there is the symmetry axis (Sec. 8.2.3) to the right (left) of which in the grey (white) region $f(\alpha)$ is determined by vibrational amplitudes $|u_i|^2 < L^{-d}$ ($|u_i|^2 > L^{-d}$). Adapted from Ref. [157].

Relation Between the Mass Exponents and the Singularity Spectrum

We will show that the set of mass exponents $\tau(q)$ is directly related to the singularity spectrum, such that the multifractal state can be described by either. We start by defining the ensemble average of the gIPRs in terms of the probability density function (PDF) of the individual box amplitudes $\mathcal{P}(\mu_k)$ as

$$\langle R_q \rangle \equiv \lambda^{-d} \langle \mu_k^q(\lambda) \rangle = \lambda^{-d} \int_0^1 \mathcal{P}(\mu_k) \mu_k^q(\lambda) d\mu_k, \quad (8.16)$$

where $\langle \dots \rangle$ represents an average over the system volume and every disorder realisation and the normalisation of $\mu_k(\lambda)$ gives the limits of the integration. To establish the relation we make the change of variable, $\mathcal{P}(\mu_k) d\mu_k = \mathcal{P}(\alpha) d\alpha$ so that in terms of α the box amplitude is parameterised such that $\mu_k(\lambda) \equiv \lambda^\alpha$ and we have

$\alpha \equiv \log \mu_k / \log \lambda$. We are left with

$$\lambda^{-d} \langle \mu_k^q(\lambda) \rangle = \lambda^{-d} \int_0^\infty \mathcal{P}(\tilde{\alpha}) \lambda^{q\tilde{\alpha}} d\tilde{\alpha}. \quad (8.17)$$

Now in terms of the PDF we find that the number of boxes having the same $\mu_k = \lambda^\alpha$ is $N_\alpha \propto \mathcal{P}(\alpha) \lambda^{-d} \propto \lambda^{-f(\alpha)}$ and we can therefore substitute into Eqn. (8.17) the relation $\mathcal{P}(\alpha) \propto \lambda^{d-f(\alpha)}$ such that

$$\lambda^{-d} \langle \mu_k^q(\lambda) \rangle \propto \int_0^\infty \lambda^{q\tilde{\alpha} - f(\tilde{\alpha})} d\tilde{\alpha}, \quad (8.18)$$

$$\propto \int_0^\infty e^{-\tilde{F}(\tilde{\alpha}) |\ln \lambda|} d\tilde{\alpha}, \quad (8.19)$$

being careful to note that $\tilde{F}(\tilde{\alpha}) = q\tilde{\alpha} - f(\tilde{\alpha})$. The integral is solved using the saddle point method [165] under the assumption that L is large (similarly λ is small) and that \tilde{F} has a unique global maximum ($\tilde{\alpha} = \alpha$) which is not the end point of the integral, giving the relations

$$q = f'(\alpha), \quad (8.20)$$

$$\tau(q) = q\alpha - f(\alpha), \quad f(\alpha) = q\alpha - \tau(q). \quad (8.21)$$

From Eqn. (8.20) we can easily see that the maximum of the singularity spectrum is found at $q = 0$ as shown in the schematic in Fig. 8.6. Using Eqns. (8.20) and (8.21) we go on to find

$$q = q + \alpha \frac{dq}{d\alpha} - \frac{d\tau}{dq} \frac{dq}{d\alpha}, \quad (8.22)$$

which gives rise to the following expression for the Lipschitz-Hölder exponent

$$\alpha_q = \frac{d\tau(q)}{dq}. \quad (8.23)$$

The set of equations from (8.20) to (8.23) establishes that $f(\alpha)$ and $\tau(q)$ are related by a Legendre transformation [35]. They also reveal many typical characteristics of the singularity spectrum as shown in Fig. 8.6. We see that the maximum of the singularity spectrum is at $\alpha_0 \geq d$ where $f(\alpha_0) = d$, $f(\alpha_1) = \alpha_1$ and $f'(\alpha_1) = 1$.

The $f(\alpha)$ must be independent of all length scales, L and l at the LDT, for true multifractals. For decreasing disorder the spectrum narrows and converges to the point $f(d) = d$, with increasing system size L . For increasing disorder the spectrum broadens and in the limit of strong disorder it converges to the points $f(0) = 0$ and $f(\infty) = d$ [93].

Parabolic Approximation of the Singularity Spectrum

Due to the universal nature of the spectrum [163,166], approximations of the shape based on analytical calculations for the AM at criticality close to the metallic regime should also serve as a good approximation to the phonon multifractal spectrum at criticality. Ref. [167] outlines a parabolic approximation to the singularity spectrum in $d = 2 + \epsilon$ dimensions (where $\epsilon \ll 1$) as

$$f(\alpha) \approx d - \frac{[\alpha - (d + \epsilon)]^2}{4\epsilon}, \quad (8.24)$$

and for the case where $d = 3$ ($\epsilon = 1$) we have $f(\alpha) = d - (\alpha - \alpha_0)^2/4$, where $\alpha_0 = d + \epsilon$. This approximation has been shown to be exact for some models [168] and in agreement with the recently proposed symmetry relation [95] (Sec. 8.2.3) so long as the $f(\alpha)$ spectrum is contained in the interval $[0, 2d]$. For the 3D AM Eqn. (8.24) does not describe the numerically obtained spectrum, and that $f(\alpha)$ deviates from a parabolic behaviour [157,169].

Symmetry Relation

Further to the parabolic approximation of the singularity spectrum, in 2006 an exact symmetry relation [95] has been derived for the multifractal exponents of the Anderson transition. The symmetry is established for the anomalous scaling exponents, Δ_q , which are defined as the additional contributions to the metallic state mass exponents at criticality. At criticality, the mass exponent from Eqn. (8.13) are rewritten as

$$\tau(q) = d(q - 1) + \Delta_q. \quad (8.25)$$

The anomalous scaling exponents characterise the critical transition [170], and vanish in the extended regime. The anomalous scaling exponents have been shown to determine the scale dependence of the local DOS in an electronic system [163]. The predicted symmetry for the exponents is

$$\Delta_q = \Delta_{1-q}, \quad (8.26)$$

and establishes an axis of symmetry within the singularity spectrum at $q = \frac{1}{2}$ (see Fig. 8.6). It stems from a symmetry relation in the LDT [171], obtained using the NL σ M. The AM does not exactly map onto the NL σ M, although this relation is expected to hold true, due to the universality of the critical exponents [44]. The symmetry relation of the anomalous multifractal exponents Δ_q can be re-written in

terms of the mass exponents as

$$d(2q - 1) = \tau(q) - \tau(1 - q). \quad (8.27)$$

Now using the Legendre transform in Sec. 8.2.3 on the mass exponents we find $f(\alpha_q = \frac{d\tau_q}{dq})$ and $-\alpha_{1-q} = \frac{d\tau(1-q)}{d(1-q)} \frac{d(1-q)}{dq}$ provides the symmetry of

$$\alpha_q + \alpha_{1-q} = 2d, \quad (8.28)$$

$$f(2d - \alpha) = f(\alpha) + d - \alpha, \quad (8.29)$$

where Eqn. (8.29) is obtained by substituting of Eqns. (8.27) and (8.28) into $f(\alpha_{1-q}) = (1 - q)\alpha_{1-q} - \tau_{1-q}$. As mentioned above, the symmetry axis is at $q = \frac{1}{2}$ which corresponds to $\alpha_{1/2} = d$. In Fig. 8.6 two points related by the symmetry relation (at $\alpha_1 = 2d - \alpha_0$, $q = 1$ and α_0 , $q = 0$) are clearly labelled, although all intermediate points around the symmetry axis are equally described by the relation. We can also infer the upper and lower limits of the singularity spectrum based on the knowledge that due to the normalisation condition of the vibrational eigenmodes, α must be positive and therefore $\alpha_{\min} = 0$. With the symmetry axis at $\alpha = d$, the relation should therefore terminate at $\alpha = 2d$, establishing an upper limit $\alpha_{\max} = 2d$.

The symmetry relation has been experimentally verified in multifractal analysis of vibrations in elastic networks [172] and has been accurately studied theoretically for the AM [93, 157]. These two systems have independent analogies to our current model.

Amongst others, numerical calculations of 1D power-law random-banded-matrices [95] and 2D Anderson transition in the spin-orbit symmetry class [173] also support the symmetry in the singularity spectra. See Refs. [24]-[29] in Rodriguez et al. [169] for a more comprehensive list. We therefore expect the symmetry relation to hold for multifractal analysis of phonons in disordered harmonic crystals.

8.2.4 Numerical Implementation

In order to numerically obtain an accurate singularity spectrum we use a disorder averaged form of the gIPR scaling law in the limit $\lambda \equiv l/L \rightarrow 0$ and take into account all contributions from finite-sized critical vibrational eigenstates. We use an ensemble averaging technique with system size scaling as opposed to typical averaging techniques as finite size effects are minimised with the former. For a rigorous discussion of other available techniques the author recommends Refs. [93, 157, 174].

We start with the same assumptions made in Sec. 8.2.2 and in addition to Eqns. (8.9) and (8.10) we find it convenient to define the parameter S_q as

$$S_q \equiv \frac{dR_q}{dq} = \sum_k \mu_k^q \cdot \ln \mu_k. \quad (8.30)$$

The ensemble average technique requires the arithmetic average of all the R_q 's for each disorder realisation and therefore we rewrite Eqn. (8.11) as

$$\langle R_q(\lambda) \rangle \propto \lambda^{\tau_{\text{ens}}(q)}, \quad (8.31)$$

where $\langle \dots \rangle$ represents the arithmetic average over all eigenstates belonging to different and uncorrelated disorder realisations. Equivalently, Eqn. (8.12) becomes

$$\tau_{\text{ens}}(q) = \lim_{\lambda \rightarrow 0} \frac{\ln \langle R_q(\lambda) \rangle}{\ln \lambda}. \quad (8.32)$$

To obtain the mass exponents $\tau_{\text{ens}}(q)$ we perform a linear fitting of $Y_{\tau_{\text{ens}}(q)} \equiv \ln \langle R_q \rangle$ against $\ln \lambda$, where λ varies by changing system size L only. The standard deviation of the data is given by $\text{stdev}(Y_{\tau_{\text{ens}}(q)}) = \sigma_{\langle R_q \rangle} / \langle R_q \rangle$, where $\sigma_{\langle R_q \rangle}$ represents the standard deviation of $\langle R_q \rangle$. The mass exponents $\tau_{\text{ens}}(q)$ are then estimated from the slopes of the linear fits for each q (see Fig. 8.8(a)). In a similar manner we find that the singularity strengths α_q , parametrized as a function of q , are given by

$$\alpha_q \equiv \frac{d\tau_{\text{ens}}(q)}{dq} = \lim_{\lambda \rightarrow 0} \frac{1}{\ln \lambda} \frac{\langle S_q \rangle}{\langle R_q \rangle}. \quad (8.33)$$

We define the parameter $Y_{\alpha_q} \equiv \langle S_q \rangle / \langle R_q \rangle$ such that

$$\text{stdev}(Y_{\alpha_q}) = \sqrt{\frac{\sigma_{\langle S_q \rangle}^2}{\langle R_q \rangle^2} + \frac{\langle S_q \rangle^2}{\langle R_q \rangle^4} \sigma_{\langle R_q \rangle}^2 - 2 \frac{\langle S_q \rangle}{\langle R_q \rangle^3} \text{cov}(\langle S_q \rangle, \langle R_q \rangle)}. \quad (8.34)$$

We emphasise that the averages $\langle S_q \rangle$ and $\langle R_q \rangle$ are calculated from the same set of eigenstates, and thus are strongly correlated due to the definition (8.30) of $\langle S_q \rangle$. The covariance term in the above formula is then essential for a correct estimation of the uncertainty. The α_q values are obtained from the slopes of the linear fits of Y_{α_q} versus $\ln \lambda$ (see Fig. 8.8(b)). Finally, using the Legendre transformation in Eqn. (8.21) we have

$$f_q \equiv q\alpha_q - \tau_{\text{ens}}(q) = \lim_{\lambda \rightarrow 0} \frac{1}{\ln \lambda} \left(\frac{q \langle S_q \rangle}{\langle R_q \rangle} - \ln \langle R_q \rangle \right). \quad (8.35)$$

Similarly, defining $Y_{f_q} = \frac{q\langle S_q \rangle}{\langle R_q \rangle} - \ln\langle R_q \rangle$ and its standard deviation

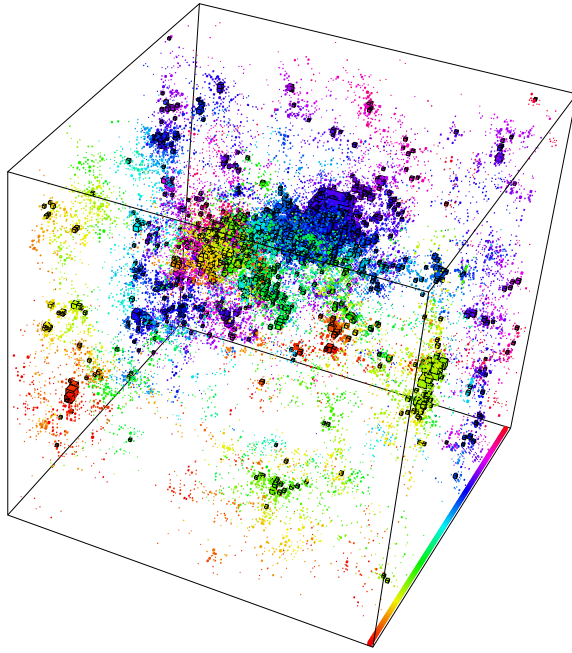
$$\text{stdev}(Y_{f_q}) = \sqrt{\frac{q^2\sigma_{\langle S_q \rangle}^2}{\langle R_q \rangle^2} + \frac{(q\langle S_q \rangle + \langle R_q \rangle)^2}{\langle R_q \rangle^4}\sigma_{\langle R_q \rangle}^2 - 2\frac{q(q\langle S_q \rangle + \langle R_q \rangle)}{\langle R_q \rangle^3}\text{cov}(\langle S_q \rangle, \langle R_q \rangle)}, \quad (8.36)$$

we can estimate f_q from the linear fit of Y_{f_q} versus $\ln\lambda$. From the pairs of values $\{\alpha_q, f_q\}$ we construct the singularity spectrum $f(\alpha)$ (see Fig. 8.9).

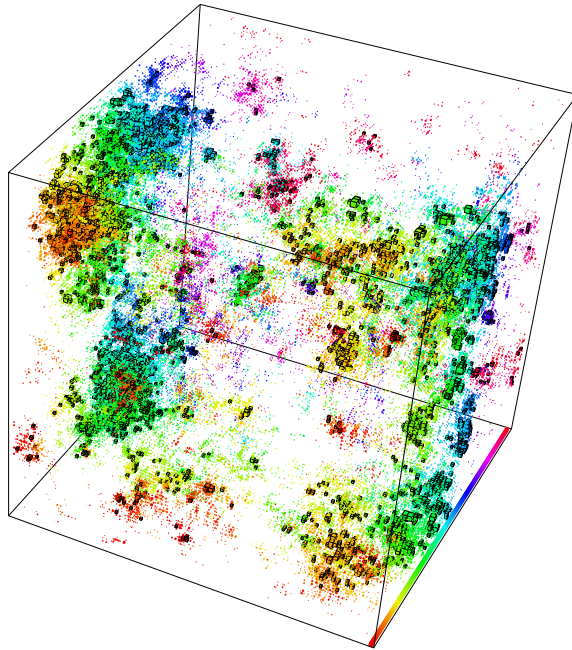
We select disorder strengths for both mass and spring constant disorder types for multifractal analysis, namely $\Delta m = 1.2$ and $\Delta k = 1$ and $\Delta k = 10$. Due to FSS of the reduced localisation lengths in Sec. 6.3.1 we already have accurate estimates of the LDT for these disorders. In order to minimise the influence of finite size effects, we need to investigate the largest possible vibrational eigenstates that can be computed in an acceptable time frame. The computational resource used for this contains 12 cores of Intel Xeon X5650 ‘‘Westmere-EP’’ 2.66 GHz cores, with 24GB of shared memory. Memory is the largest constraint for sparse matrix diagonalisation (discussed in Sec. 3.2) and limits the system sizes achievable. For symmetric spring constant disordered systems, we compute eigenstates in a cube of volume $L^3 = 100^3$, whereas in the non-symmetric mass disordered systems, we set the corresponding maximum system volume as $L^3 = 90^3$. Roughly 30 minutes of computing time is required to obtain each of the largest volume eigenstates in both symmetric and non-symmetric systems. Two examples of critical eigenstate intensities for these maximum system sizes for mass disorder $\Delta m = 1.2$ and spring constant disorder $\Delta k = 10$ are shown in Fig. 8.7.

In total, we compute 5000 states for each system size from $L^3 = 20^3$ to the above prescribed maxima at intervals of $\Delta L = 10$. It has been found in a previous study that correlations between states near to the LDT for identical disorder distributions has adverse effects on the overall multifractal analysis [169]. We therefore only consider a single critical state close to the LDT for each individual disorder realisation. The box amplitude and the corresponding q -moments are calculated using box-size $l = 1$ for non-negative moments ($q \geq 0$) and $l > 1$ (for all cases $l = 2$ has proven adequate) for $q < 0$, in order to minimise the uncertainty in the small amplitudes of the eigenstates [169].

In Figs. 8.8 and 8.9 we show examples of the linear fits for τ_{ens} , α_q and f_q , respectively, for values of q as labelled within the figures. We see that at q values nearer to $q = 0$, the data has a higher quality of fit, as expected, due to the increase of the error for higher moments of q . We find especially in the mass disorder case, higher fluctuations at the edges of the range of q moments compared to that of both



(a)



(b)

Figure 8.7: Critical eigenstate intensity distributions $|u_j|^2$ obtained from exact diagonalisation for system of size (a) $L^3 = 90^3$ for mass disorder $\Delta m = 1.2$ at frequency $\omega_c^2 = 12.681$ and (b) $L^3 = 100^3$ for spring constant disorder $\Delta k = 10$ at frequency $\omega_c^2 = 19.75$. All sites with $|u(\vec{r}_j)|^2 / L^3 \sum_j |u(\vec{r}_j)|^2 > 1$ are shown as small cubes and those with black edges have $|u(\vec{r}_j)|^2 / L^3 \sum_j |u(\vec{r}_j)|^2 > \sqrt{1000}$ and $|u_j|^2 < \langle |u_j|^2 \rangle$ are not displayed. The colour scale distinguishes between different slices of the system along the axis into the page.

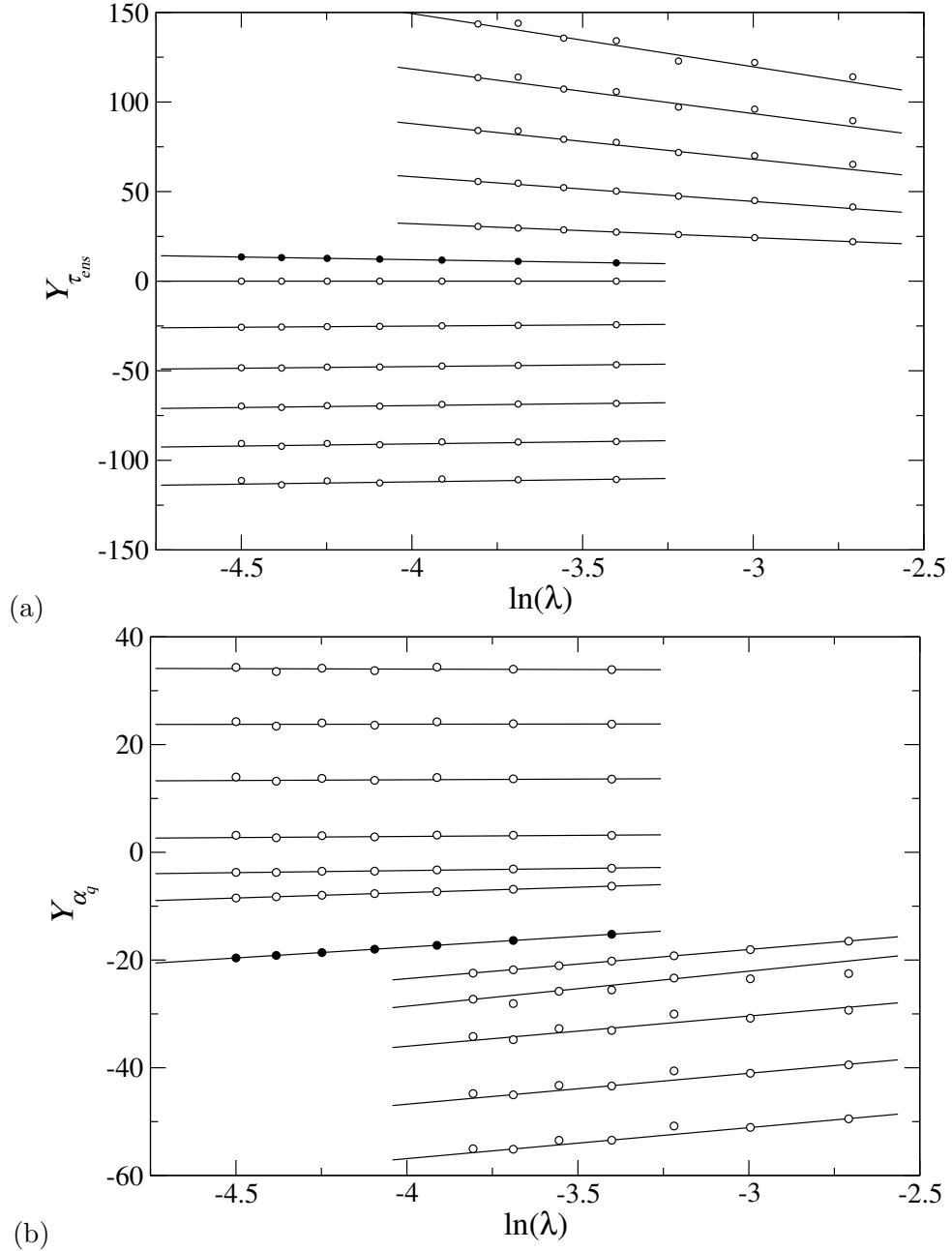


Figure 8.8: Linear fits for mass disorder $\Delta m = 1.2$ of (a) $Y_{\tau_{ens}}$ and (b) Y_{α_q} against $\ln(\lambda)$ for linear system sizes 30-90 and integer q moments from 6 (top), 5, ..., 0, -1, ..., -5 (bottom). The slopes give (a) τ_{ens} and (b) α_q for the particular q which can be seen plotted as a function of q in Fig. 8.10(a) and Fig. 8.10(b), respectively. Data points for $q \neq 0$ have been properly shifted vertically to ensure optimal visualisation. Data for $q = 0$ has filled symbols. Note the $\ln(\lambda)$ scale varies from positive to negative q due to the selection of box size l . When not shown, standard deviations are contained within symbol size.

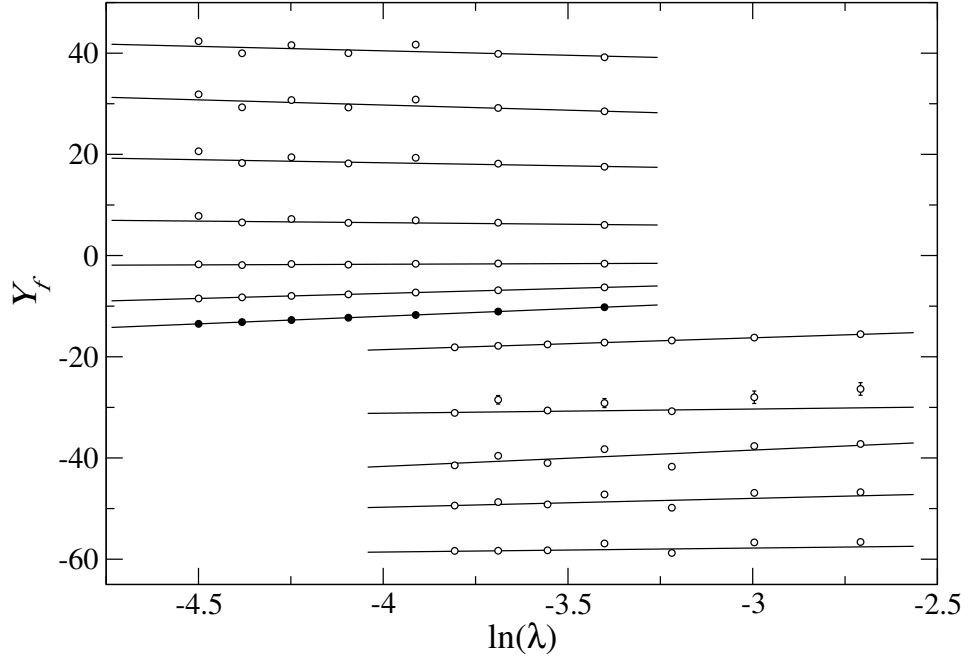


Figure 8.9: Linear fits for mass disorder $\Delta m = 1.2$ of Y_{f_q} against $\ln(\lambda)$ for linear system sizes 30-90 and integer q moments from 6 (top), 5, ..., 0, -1, ..., -5 (bottom). The slopes give f_q for the particular q which can be seen plotted with their corresponding α_q in Fig. 8.10(b) which forms the singularity spectrum. Figure properties as in Fig. 8.8.

spring constant disorder magnitudes by comparing the singularity spectra in Figs. 8.10(b), 8.11(b) and 8.12(b).

Comparison of Electron and Phonon $f(\alpha)$

As expected from the definition (8.32), and as a consequence of the eigenstate normalisation, in all cases $\tau_{\text{ens}}(0) = -d$ and $\tau_{\text{ens}}(1) = 0$. This can be seen in all plots of τ_{ens} versus q (Figs. 8.10(a), 8.11(a) and 8.12(a)). We also see that τ_{ens} is non-linear in q and therefore shows signs of multifractality [158].

We plot for each of the selected disorders (Figs. 8.10(b), 8.11(b) and 8.12(b)), the singularity spectrum with the corresponding symmetry relation discussed in Sec. 8.2.3. This relation has been shown to be satisfied, within statistical error, for the electronic Anderson MIT [157]. We find that for disorders $\Delta m = 1.2$ (Fig. 8.10(b)) and $\Delta k = 10$ (Fig. 8.12(b)) the symmetry relation holds within error in the α -range that is statistically reliable. In the tails of the spectrum, which are obtained from large $|q|$ values, a higher number of disorder realisations are needed to reduce the

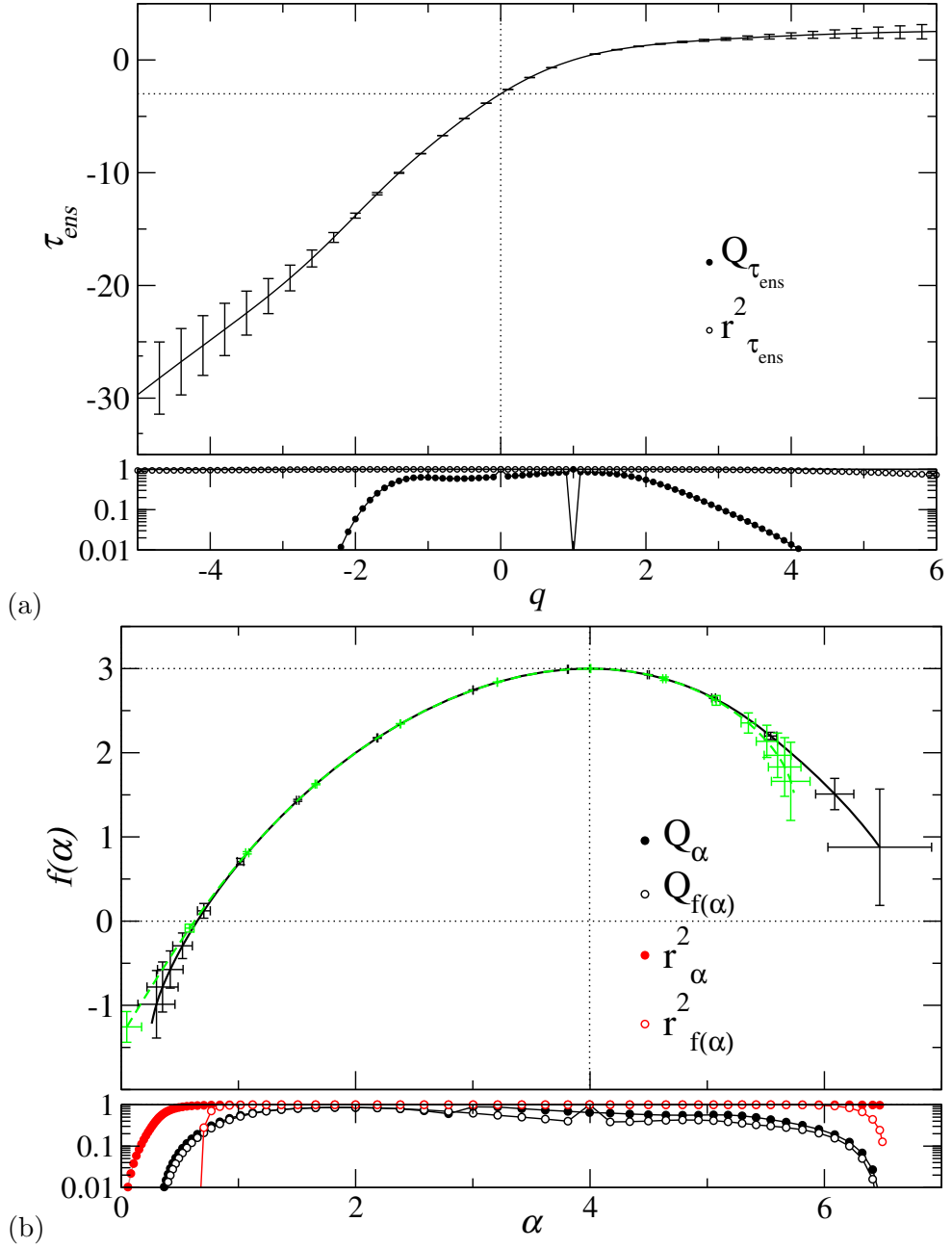


Figure 8.10: For mass disorder $\Delta m = 1.2$ and critical transition frequency of $\omega_c^2 = 12.681$ from 5000 eigenstates for each system size $L^3 = 30^3$ to $L^3 = 90^3$ in steps of $\delta L = 10$. Panel (a) shows $\tau_{\text{ens}}(q)$ as a function of q with error bars at every third data point. Panel (b) displays the singularity spectrum $f(\alpha)$ (black solid line) with corresponding symmetry transformed spectrum $f(2d - \alpha) = f(\alpha) + d - \alpha$ (green dashed line), only every third symbol is shown with associated error (one standard deviation). The values of linear correlation coefficient r^2 and quality of fit parameter Q for the linear fits used to estimate τ_{ens} , α_q and f_q are given in the base plot. Note that $\tau_{\text{ens}}(1) = 0$ for all L and that the points in the linear fitting are uncorrelated, therefore $r^2 = 0$ for $q = 1$.

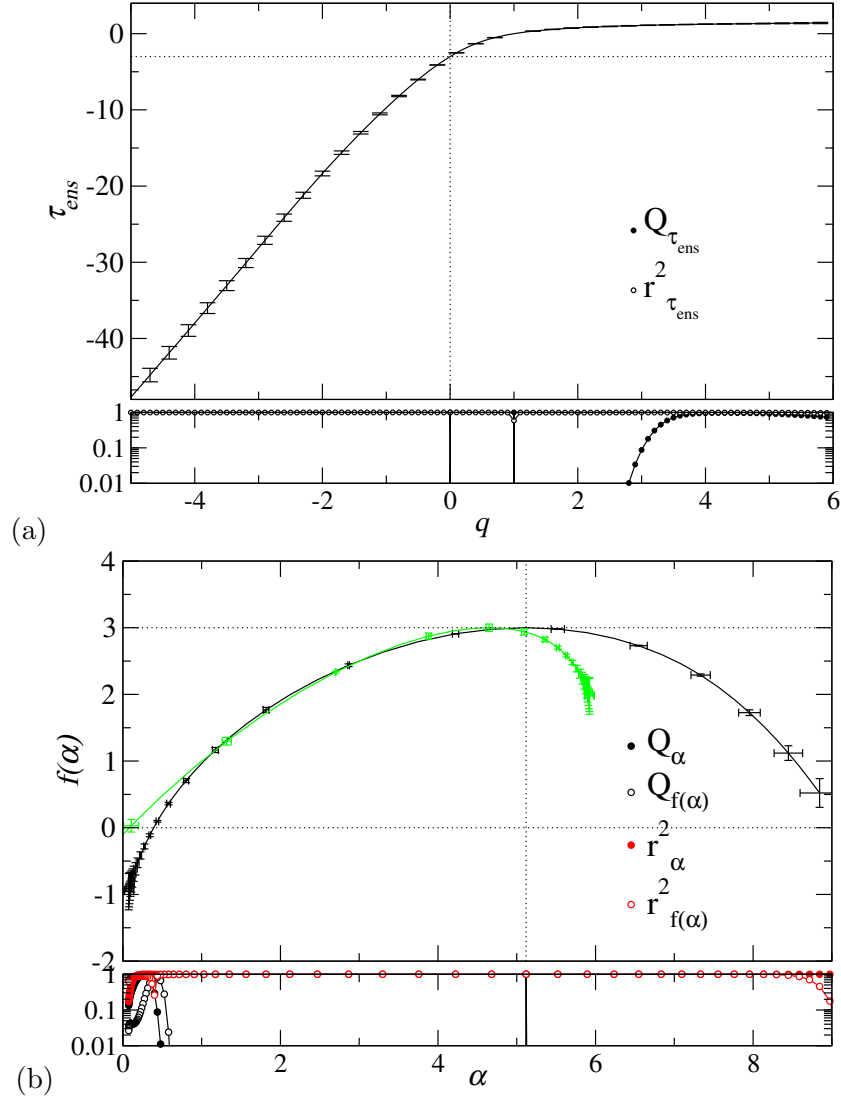


Figure 8.11: Panel (a) shows $\tau_{\text{ens}}(q)$ as a function of q with error bars at every third data point. Panel (b) displays the singularity spectrum $f(\alpha)$ (black solid line) for spring constant disorder $\Delta k = 1$ and critical transition frequency of $\omega_c^2 = 12.527$ from 5000 eigenstates for each system size $L^3 = 20^3$ to $L^3 = 100^3$ in steps of $\delta L = 10$. Figure properties as in Fig. 8.10.

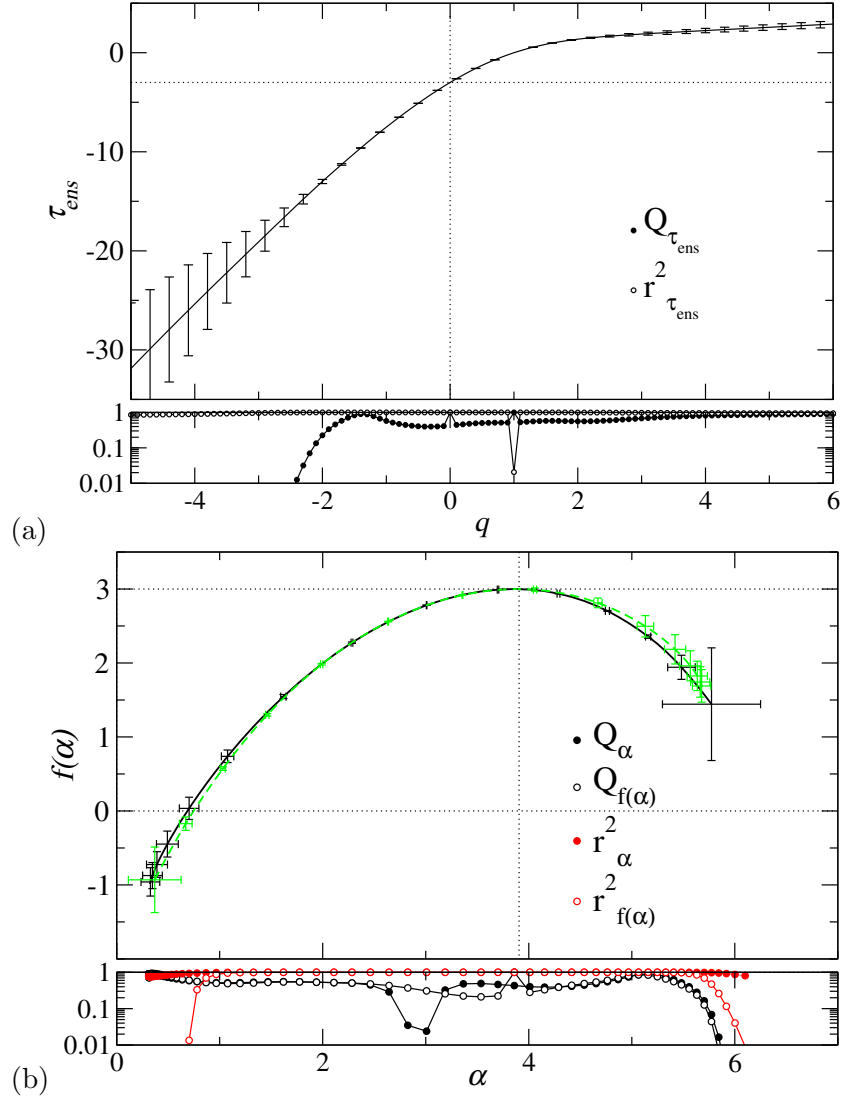


Figure 8.12: Panel (a) shows $\tau_{ens}(q)$ as a function of q with error bars at every third data point. Panel (b) displays the singularity spectrum $f(\alpha)$ (black solid line) for spring constant disorder $\Delta k = 10$ and critical transition frequency of $\omega_c^2 = 19.75$ from 5000 eigenstates at each system size $L^3 = 50^3$ to $L^3 = 100^3$ in steps of $\delta L = 10$. Figure properties as in Fig. 8.10.

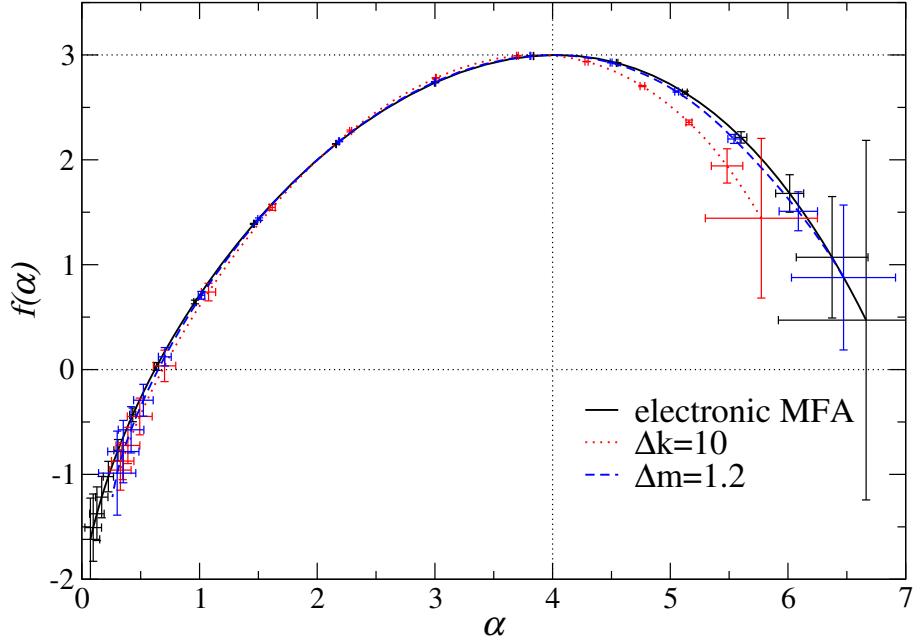


Figure 8.13: Singularity spectrum $f(\alpha)$ comparison with the high precision electronic singularity spectrum found at the MIT [175] (black line) and the two phonon singularity spectra for $\Delta m = 1.2$ (blue line) and $\Delta k = 10$ (red line) from Figs. 8.10 and 8.12, respectively.

statistical fluctuations. Therefore an increase in the uncertainty of $f(\alpha)$ is to be expected at the tails.

The singularity spectrum for disorder $\Delta k = 1$ (Fig. 8.11(b)) does not follow the expected trend. The symmetry relation is not very well satisfied and the maximum is not found at $\alpha_0 \simeq 4$. We note that the spectrum for $\Delta k = 1$ has broadened more than expected at criticality and α extends beyond the expected maximum limit of $2d$. Relating these findings back to the initial reduced localisation lengths in Sec. 6.3 we see that the LDT of disorder $\Delta k = 1$ has the highest irrelevant shift of all six high accuracy points that were finite size scaled. Because of this and due to the broader than expected singularity spectrum we conclude that our estimate for the transition frequency may be further into the localised regime than the critical regime. We also note that in the spring disorder case that near criticality there is a lower VDOS and therefore the frequencies of the states obtained from numerical diagonalisation fluctuate more than in the mass disordered case.

In Fig. 8.13 we compare the two phonon multifractal spectra that satisfy the symmetry relation within error with the electronic $f(\alpha)$ spectrum obtained for the MIT in Ref. [157]. We see that all three singularity spectra overlap within their

95% confidence intervals for $\alpha \leq 4$. The deviation that can be observed for the case of spring disorder at $\alpha > 4$ is most likely a consequence of the uncertainty in the location of the critical point for this disorder and we emphasise that the critical point has been found in a region of very low VDOS. This not only makes the estimation of ω_c^2 particularly challenging, but also the distribution of eigenvalues and eigenstates used in the MFA, around ω_c^2 , become wider, thus increasing the underlying uncertainty in the multifractal spectrum.

In summary, we have shown the agreement of the multifractal spectrum of the LDT for phonons with either mass or spring disorder, and electrons in the AM, for three different points on the mobility edge in their corresponding phase diagrams. This confirms the earlier findings that these models exhibit the same critical properties.

Chapter 9

Conclusions

To summarise, the aim of this work is to characterise phonon modes in disordered harmonic lattices, specifically 1D and 3D systems. We study the effect of disorder on the phonon modes and particularly the dependence of localisation length on the magnitude/type of disorder and frequency of the excitation. Much of the work has been based on analogies between electron and phonon systems and we have successfully developed a transformation to re-use known properties of electrons to obtain phonon characteristics.

In 1D systems our results conform to the scaling theory of localisation by showing that finite localisation lengths exist for all non-zero frequency phonon modes in disordered systems. We confirm the non-existence of a LDT throughout the whole frequency band for both uniform mass and spring constant disorders. We also use the relative simplicity of the 1D system to test the reliability of numerical methods against analytical results which are then used throughout the 3D investigation. Furthermore, numerous disorder realisations/distributions are investigated as a preview of likely effects before concentrating on a single realisation of disorder type in 3D systems. As a consequence, uniform disorder for both mass and spring constant cases is used due to the relative simplicity of implementation and the ability to increase the measure of disorder strength beyond limits imposed in other research of the same systems to study analogies with electronic disordered systems.

In 3D we start by comparing the canonical equations for a potential disordered electronic system with that of the mass disordered phonon system. We obtain a set of transformation relations that convert the phase boundary from the electronic phase diagram for the LDT to that of a phonon phase boundary. This direct translation reveals a phase boundary that extends beyond Δk or $\Delta m = 2$ and implies that even in 3D an infinite disorder strength is required to localise the zero-frequency modes. The phase diagrams for both mass and spring constant disorder

are confirmed with high precision TMM computations with an accuracy within 0.1% of the standard deviation of the Lyapunov exponents. These studies show consistent results within error for the LDT phase boundaries and confirm that phonons do in fact experience localisation phenomena for any disorder magnitude. The high precision reduced localisation lengths are finite size scaled and Monte Carlo stability analysis is applied to obtain critical parameters and error estimates as accurate as possible. The critical parameters are consistent with previous studies of the AM for electron systems and we confirm that the phonon localisation problem is of the same universality class as that of the electronic problem.

The VDOS is found numerically for both mass and spring constant disorder and confirmed with CPA calculations. For spring constant disorder, the CPA calculations are now standard, using the two-site model, but for mass disorder the single site CPA is difficult to implement due to the loss of symmetry in the dynamical matrix as a direct consequence of the disorder in the masses. In this case the DOS was calculated for the potential disordered electronic case using a frequency dependant disorder distribution and transformed to that of the phonon VDOS. The transformation gives a satisfactory fit with the phonon numerical data. From the VDOS (both numerical and CPA) we locate the position of the BP in the frequency domain and find that the properties of the states that surround the BP trajectory appear to be affected by the presence of the BP. The nature of the influence of the BP on the normal modes is a matter for further investigation. We also confirm that there is no simple correlation between the BP frequency and the LDT.

With vibrational eigenstate statistics we find that in the localised regime the displacement fluctuations of the states heavily depart from the GOE and that disorder has little effect on the vibrational modes prior to the LDT. We also find that around the BP frequency there is an anomalous deviation from GOE indicating the possible significance of the BP. It is generally understood that plane waves ($\omega < \omega_{BP}$) as well as the random-matrix states ($\omega > \omega_{BP}$) obey the GOE statistics rather well, whereas the states at the cross-over (i.e. the states with $\omega = \omega_{BP}$) have a maximum deviation from GOE. This may support the conjecture that the BP signifies the crossover between plane waves and random matrix states.

Using MFA we find that for LDTs, whose critical parameters are not influenced by a low VDOS (namely $\Delta k = 10$ and $\Delta m = 1.2$), the singularity spectrum satisfies the newly proposed symmetry relation within error. We also see that the singularity spectrum is largely within error of the electronic singularity spectrum at the MIT confirming the previous findings that these models exhibit the same critical properties.

Appendices

A Tables of Critical Parameters

In Sec. 6.3.2 we show the stable fits from FSS, the below tables include the next highest order fits used in stability analysis. Tabs. A. 1. and A. 2. are for the mass disorders $\Delta m = 1, 2, 4$ and 9 for spectral variables ω^2 and ω , respectively. Tabs. A. 3. and A. 4. are for spring constant disorders $\Delta k = 1, 7$ and 10 for spectral variables ω^2 and ω , respectively.

B Weighted Averaging

To take a weighted mean of a set of N independent numbers with symmetric error bars we must first work out the weighting factors w_i of each number, as

$$w_i = \frac{1}{\sigma_i^2} \quad (9.1)$$

where i is the index of the number and σ is the standard error/deviation. Therefore the weighted mean \bar{y} of the independent numbers y_i is

$$\bar{y} = \frac{\sum_{i=1}^N w_i y_i}{\sum_{i=1}^N w_i} \quad (9.2)$$

and the corresponding weighted standard deviation is

$$\sigma_{\bar{y}} = \sqrt{\frac{1}{\sum_{i=1}^N w_i}}. \quad (9.3)$$

When working with unsymmetric error bars we must include contributions from both bars. We use the above equations with a phantom set of data that includes all numbers twice, where each individual unsymmetric error bar is treated as a symmetric one, hence the data set is doubled. This method will give a weighted

$\Delta m = 1.2$												
M	ω^2	n_{r_0}	n_{r_1}	n_i	m_r	m_i	ω_c^2	ν	y	χ^2	μ	Γ_q
8-20	12.15 - 13.1	2	3	1	2	0	$12.681^{+0.056}_{-0.034}$	$1.57^{+0.14}_{-0.09}$	$1.46^{+0.83}_{-1.45}$	165^{+38}_{-34}	165	0.84
8-20	12.15 - 13.1	3	3	1	2	0	$12.700^{+0.058}_{-0.046}$	$1.50^{+0.23}_{-0.23}$	$1.15^{+0.73}_{-1.30}$	164^{+36}_{-36}	164	0.86
8-20	12.15 - 13.1	2	4	1	2	0	$12.679^{+0.046}_{-0.033}$	$1.57^{+0.14}_{-0.09}$	$1.53^{+0.78}_{-1.39}$	164^{+38}_{-34}	164	0.83
8-20	12.15 - 13.1	2	3	1	3	0	$12.676^{+0.032}_{-0.031}$	$1.56^{+0.11}_{-0.08}$	$1.59^{+0.68}_{-1.53}$	163^{+38}_{-34}	164	0.82
8-20	12.15 - 13.1	2	3	1	2	1	$12.693^{+0.067}_{-0.044}$	$1.63^{+0.22}_{-0.14}$	$1.31^{+0.82}_{-1.53}$	164^{+38}_{-34}	164	0.87
$\Delta m = 4$												
M	ω^2	n_{r_0}	n_{r_1}	n_i	m_r	m_i	ω_c^2	ν	y	χ^2	μ	Γ_q
8-20	3.75 - 4.25	3	2	1	1	0	$4.134^{+0.024}_{-0.020}$	$1.57^{+0.06}_{-0.08}$	$1.08^{+0.24}_{-0.25}$	572^{+69}_{-64}	573	0.99
8-20	3.75 - 4.25	4	2	1	1	0	$4.133^{+0.024}_{-0.020}$	$1.58^{+0.06}_{-0.08}$	$1.09^{+0.24}_{-0.25}$	572^{+66}_{-65}	572	0.99
8-20	3.75 - 4.25	3	3	1	1	0	$4.134^{+0.026}_{-0.020}$	$1.59^{+0.08}_{-0.10}$	$1.08^{+0.25}_{-0.25}$	572^{+69}_{-64}	572	0.99
8-20	3.75 - 4.25	3	2	1	2	0	$4.133^{+0.024}_{-0.020}$	$1.57^{+0.09}_{-0.10}$	$1.09^{+0.24}_{-0.25}$	572^{+65}_{-64}	572	0.99
8-20	3.75 - 4.25	3	2	1	1	1	$4.134^{+0.026}_{-0.021}$	$1.57^{+0.09}_{-0.10}$	$1.09^{+0.26}_{-0.27}$	572^{+70}_{-64}	572	0.99
$\Delta m = 9$												
M	ω^2	n_{r_0}	n_{r_1}	n_i	m_r	m_i	ω_c^2	ν	y	χ^2	μ	Γ_q
8-20	-1.65 - -1.5	2	3	1	2	0	$-1.623^{+0.018}_{-0.037}$	$1.56^{+0.41}_{-0.18}$	$0.82^{+0.50}_{-0.47}$	154^{+37}_{-33}	154	0.87
8-20	-1.65 - -1.5	3	3	1	2	0	$-1.610^{+0.013}_{-0.017}$	$1.50^{+0.20}_{-0.16}$	$1.16^{+0.46}_{-0.50}$	154^{+37}_{-33}	153	0.90
8-20	-1.65 - -1.5	2	4	1	2	0	$-1.605^{+0.011}_{-0.020}$	$1.50^{+0.14}_{-0.10}$	$1.37^{+0.62}_{-0.52}$	153^{+37}_{-33}	153	0.90
8-20	-1.65 - -1.5	2	3	1	3	0	$-1.607^{+0.011}_{-0.018}$	$1.52^{+0.19}_{-0.12}$	$1.26^{+0.50}_{-0.49}$	154^{+38}_{-34}	153	0.90
8-20	-1.65 - -1.5	2	3	1	2	1	$-1.624^{+0.020}_{-0.037}$	$1.55^{+0.65}_{-0.82}$	$0.81^{+0.51}_{-0.51}$	153^{+36}_{-32}	153	0.86

Table A.1: Critical parameter ω_c^2 and ν for pure mass disorder transitions $\Delta m = 1.2, 4$ and 9 computed from FSS obtained in the given M and ω^2 ranges and with the orders of the expansion given by n_{r_0} , n_{r_1} , n_i , m_r and m_i . The minimised χ^2 value, the degrees of freedom μ and the resulting goodness-of-fit parameter Γ_q are also shown for each fit. Extended table includes higher order fits used for stability analysis.

$\Delta m = 1.2$												
M	ω	n_{r_0}	n_{r_1}	n_i	m_r	m_i	ω_c	ν	y	χ^2	μ	Γ_q
8-20	3.485 - 3.62	2	3	1	2	0	3.561 ^{+0.008} _{-0.005}	1.57 ^{+0.15} _{-0.09}	1.47 ^{+0.81} _{-1.43}	164 ⁺³⁸ ₋₃₄	165	0.84
8-20	3.485 - 3.62	3	3	1	2	0	3.564 ^{+0.010} _{-0.007}	1.51 ^{+0.19} _{-0.26}	1.16 ^{+0.75} _{-1.31}	164 ⁺³⁸ ₋₃₄	164	0.86
8-20	3.485 - 3.62	2	4	1	2	0	3.561 ^{+0.007} _{-0.005}	1.57 ^{+0.14} _{-0.09}	1.52 ^{+0.74} _{-1.41}	164 ⁺³⁷ ₋₃₅	164	0.83
8-20	3.485 - 3.62	2	3	1	3	0	3.561 ^{+0.006} _{-0.002}	1.57 ^{+0.14} _{-0.10}	1.39 ^{+0.65} _{-1.46}	164 ⁺³⁸ ₋₃₄	164	0.83
8-20	3.485 - 3.62	2	3	1	2	1	3.563 ^{+0.009} _{-0.007}	1.63 ^{+0.21} _{-0.14}	1.30 ^{+0.81} _{-1.52}	163 ⁺³⁷ ₋₃₄	164	0.87
$\Delta m = 4$												
M	ω	n_{r_0}	n_{r_1}	n_i	m_r	m_i	ω_c	ν	y	χ^2	μ	Γ_q
8-20	1.936 - 2.062	3	2	1	1	0	2.033 ^{+0.006} _{-0.005}	1.55 ^{+0.07} _{-0.08}	1.07 ^{+0.24} _{-0.25}	573 ⁺⁶⁵ ₋₆₃	573	0.99
8-20	1.936 - 2.062	4	2	1	1	0	2.033 ^{+0.006} _{-0.005}	1.55 ^{+0.06} _{-0.08}	1.08 ^{+0.24} _{-0.26}	572 ⁺⁶⁹ ₋₆₅	572	0.99
8-20	1.936 - 2.062	3	3	1	1	0	2.034 ^{+0.007} _{-0.005}	1.58 ^{+0.08} _{-0.09}	1.07 ^{+0.24} _{-0.26}	572 ⁺⁶⁹ ₋₆₆	572	0.99
8-20	1.936 - 2.062	3	2	1	2	0	2.033 ^{+0.006} _{-0.005}	1.57 ^{+0.08} _{-0.10}	1.08 ^{+0.24} _{-0.24}	572 ⁺⁶⁸ ₋₆₄	572	0.99
8-20	1.936 - 2.062	3	2	1	1	1	2.033 ^{+0.006} _{-0.005}	1.53 ^{+0.11} _{-0.10}	1.10 ^{+0.25} _{-0.26}	571 ⁺⁶⁵ ₋₆₅	572	0.99
$\Delta m = 9$												
M	ω	n_{r_0}	n_{r_1}	n_i	m_r	m_i	ω_c	ν	y	χ^2	μ	Γ_q
8-20	-1.284 - -1.225	2	3	1	1	0	-1.273 ^{+0.006} _{-0.014}	1.56 ^{+0.44} _{-0.17}	0.90 ^{+0.52} _{-0.42}	155 ⁺³⁶ ₋₃₃	155	0.83
8-20	-1.284 - -1.225	3	3	1	1	0	-1.273 ^{+0.007} _{-0.014}	1.58 ^{+0.44} _{-0.19}	0.88 ^{+0.52} _{-0.46}	154 ⁺³⁸ ₋₃₂	154	0.82
8-20	-1.284 - -1.225	2	4	1	1	0	-1.270 ^{+0.005} _{-0.007}	1.51 ^{+0.19} _{-0.12}	1.08 ^{+0.42} _{-0.39}	154 ⁺³⁷ ₋₃₃	154	0.88
8-20	-1.284 - -1.225	2	3	1	2	0	-1.268 ^{+0.005} _{-0.008}	1.50 ^{+0.16} _{-0.12}	1.20 ^{+0.51} _{-0.45}	155 ⁺³⁷ ₋₃₄	154	0.91
8-20	-1.284 - -1.225	2	3	1	1	1	-1.272 ^{+0.006} _{-0.012}	1.60 ^{+0.39} _{-0.43}	0.94 ^{+0.52} _{-0.44}	154 ⁺³⁸ ₋₃₃	154	0.84

Table A.2: Critical parameter ω_c and ν for pure mass disorder transitions $\Delta m = 1.2, 4$ and 9 computed from FSS obtained in the given M and ω ranges and with the orders of the expansion given by n_{r_0} , n_{r_1} , n_i , m_r and m_i . The minimised χ^2 value, the degrees of freedom μ and the resulting goodness-of-fit parameter Γ_q are also shown for each fit. Extended table includes higher order fits used for stability analysis.

$\Delta k = 1$												
M	ω^2	n_{r_0}	n_{r_1}	n_i	m_r	m_i	ω_c^2	ν	y	χ^2	μ	Γ_q
10 - 20	12.48 - 12.6	3	1	1	1	1	12.527 ^{+0.003} _{-0.004}	1.58 ^{+0.05} _{-0.04}	3.76 ^{+0.28} _{-0.27}	132 ⁺³⁴ ₋₃₀	132	0.62
10 - 20	12.48 - 12.6	4	1	1	1	1	12.527 ^{+0.003} _{-0.004}	1.58 ^{+0.05} _{-0.05}	3.78 ^{+0.27} _{-0.27}	130 ⁺³³ ₋₃₀	131	0.62
10 - 20	12.48 - 12.6	3	2	1	1	1	12.527 ^{+0.003} _{-0.003}	1.58 ^{+0.05} _{-0.04}	3.78 ^{+0.26} _{-0.27}	131 ⁺³⁴ ₋₃₀	131	0.70
10 - 20	12.48 - 12.6	3	1	1	2	1	12.528 ^{+0.004} _{-0.004}	1.60 ^{+0.06} _{-0.06}	3.83 ^{+0.27} _{-0.28}	131 ⁺³³ ₋₃₀	131	0.67
10 - 20	12.48 - 12.6	3	1	1	1	2	12.527 ^{+0.003} _{-0.003}	1.57 ^{+0.10} _{-0.06}	3.78 ^{+0.25} _{-0.26}	132 ⁺³⁵ ₋₃₀	131	0.82
$\Delta k = 10$												
M	ω^2	n_{r_0}	n_{r_1}	n_i	m_r	m_i	ω_c^2	ν	y	χ^2	μ	Γ_q
6 - 16	18.8 - 20.3	1	3	1	2	0	19.749 ^{+0.043} _{-0.038}	1.51 ^{+0.08} _{-0.08}	1.55 ^{+0.46} _{-0.80}	176 ⁺³⁹ ₋₃₆	176	0.84
6 - 16	18.8 - 20.3	2	3	1	2	0	19.728 ^{+0.061} _{-0.081}	1.50 ^{+0.17} _{-0.63}	1.48 ^{+0.79} _{-1.09}	175 ⁺³⁹ ₋₃₅	175	0.91
6 - 16	18.8 - 20.3	1	4	1	2	0	19.743 ^{+0.047} _{-0.035}	1.49 ^{+0.10} _{-0.10}	1.46 ^{+0.42} _{-0.83}	175 ⁺⁴⁰ ₋₃₅	175	0.85
6 - 16	18.8 - 20.3	1	3	1	3	0	19.758 ^{+0.041} _{-0.035}	1.52 ^{+0.08} _{-0.08}	1.68 ^{+0.50} _{-0.89}	175 ⁺³⁹ ₋₃₅	175	0.84
6 - 16	18.8 - 20.3	1	3	1	3	1	19.734 ^{+0.059} _{-0.052}	1.54 ^{+0.09} _{-0.11}	1.39 ^{+0.54} _{-1.03}	176 ⁺³⁹ ₋₃₅	175	0.90
$\Delta k = 7$												
M	ω^2	n_{r_0}	n_{r_1}	n_i	m_r	m_i	ω_c^2	ν	y	χ^2	μ	Γ_q
8 - 20	-3.5 - -2.75	2	2	1	1	0	-3.325 ^{+0.070} _{-0.115}	1.59 ^{+0.23} _{-0.29}	0.83 ^{+0.33} _{-0.35}	162 ⁺³⁸ ₋₃₃	162	0.51
8 - 20	-3.5 - -2.75	3	2	1	1	0	-3.325 ^{+0.069} _{-0.101}	1.61 ^{+0.19} _{-0.33}	0.84 ^{+0.31} _{-0.34}	161 ⁺³⁸ ₋₃₄	161	0.78
8 - 20	-3.5 - -2.75	2	3	1	1	0	-3.330 ^{+0.067} _{-0.099}	1.55 ^{+0.22} _{-0.47}	0.81 ^{+0.29} _{-0.32}	161 ⁺³⁷ ₋₃₄	161	0.77
8 - 20	-3.5 - -2.75	2	2	1	2	0	-3.334 ^{+0.070} _{-0.116}	1.61 ^{+0.20} _{-0.16}	0.80 ^{+0.33} _{-0.33}	162 ⁺³⁸ ₋₃₄	161	0.79
8 - 20	-3.5 - -2.75	2	2	1	1	1	-3.333 ^{+0.075} _{-0.132}	1.63 ^{+0.42} _{-0.55}	0.80 ^{+0.38} _{-0.35}	161 ⁺³⁸ ₋₃₃	161	0.50

Table A.3: Critical parameter ω_c^2 and ν for pure mass disorder transitions $\Delta k = 1, 7$ and 10 computed from FSS obtained in the given M and ω^2 ranges and with the orders of the expansion given by n_{r_0} , n_{r_1} , n_i , m_r and m_i . The minimised χ^2 value, the degrees of freedom μ and the resulting goodness-of-fit parameter Γ_q are also shown for each fit. Extended table includes higher order fits used for stability analysis.

$\Delta k = 1$												
M	ω	n_{r_0}	n_{r_1}	n_i	m_r	m_i	ω_c	ν	y	χ^2	μ	Γ_q
10-20	3.529 - 3.55	3	3	1	1	2	$3.540^{+0.001}_{-0.001}$	$1.47^{+0.15}_{-0.05}$	$4.05^{+0.24}_{-0.23}$	157^{+39}_{-34}	156	0.49
10-20	3.529 - 3.55	4	3	1	1	2	$3.540^{+0.001}_{-0.001}$	$1.48^{+0.06}_{-0.04}$	$4.04^{+0.24}_{-0.24}$	155^{+36}_{-33}	155	0.47
10-20	3.529 - 3.55	3	4	1	1	2	$3.540^{+0.001}_{-0.001}$	$1.45^{+0.17}_{-0.06}$	$4.03^{+0.25}_{-0.27}$	156^{+37}_{-33}	155	0.51
10-20	3.529 - 3.55	3	3	1	2	2	$3.540^{+0.001}_{-0.001}$	$1.45^{+0.10}_{-0.04}$	$3.99^{+0.24}_{-0.25}$	155^{+37}_{-33}	155	0.51
10-20	3.529 - 3.55	3	3	1	1	3	$3.540^{+0.001}_{-0.001}$	$1.39^{+0.04}_{-0.04}$	$4.01^{+0.24}_{-0.22}$	156^{+38}_{-34}	155	0.93
$\Delta k = 10$												
M	ω	n_{r_0}	n_{r_1}	n_i	m_r	m_i	ω_c	ν	y	χ^2	μ	Γ_q
6-16	4.335 - 4.506	2	3	1	2	0	$4.441^{+0.008}_{-0.009}$	$1.52^{+0.15}_{-0.53}$	$1.28^{+0.66}_{-0.93}$	199^{+41}_{-38}	199	0.87
6-16	4.335 - 4.506	3	3	1	2	0	$4.441^{+0.008}_{-0.008}$	$1.49^{+0.19}_{-0.43}$	$1.26^{+0.62}_{-0.97}$	198^{+42}_{-38}	198	0.86
6-16	4.335 - 4.506	2	4	1	2	0	$4.441^{+0.007}_{-0.010}$	$1.52^{+0.15}_{-0.54}$	$1.30^{+0.70}_{-0.97}$	198^{+42}_{-37}	198	0.87
6-16	4.335 - 4.506	2	3	1	3	0	$4.441^{+0.008}_{-0.005}$	$1.52^{+0.16}_{-0.11}$	$1.29^{+0.49}_{-1.06}$	199^{+42}_{-37}	198	0.91
6-16	4.335 - 4.506	2	3	1	2	1	$4.438^{+0.009}_{-0.012}$	$1.41^{+0.26}_{-0.61}$	$1.13^{+0.72}_{-0.90}$	198^{+41}_{-37}	198	0.90
$\Delta k = 7$												
M	ω	n_{r_0}	n_{r_1}	n_i	m_r	m_i	ω_c	ν	y	χ^2	μ	Γ_q
8-20	-1.87 - -1.66	2	2	1	1	0	$-1.825^{+0.019}_{-0.033}$	$1.60^{+0.21}_{-0.19}$	$0.81^{+0.34}_{-0.32}$	162^{+38}_{-34}	162	0.79
8-20	-1.87 - -1.66	3	2	1	1	0	$-1.825^{+0.020}_{-0.032}$	$1.60^{+0.22}_{-0.19}$	$0.82^{+0.32}_{-0.34}$	161^{+39}_{-34}	161	0.78
8-20	-1.87 - -1.66	2	3	1	1	0	$-1.825^{+0.020}_{-0.033}$	$1.60^{+0.21}_{-0.20}$	$0.81^{+0.33}_{-0.34}$	161^{+38}_{-34}	161	0.78
8-20	-1.87 - -1.66	2	2	1	2	0	$-1.826^{+0.019}_{-0.032}$	$1.62^{+0.18}_{-0.13}$	$0.80^{+0.33}_{-0.32}$	161^{+37}_{-33}	161	0.77
8-20	-1.87 - -1.66	2	2	1	1	1	$-1.826^{+0.020}_{-0.034}$	$1.61^{+0.35}_{-0.55}$	$0.80^{+0.35}_{-0.34}$	161^{+39}_{-33}	161	0.78

Table A.4: Critical parameter ω_c and ν for pure mass disorder transitions $\Delta k = 1, 7$ and 10 computed from FSS obtained in the given M and ω ranges and with the orders of the expansion given by n_{r_0} , n_{r_1} , n_i , m_r and m_i . The minimised χ^2 value, the degrees of freedom μ and the resulting goodness-of-fit parameter Γ_q are also shown for each fit. Extended table includes higher order fits used for stability analysis.

mean with a single symmetric standard error. To retain unsymmetric error bars Eqn. (9.3) is re-written so that the contribution of the weights for negative and positive errors is doubled to match the size of the new set as

$$\sigma_y^+ = \sqrt{\frac{1}{2 \cdot \sum_+ w_i}} \quad \text{and} \quad \sigma_y^- = \sqrt{\frac{1}{2 \cdot \sum_- w_i}}, \quad (9.4)$$

where \sum_+ and \sum_- represent summations over indexes i that contain positive and negative error estimates, respectively.

Bibliography

- [1] R. C. Chu, R. E. Simons, M. J. Ellsworth, R. R. Schmidt, and V. Cozzolino. Review of cooling technologies for computer products. *IEEE Trans. Device Mater. Reliab.*, 4:568, 2004.
- [2] W. Kim, R. Wang, and A. Majumdar. Nanostructuring expands thermal limits. *Nanotoday*, 2:40, 2007.
- [3] H. J. Goldsmid. *Electronic Refrigeration*. Pion, London, 1986.
- [4] A. F. Ioffe. *Semiconductor Thermoelements and Thermoelectric Cooling*. Infosearch Ltd., London, 1958.
- [5] M. S. Dresselhaus, G. Chen, M. Y. Tang, R. Yang, H. Lee, D. Wang, Z. Ren, J. Fleurial, and P. Gogna. New directions for low-dimensional thermoelectric materials. *Adv. Mater.*, 19:1043, 2007.
- [6] G. Slack. *CRC Handbook of Thermoelectrics*. CRC Press, Boca Raton, FL, 1995.
- [7] W. Kim, J. Zide, A.C. Gossard, D. Klenov, S. Stemmer, A. Shakouri, and A. Majumdar. Thermal conductivity reduction and thermoelectric figure of merit increase by embedding nanoparticles in crystalline semiconductors. *Phys. Rev. Lett.*, 96:045901, 2006.
- [8] A. Balandin and K.L. Wang. Significant decrease of the lattice thermal conductivity due to phonon confinement in a free-standing semiconductor quantum well. *Phys. Rev. B*, 58:1544, 1998.
- [9] R. Venkatasubramanian. Lattice thermal conductivity reduction and phonon localization like behaviour in superlattice structures. *Phys. Rev. B*, 61:3091, 2000.
- [10] *Thermal Conductivity Reduction Mechanisms in Superlattices*, 22nd International Conference on Thermoelectrics, 445 Hoes Lane, Piscataway, NJ 08855-1331, 2003. IEEE Xplore.
- [11] T. Tritt. *Thermal Conductivity: Theory, Properties, and Applications*. Springer, 233 Spring Street, New York, NY 10013, 2004.

- [12] I.M. Lifshitz and A.M. Kosevich. The dynamics of a crystal lattice with defects. *Journal of Physics: USSR*, 8:217, 1954.
- [13] K.M. Katika and L. Pilon. The effect of nanoparticles on the thermal conductivity of crystalline thin films at low temperatures. *J. Appl. Phys.*, 103:114308, 2008.
- [14] D. Walton and E.J. Lee. Scattering of phonons by a square-well potential and the effect of colloids on the thermal conductivity. II. theoretical. *Phys. Rev.*, 157:724, 1967.
- [15] G.P. Srivastava. *The Physics of Phonons*. Taylor & Francis Group, 270 Madison Avenue, New York, 1990.
- [16] P. D. Maycock. Thermal conductivity of silicon, germanium, III-V compounds and III-V alloys. *Solid State Electronics*, 10:161, 1967.
- [17] P. W. Anderson. Absence of diffusion in certain random lattices. *Phys. Rev.*, 109:1492, 1958.
- [18] Juliette Billy, Vincent Josse, Zhanchun Zuo, Alain Bernard, Ben Hambrecht, Pierre Lugan, David Clement, Laurent Sanchez-Palencia, Philippe Bouyer, and Alain Aspect. Direct observation of Anderson localization of matter waves in a controlled disorder. *Nature*, 453:891, 2008.
- [19] B. Kramer and A. MacKinnon. Localization: theory and experiment. *Rep. Prog. Phys.*, 56:1469, 1993.
- [20] Ferdinand Evers and Alexander D. Mirlin. Anderson transitions. *Rev. Mod. Phys.*, 80:1355, 2008.
- [21] N. F. Mott. Conduction in non-crystalline systems. I. Localized electronic states in disordered systems. *Phil. Mag.*, 17:1259, 1968.
- [22] J. M. Ziman. Localization of electrons in ordered and disordered systems II. bound bands. *J. Phys. C*, 2:1230, 1969.
- [23] D. P. Belanger and A. P. Young. The random field Ising model. *J. Magn. Mater.*, 100:272, 1991.
- [24] J. M. Ziman. *Models of Disorder*. Cambridge University Press, Cambridge, UK, 1979.
- [25] B. Bulka, M. Schreiber, and B. Kramer. Localization, quantum interference, and the metal-insulator transition. *Z. Phys. B*, 66:21, 1987.
- [26] P. Cain, R. A. Römer, and M. Schreiber. Phase diagram of the three-dimensional Anderson model of localization with random hopping. *Ann. Phys. (Leipzig)*, 8:SI33, 1999. ArXiv: cond-mat/9908255.

- [27] M. E. Fisher. Renormalization group theory: Its basis and formulation in statistical physics. *Rev. Mod. Phys.*, 709, 1998.
- [28] D. J. Thouless. Electrons in disordered systems and the theory of localization. *Phys. Rep.*, 13:93, 1974.
- [29] E. Abrahams, P. W. Anderson, D. C. Licciardello, and T. V. Ramakrishnan. Scaling theory of localization: Absence of quantum diffusion in two dimensions. *Phys. Rev. Lett.*, 42:673, 1979.
- [30] F. J. Wegner. Corrections to scaling laws. *Phys. Rev. B*, 5:4529, 1972.
- [31] F. Wegner. Electrons in disordered systems. Scaling near the mobility edge. *Z. Phys. B*, 25:327, 1976.
- [32] F. Wegner. The mobility edge problem: continuous symmetry and a conjecture. *Z. Phys. B*, 35:207, 1979.
- [33] S. John, H. Sompolinsky, and M. J. Stephen. Localization in a disordered elastic medium near two dimensions. *Phys. Rev. B*, 27:5592, 1983.
- [34] R. Landauer. Electrical resistance of disordered one-dimensional lattices. *Phil. Mag.*, 21:863, 1970.
- [35] Martin Janssen. Statistics and scaling in disordered mesoscopic electron systems. *Phys. Rep.*, 295:1, 1998.
- [36] R. A. Römer and M. Schreiber. *The Anderson Transition and its Ramifications — Localisation, Quantum Interference, and Interactions*, volume 630 of *Lecture Notes in Physics*, chapter Numerical investigations of scaling at the Anderson transition, pages 3–19. Springer, Berlin, 2003.
- [37] K. Slevin and T. Ohtsuki. Corrections to scaling at the Anderson transition. *Phys. Rev. Lett.*, 82:382, 1999. ArXiv: cond-mat/9812065.
- [38] S. Waffenschmidt, C. Pfleiderer, and H. v. Löhneysen. Critical behavior of the conductivity of Si:P at the metal-insulator transition under uniaxial stress. *Phys. Rev. Lett.*, 83:3005, 1999. ArXiv: cond-mat/9905297.
- [39] A. B. Fowler, G. L. Timp, J. J. Wainer, and R. A. Webb. Observation of resonant tunnelling in silicon inversion layers. *Phys. Rev. Lett.*, 57:138, 1986.
- [40] G. J. Dolan, J. C. Licini, and D. J. Bishop. Quantum interference effects in lithium ring arrays. *Phys. Rev. Lett.*, 56:1493, 1986.
- [41] M. A. Paalanen and G. A. Thomas. Experimental tests of localization in semiconductors (metal-insulator transition). *Helv. Phys. Acta*, 56:27, 1983.
- [42] H. P. Wei, D. C. Tsui, M. A. Paalanen, and A. M. M. Pruisken. Experiments on delocalization and universality in the integral quantum Hall effect. *Phys. Rev. Lett.*, 61:1294, 1988.

- [43] A. M. M. Pruisken. Universal singularities in the integral quantum Hall effect. *Phys. Rev. Lett.*, 61:1297, 1988.
- [44] A. M. M. Pruisken. *The Quantum Hall Effect*. Springer, Berlin, 1987.
- [45] S. John. Electromagnetic absorption in a disordered medium near a photon mobility edge. *Phys. Rev. Lett.*, 53:2169, 1984.
- [46] S. He and J. D. Maynard. Detailed measurements of inelastic scattering in Anderson localization. *Phys. Rev. Lett.*, 57:3171, 1986.
- [47] E. N. Economou and C. M. Soukoulis. Calculation of optical transport and localization quantities. *Phys. Rev. B*, 40:7977, 1989.
- [48] D. S. Wiersma, P. Bartolini, A. Lagendjik, and R. Righini. Localization of light in a disordered medium. *Nature*, 390:671, 1997.
- [49] Hefei Hu, A. Strybulevych, J. H. Page, S. E. Skipetrov, and B. A. Van Tiggelen. Localization of ultrasound in a three-dimensional elastic network. *Nature Physics*, 4:945, 2008.
- [50] Giacomo Roati, Chiara D’Errico, Leonardo Fallani, Marco Fattori, Chiara Fort, Matteo Zaccanti, Giovanni Modugno, Michele Modugno, and Massimo Inguscio. Anderson localization of a non-interacting Bose-Einstein condensate. *Nature*, 453:895, 2008.
- [51] P Bouyer. Quantum gases and optical speckle: a new tool to simulate disordered quantum systems. *Reports on Progress in Physics*, 73:062401, 2010.
- [52] F. C. Brown. *The Physics of Solids*. W. A. Benjamin, Inc., New York, 1967.
- [53] E. Anderson, Z. Bai, C. Bischof, S. Blackford, J. Demmel, J. Dongarra, J. Du Croz, A. Greenbaum, S. Hammarling, A. McKenney, and D. Sorensen. *LAPACK Users’ Guide*. Society for Industrial Mathematics, Philadelphia, PA., 1987.
- [54] O. Schenk, M. Bollhöfer, and R. Römer. On large scale diagonalization techniques for the Anderson model of localization. *SIAM Journal of Sci. Comp.*, 28:963, 2006.
- [55] Richard B. Lehoucq, Danny C. Sorensen, and C. Yang. *Arpack User’s Guide: Solution of Large-Scale Eigenvalue Problems With Implicitly Restarted Arnoldi Methods*. Society for Industrial Mathematics, Philadelphia, PA., 1998.
- [56] W. E. Arnoldi. The principle of minimized iterations in the solution of the matrix eigenvalue problem. *Quarterly of Applied Mathematics*, 9:17, 1951.
- [57] C. Lanczos. An iteration method for the solution of the eigenvalue problem of linear differential and integral operators. *J. Res. Nat. Bur. Standards.*, 45:255, 1950.

- [58] Y. Saad. *Iterative methods for sparse linear systems*. SIAM, Philadelphia, 2003.
- [59] O. Schenk, K. Gärtner, W. Fichtner, and A. Stricker. Pardiso: A high-performance serial and parallel sparse linear solver in semiconductor device simulation. *Journal of Future Generation Computers Systems*, 18:69, 2001.
- [60] M. Bollhöfer and Y. Notay. JADAMILU: a software code for computing selected eigenvalues of large sparse symmetric matrices. *Comp. Phys. Comm.*, 177:951, 2007.
- [61] A. I. Boukai, Y. Bunimovich, J. Tahir-Kheli, J. Yu, W. A. Goddard, and J. R. Heath. Silicon nano wires as efficient thermoelectric materials. *Nature*, 451:168, 2008.
- [62] C. B. Vining. Desperately seeking silicon. *Nature*, 451:132, 2008.
- [63] P. Dean and M.D. Bacon. The nature of vibrational modes in disordered systems. *Proc. Phys. Soc.*, 81:642, January 1963.
- [64] J.R. Hook and H.E. Hall. *Solid State Physics*. John Wiley & Sons Ltd., The Atrium, Southern Gate, Chichester, PO19 8SQ, 2nd edition edition, 1991.
- [65] R. J. Bell. The dynamics of disordered lattices. *Rep. Prog. Phys.*, 35:1315, 1972.
- [66] R.W. Clough and J. Penzien. *Dynamics of Structures*. McGraw-Hill, Inc., New York, 2nd edition edition, 1993.
- [67] J. Canisius and J.L. van Hemmen. Localization of phonons. *J. Phys. C*, 18:4873, 1985.
- [68] Y. Ezzahri, S. Grauby, J.M. Rampnoux, H. Michel, G. Pernot, W. Claeys, S. Dilhaire, C. Rossignol, G. Zeng, and A. Shakouri. Coherent phonons in Si/SiGe superlattices. *Phys. Rev. B*, 75:195309, 2007.
- [69] C. Kittel. *Introduction to Solid State Physics*. John Wiley & Sons Ltd., The Atrium, Southern Gate, Chichester, PO19 8SQ, 7th edition edition, 1996.
- [70] L. Li and X. Yang. Phonon spectra of a Fibonacci chain. *Physica B*, 403:2888, 2008.
- [71] D. Huang, G. Gumbs, Y. Zhao, and G.W. Auner. Optical-phonon transport and localization in periodic and Fibonacci polar-semiconductor superlattices. *Phys. Lett. A*, 200:459, 1995.
- [72] W. Schirmacher, G. Diezemann, and C. Ganter. Harmonic vibrational excitations in disordered solids and the boson peak. *Phys. Rev. Lett.*, 81:136, 1998.

- [73] S. N. Taraskin, Y. L. Loh, G. Natarajan, and S. R. Elliott. Origin of the boson peak in systems with lattice disorder. *Phys. Rev. Lett.*, 86:1255, 2001.
- [74] Viktor G Veselago. The electrodynamics of substances with simultaneously negative values of ϵ and $\epsilon\epsilon$? *Soviet Physics Uspekhi*, 10:509, 1968.
- [75] Zhengyou Liu, Xixiang Zhang, Yiwei Mao, Y.Y. Zhu, Zhiyu Yang, C.T. Chan, and Ping Sheng. Locally resonant sonic materials. *Science*, 289:1734, 2000.
- [76] Z. G. Wang, S. H. Lee, C. K. Kim, C. M. Park, K. Nahm, and S. A. Nikitov. Acoustic wave propagation in one-dimensional phononic crystals containing Helmholtz resonators. *J. Appl. Phys.*, 103:064907, 2008.
- [77] I.F. Herrera-Gonzalez, F.M. Izrailev, and L. Tessieri. Anomalous thermal properties of a harmonic chain with correlated isotopic disorder. *Europhys. Lett.*, 90:14001, 2010.
- [78] V. I. Oseledec. A multiplicative ergodic theorem. Ljapunov characteristic numbers for dynamical systems. *Trans. Moscow Math. Soc.*, 19:197, 1968.
- [79] J.J. Ludlam, T.O. Stadelmann, S.N. Taraskin, and S.R. Elliott. Numerical analysis of the vibrational eigenmodes of a 2D disordered lattice. *Journal of Non-Crystalline Solids*, 293:676, 2001.
- [80] Stefanie Russ. Scaling of the localization length in linear electronic and vibrational systems with long-range correlated disorder. *Phys. Rev. B*, 66:012204, 2002.
- [81] J.J Ludlam, S.N. Taraskin, and S.R. Elliott. Disorder induced vibrational localization. *Phys. Rev. B*, 67:132203, 2003.
- [82] H. Shima, S. Nishino, and T. Nakayama. Peculiar behaviors of excited modes in harmonic chains with correlated disorder. *J. Phys.: Conf. Ser.*, 92:012156, 2007.
- [83] R. A. Römer and H. Schulz-Baldes. Weak disorder expansion for localization lengths of quasi-1d systems. *Europhys. Lett.*, 68:247, 2004.
- [84] M. Yamanaka, Y. Avishai, and M. Kohmoto. Universality class in the one-dimensional localization problem. *Phys. Rev. B*, 54:228, 1996.
- [85] L. I. Deych, D. Zaslavsky, and A. A. Lisyansky. Statistics of the Lyapunov exponent in 1D random periodic-on-average systems. *Phys. Rev. Lett.*, 81, 1998.
- [86] J.-L. Pichard and G. Sarma. Finite-size scaling approach to Anderson localisation. *J. Phys. C*, 14:L127, 1981.
- [87] M. Schreiber. Numerical evidence for power-law localisation in weakly disordered systems. *J. Phys.: Condens. Matter*, 18:2493, 1985.

- [88] M. Born and K. Huang. *Dynamical Theory of Crystal Lattices*. Oxford, Univ. Press, New York, 1954.
- [89] Shechao Feng and Pabitra N. Sen. Percolation on elastic networks: New exponent and threshold. *Phys. Rev. Lett.*, 52:216, 1984.
- [90] Yasuyuki Akita and Tomi Ohtsuki. Anderson transition of three dimensional phonon modes. *J. Phys. Soc. Jap.*, 67:2954, 1998.
- [91] M. Born and T. Von Kármán. Boundary conditions. *Physik. Zeits.*, 13:297, 1912.
- [92] J. M. Ziman. *Electrons and Phonons*. Clarendon Press, Oxford, 1967.
- [93] Louella J. Vasquez, Alberto Rodriguez, and Rudolf A. Römer. Multifractal analysis of critical states in the 3D Anderson model. I. symmetry relation under typical averaging. *Phys. Rev. B*, 78:195106, 2008. ArXiv: cond-mat:0807.2217v1.
- [94] J J Ludlam, S N Taraskin, S R Elliot, and D A Drabold. Universal features of localized eigenstates in disordered systems. *J. Phys.: Condens. Matter*, 17:L321, 2005.
- [95] A. D. Mirlin, Y. V. Fyodorov, A. Mildenerger, and F. Evers. Exact relations between multifractal exponents at the Anderson transition. *Phys. Rev. Lett.*, 97:046803, 2006.
- [96] L. Van Hove. The occurrence of singularities in the elastic frequency distribution of a crystal. *Phys. Rev.*, 89:1189, 1953.
- [97] F. Yonezawa and K. Morigaki. Coherent potential approximation: Basic concepts and applications. *Prog. Theor. Phys. Supplement*, 53:1, 1973.
- [98] P. Sheng. *Introduction to wave scattering, localization and mesoscopic phenomena*. Springer series in materials science. Springer, 2006.
- [99] J.W. Kantelhardt, A. Bunde, and L. Schweitzer. Extended fractons and localized phonons on percolation clusters. *Phys. Rev. Lett.*, 81:4907, 1998.
- [100] W. Schirmacher, C. Tomaras, B. Schmid, G. Viliani, G. Baldi, G. Ruocco, and T. Scopigno. Vibrational excitations in systems with correlated disorder. *Phys. Stat. Sol. C*, 5:862, 2008.
- [101] M. Antezza, Y. Castin, and D. A. W. Hutchinson. Quantitative study of two- and three-dimensional strong localization of matter waves by atomic scatterers. *Phys. Rev. A*, 82:043602, 2010.
- [102] Abhishek Chaudhuri, Anupam Kundu, Dibyendu Roy, Abhishek Dhar, Joel L. Lebowitz, and Herbert Spohn. Heat transport and phonon localization in mass-disordered harmonic crystals. *Phys. Rev. B*, 81:064301, Feb 2010.

- [103] T. Horigucho. Lattice Green's function for the simple cubic lattice. *J. Phys. Soc. Japan*, 30:1261, 1971.
- [104] G. S. Joyce. On the simple cubic lattice Green function. *Phil. Trans. R. Soc. A*, 273:583, 1973.
- [105] K. Heun. Zur Theorie der Riemann'schen Functionen zweiter Ordnung mit vier Verzweigungspunkten. *Math. Annln.*, 33:161, 1889.
- [106] W. H. Press, S. A. Teukolsky, W. T. Vetterling, and B. P. Flannery. *Numerical recipes in C: The Art of Scientific Computing*. Cambridge University Press, New York, 2002.
- [107] M. Wołoszyn and A. Z. Maksymowicz. Coherent potential approximation technique in a simple example of resistivity calculations for binary alloys. *TASK quarterly*, 6:4, 2002.
- [108] A. D. Zdetsis, C. M. Soukoulis, E. N. Economou, and G. S. Grest. Localization in two- and three-dimensional systems away from the band center. *Phys. Rev. B*, 32:7811, 1985.
- [109] M. Wagener and W. Schirmacher. Effective medium approximation for vibrational excitations in disordered solids. *Journal of Non-Crystalline Solids*, 145:136, 1992.
- [110] J. Jäckle. Low frequency Raman scattering in glasses. In W.A. Phillips, editor, *Amorphous Solids: Low-Temperature Properties*, page 135. Springer-Verlag, Berlin, 1981.
- [111] P. Flubacher, A. J. Leadbetter, J. A. Morrison, and B. P. Stoicheff. The low-temperature heat capacity and the Raman and Brillouin spectra of vitreous silica. *J. Phys. Chem. Solids*, 12:53, 1959.
- [112] V. Illyin, I. Procaccia, I. Regev, and Y. Shokef. Randomness-induced redistribution of vibrational frequencies in amorphous solids. *Phys. Rev. B*, 80:174201, 2009.
- [113] P. M. Derlet, R. Maaß, and J. F. Löffler. The boson peak of model glass systems and its relation to atomic structure. *Eur. Phys. J. B*, 85:148, 2012.
- [114] A. I. Chumakov, G. Monaco, A. Monaco, W. A. Crichton, A. Bosak, R. Ruffer, A. Meyer, F. Kargl, L. Comez, D. Fioretto, H. Giefers, S. Roitsch, G. Wortmann, M. H. Manghnani, A. Hushur, Q. Williams, J. Balogh, K. Parliński, P. Jochym, and P. Piekarczyk. Equivalence of the boson peak in glasses to the transverse acoustic Van Hove singularity in crystals. *Phys. Rev. Lett.*, 106:225501, 2011.
- [115] H. Shintani and H. Tanaka. Universal link between the boson peak and transverse phonons in glass. *Nature Mater.*, 7:870, 2008.

- [116] A. I. Chumakov, I. Sergueev, U. van Bürck, W. Schirmacher, T. Asthalter, R. Rüffer, O. Leupold, and W. Petry. Collective nature of the boson peak and universal transboson dynamics of glasses. *Phys. Rev. Lett.*, 92:245508, 2004.
- [117] C. Tomaras, B. Schmid, and W. Schirmacher. Replica field theory for anharmonic sound attenuation in glasses. *J. Non-Cryst. Solids.*, 357:542, 2011.
- [118] A. G. Kalampounias, S. N. Yannopoulos, and G. N. Papatheodorou. A high-temperature Raman spectroscopic investigation of the potassium tetrasilicate in glassy, supercooled, and liquid states. *J. Chem. Phys.*, 125:164502, 2006.
- [119] S. Alexander. Vibrations of fractals and scattering of light from aerogels. *Phys. Rev. B*, 40:7953, 1989.
- [120] W. Schirmacher and G. Diezemann. Propagation and localisation of vibrational modes in 3-dimensional disordered systems: The binary force constant model. *Ann. Phys. (Leipzig)*, 8:727, 1999.
- [121] J.L. Feldman, M.D. Kluge, P.B. Allen, and F. Wooten. Thermal conductivity and localization in glasses: numerical study of a model of amorphous silicon. *Phys. Rev. B*, 48:12589, November 1993.
- [122] Jan W. Kantelhardt, Stefanie Russ, and Armin Bunde. Excess modes in the vibrational spectrum of disordered systems and the boson peak. *Phys. Rev. B*, 63:064302, 2001.
- [123] T. Scopigno, J.B. Suck, R. Angelini, F. Albergamo, and G. Ruocco. High-frequency dynamics in metallic glasses. *Phys. Rev. Lett.*, 96:135501, 2006.
- [124] S.N. Taraskin, J.J. Ludlam, G. Natarajan, and S.R. Elliott. Propagation, hybridization and localization of vibrational excitations in disordered materials. *Philosophical Magazine B*, 82:197, 2002.
- [125] W. Schirmacher and M. Wagener. Vibrational anomalies and phonon localization in glasses. *Solid State Communications*, 86:597, 1993.
- [126] T. Nakayama, K. Yakubo, and R. L. Orbach. Dynamical properties of fractal networks: Scaling, numerical simulations, and physical realizations. *Rev. Mod. Phys.*, 66:381, 1994.
- [127] A. Feher, I. M. Yurkin, L. I. Deich, M. Orendáč, and I. D. Turyanitsa. The comparative analysis of some low-frequency vibrational state density models of the amorphous materials - applied to the As_2S_3 glass. *Physica B*, 194:395, 1994.
- [128] S. N. Taraskin and S. R. Elliott. Ioffe-Regel crossover for plane-wave vibrational excitations in vitreous silica. *Phys. Rev. B*, 61:12031, 2000.
- [129] S. K. Sarkar, G. S. Matharoo, and A. Pandey. Universality in the vibrational spectra of single-component amorphous clusters. *Phys. Rev. Lett.*, 92:215503, 2004.

- [130] S Taraskin and S Elliott. Disorder-induced zero-energy spectral singularity for random matrices with correlations. *Phys. Rev. B*, 65:052201, 2002.
- [131] H. Grussbach and M. Schreiber. Determination of the mobility edge in the Anderson model of localization in three dimensions by multifractal analysis. *Phys. Rev. B*, 51:663, 1995.
- [132] A. MacKinnon and B. Kramer. One-parameter scaling of localization length and conductance in disordered systems. *Phys. Rev. Lett.*, 47:1546, 1981.
- [133] B. Kramer, A. Broderix, A. MacKinnon, and M. Schreiber. The Anderson transition: new numerical results for the critical exponents. *Physica A*, 167:163, 1990.
- [134] Shanshan Yao, Xiaoming Zhou, and Gengkai Hu. Experimental study on negative effective mass in a 1d mass-spring system. *New J. of Phys.*, 10:043020, 2008.
- [135] B. J. Huang and Ten-Ming Wu. Localization-delocalization transition in hessian matrices of topologically disordered systems. *Phys. Rev. E*, 79:041105, 2009.
- [136] R. A. Horn and C. R. Johnson. *Matrix Analysis*. Cambridge University Press, New York, 1985.
- [137] T. Edwards. Parallelising the transfer-matrix method using graphics processors. Master's thesis, University of Warwick, 2012.
- [138] Alberto Rodriguez, Louella J. Vasquez, Keith Slevin, and Rudolf A. Römer. Critical parameters from a generalized multifractal analysis at the Anderson transition. *Phys. Rev. Lett.*, 105:046403, 2010.
- [139] F. Milde, R. A. Römer, M. Schreiber, and V. Uski. Critical properties of the metal-insulator transition in anisotropic systems. *Eur. Phys. J. B*, 15:685, 2000. ArXiv: cond-mat/9911029.
- [140] W. H. Press, B. P. Flannery, S. A. Teukolsky, and W. T. Vetterling. *Numerical Recipes in FORTRAN*. Cambridge University Press, Cambridge, 2nd edition, 1992.
- [141] F.A.B.F. de Moura and F. Domínguez-Adame. Extended modes and energy dynamics in two-dimensional lattices with correlated disorder. *Eur. Phys. J. B*, 66:165, 2008.
- [142] A. MacKinnon. Critical exponents for the metal-insulator transition. *J. Phys.: Condens. Matter*, 6:2511, 1994.
- [143] Cecile Monthus and Thomas Garel. Anderson localization of phonons in dimension $d=1,2,3$: Finite-size properties of the inverse participation ratios and eigenstates. *Phys. Rev. B*, 81:224208, 2010.

- [144] P. Biswas, P. Cain, R. A. Römer, and M. Schreiber. Off-diagonal disorder in the Anderson model of localization. *phys. stat. sol. (b)*, 218:205, 2000. ArXiv: cond-mat/0001315.
- [145] P. Cain. Das Anderson-Modell der Lokalisierung mit nichtdiagonaler Unordnung. Master's thesis, Technische Universität Chemnitz, December 1998.
- [146] T. Kawarabayashi, B. Kramer, and T. Ohtsuki. Anderson transitions in three-dimensional disordered systems with randomly varying magnetic flux. *Phys. Rev. B*, 57:11842, 1998.
- [147] M. L. Mehta. *Random Matrices and the Statistical Theory of Energy levels*. Academic Press, New York, 1991.
- [148] F. Haake. *Quantum Signatures of Chaos*. Springer, Berlin, 2nd edition, 1992.
- [149] C. E. Porter. *Statistical Theories of Spectra: Fluctuations*. Academic Press, New York, 1965.
- [150] F. J. Dyson. Statistical theory of the energy levels of complex systems. I. *J. Math. Phys.*, 3:140, 1962.
- [151] Y. V. Fyodorov and A. D. Mirlin. Statistical properties of eigenfunctions of random quasi 1d one-particle hamiltonians. *Int. J. Mod. Phys. B*, 8:3795, 1994.
- [152] V. Uski, B. Mehlig, R. A. Römer, and M. Schreiber. An exact diagonalization study of rare events in disordered conductors. *Phys. Rev. B*, 62:R7699, 2000.
- [153] E. P. Wigner. On the statistical distribution of the widths and spacings of nuclear resonance levels. *Proc. Camb. Phil. Soc.*, 47:790, 1951.
- [154] A. D. Mirlin. Statistics of energy levels and eigenfunctions in disordered systems. *Phys. Rep.*, 326:259, 2000.
- [155] Branislav K. Nikolić. Statistical properties of eigenstates in three-dimensional mesoscopic systems with off-diagonal or diagonal disorder. *Phys. Rev. B*, 64:014203, 2001.
- [156] C. E. Porter and R. G. Thomas. Fluctuations of nuclear reaction widths. *Phys. Rev.*, 104:483, 1956.
- [157] Alberto Rodriguez, Louella J. Vasquez, and Rudolf A. Römer. Multifractal analysis of critical states in the 3D Anderson model. II. Symmetry relation under ensemble averaging. *Phys. Rev. B*, 78:195107, 2008. cond-mat:0807.2209v1.
- [158] M. Janssen. Multifractal analysis of broadly-distributed observables at criticality. *Int. J. Mod. Phys. B*, 8:943, 1994.

- [159] Matthew S. Foster, Shinsei Ryu, and Andreas W. W. Ludwig. Termination of typical wave-function multifractal spectra at the Anderson metal-insulator transition: Field theory description using the functional renormalization group. *Phys. Rev. B*, 80:075101, 2009.
- [160] B.B. Mandelbrot. *The Fractal Geometry of Nature*. W.H. Freeman, 1983.
- [161] H. V. Koch. *Classics on Fractals*. Addison-Wesley, Reading MA, 1993.
- [162] B. Veress and J. Szigethy, editors. *Horizons in Earth Science Research*, volume 3. Nova Science Pub Incorporated, Hauppauge, NY, USA, 2011. arXiv:1104.4991v1.
- [163] T. Nakayama and K. Yakubo. *Fractal Concepts in Condensed Matter Physics*. Springer, Berlin, Germany, 2003.
- [164] D. Harte. *Multifractals: Theory and Applications*. Chapman & Hall, London, 2001.
- [165] T. C. Halsey, M. H. Jensen, L. P. Kadanoff, I. Procaccia, and B. I. Shraiman. Fractal measures and their singularities: The characterization of strange sets. *Phys. Rev. A*, 33:2, 1986.
- [166] F. J. Solis and L. Tao. Lacunarity of random fractals. *Phys. Rev. A*, 228:351, 1997.
- [167] F. Wegner. Four-loop-order beta-function of nonlinear sigma-models in symmetric spaces. *Nucl. Phys. B*, 316:663, 1989.
- [168] A. W. W. Ludwig, M. P. A. Fisher, R. Shankar, and G. Grinstein. Integer quantum Hall transition: An alternative approach and exact results. *Phys. Rev. B*, 50:7526, 1994.
- [169] Alberto Rodriguez, Louella J. Vasquez, Keith Slevin, and Rudolf A. Römer. Multifractal finite-size scaling and universality at the Anderson transition. *Phys. Rev. B*, 84:134209, 2011.
- [170] F. Evers, A. Mildenberg, and A. D. Mirlin. Quantum Hall effects in normal and superconducting systems: localization and multifractality. *Phys. Stat. Sol. b*, 245:284, 2008.
- [171] Alexander D. Mirlin and Yan V. Fyodorov. Distribution of local densities of states, order parameter function, and critical behaviour near the Anderson transition. *Phys. Rev. Lett.*, 72:526, 1994.
- [172] Sanli Faez, Anatoliy Strybulevych, John H. Page, Ad Lagendijk, and Bart A. van Tiggelen. Observation of multifractality in Anderson localization of ultrasound. *Phys. Rev. Lett.*, 103:155703, 2009.

- [173] A. Miltenberger and F. Evers. Wave function statistics at the symplectic two-dimensional Anderson transition: Bulk properties. *Phys. Rev. B*, 75:041303, 2007.
- [174] L. J. Vasquez. *High Precision Multifractal Analysis in the 3D Anderson Model of Localisation*. PhD thesis, University of Warwick, 2010.
- [175] Alberto Rodriguez, Louella J. Vasquez, and Rudolf A. Römer. Multifractal analysis with the probability density function at the three-dimensional Anderson transition. *Phys. Rev. Lett.*, 102:106406, 2009. cond-mat:0812.1654.